Ultra-Wideband (UWB) Communication using Carrierless Amplitude Phase Modulation

Tahir Malik

A thesis submitted for the degree of

Doctor of Philosophy

in

Electrical & Electronic Engineering

at the

University of Canterbury,

Christchurch, New Zealand.

2016

ABSTRACT

Ultra-Wideband (UWB) technology can be used for high data rate, very low power communication. Pulse Position Modulated (PPM) based time domain schemes for UWB communication have been investigated in this thesis. When implemented via the time domain techniques, it is usually referred to as impulse radio UWB (IR-UWB). There is currently a need to increase the data rate of IR-UWB systems for them to be considered as a viable alternative to existing short range communication techniques.

This thesis develops a time domain based two dimensional phase incoherent Impulse Radio UWB (IR-UWB) communication scheme called pulse position modulated IR-UWB. It is based in part on the concept of carrierless amplitude phase modulation (CAP). Initially, we develop and analyse an IR-UWB system employing an M-ary time orthogonal modulation scheme, namely PPM, in an additive white Gaussian noise (AWGN) channel. Signal detection is based on maximum likelihood (ML) techniques and system performance is evaluated both analytically and by simulation and presented using bit error rate (BER) plots. We then consider M-ary PPM IR-UWB transmission in a multipath channel environment. Both matched filter and Rake receiver structures are considered. Simulation results show that the Rake offers the best performance. To help maintain high transmitted data rates, the thesis develops an M-ary PPM IR-UWB system using a two-dimensional modulation based on the concept of CAP. The resulting scheme is called M-ary PPM-CAP IR-UWB. A Rake is used at the receiver to mitigate the effects of the multipath channel. This thesis focuses on single user phase-incoherent uncoded communication based on these orthogonal modulation formats. System performance

results assume an IEEE 802.15.3a multipath channel model.

Finally, the thesis develops and evaluates an open loop synchronization technique for PPM-CAP IR-UWB. Synchronization in PPM based systems is equivalent to estimating the start time of a frame. This estimate is obtained by a feed-forward ML detector implemented within the receiver. Symbol synchronization is then obtained by means of a counter operating at the symbol rate that is initiated at the start of a frame and counts to the number of symbols in the frame. Simulation results with ML based synchronization are presented as a function of various combinations of system parameters. Results show that this synchronization scheme provides accurate data frame time estimate with less pilot symbol overhead.

Dedicated to my Parents

ACKNOWLEDGEMENTS

I would like express my deep gratitude to my supervisors, Professor Desmond P. Taylor and Associate Professor Philippa A. Martin for their guidance, motivation, technical advise and patience during my doctoral studies. Working with them has been very enlightening for both my studies and professional career.

My thanks goes to the academic, administrative, technical and computer staff in the Department of Electrical and Computer Engineering for providing the guidance, equipment and facilities required during my doctoral studies.

I would also like to thank the current and former members of the communications research group (CRG) for the technical (and not so technical) discussions we had. It has been a pleasure to work alongside you all.

My appreciation goes to my friends in Christchurch for the warm and cheerful environment that they provided me during my stay here.

Special gratitude goes to my parents for their patience and motivation during my studies. My achievements would not have been possible without their support and prayers.

CONTENTS

LIST OF FIGURES

LIST OF TABLES

Chapter 1

INTRODUCTION

1.1 INTRODUCTION TO ULTRA-WIDEBAND RADIO

Ultra-Wideband (UWB) communications has received much interest in the past decade primarily due to the simplicity involved in dealing with a carrierless transmission format. It can be used in diverse applications ranging from impulse radar to body area networks (BAN). It is a good alternative to existing short and medium range technologies such as bluetooth and other wireless protocols such as Wi-Fi. The narrow pulse format coupled with carrierless transmission makes it possible to accurately resolve the received multipath components and achieve higher data rates.

UWB (or impulse transmission) was first demonstrated as early as the late 19th century by Heinrich Hertz, using a spark gap transmitter for generation of electromagnetic waves [1], [2], [3], [4], [5]. Spark gap transmitters/radios [6] [7], are a crude form of impulse transmitter and were disallowed by 1924 as their transmission caused interference to the developing narrowband services [8]. Marconi utilized the concept of impulse radio (IR) and referred to it as transmitting *very short* or time limited electromagnetic waves for Morse code messages across the Atlantic Ocean [9], [10]. The term "very short" wave corresponded to a wave with a centre frequency of approximately 600 MHz in 1896 as experimented by Marconi [11]. Time domain based UWB is referred to as IR-UWB because of the narrow pulses involved in transmitting data, either coded or uncoded. It remains an attractive alternative to conventional RF communications because of the

lack of an explicit high frequency carrier signal. It does not require up/down conversion at the transmitter/receiver which results in less complex circuitry.

IR-UWB systems have been investigated with different modulation schemes which include pulse amplitude modulation, on/off keying (OOK), pulse position modulation (PPM) and pulse shape modulation (PSM) [12–15]. In [16], [17], IR-UWB based on bi-orthogonal PPM with time hop (TH) codes using bi-polar pulses was proposed. The schemes dependent on bi-orthogonal PPM require phase information at the receiver for demodulation, while higher order orthogonal pulse transmission (or PSM) makes the receiver more complex due to the large number of correlators [15, 17]. However, PPM remains a suitable modulation choice for IR-UWB as it does not require phase information at the receiver. It can distribute energy over the spectrum [13] and synchronization is equivalent to estimating the start time of the received frame.

Many contributions have been made to the advancement of time domain based IR-UWB. For example, [18], [19], [20], [21], describes the impact of having a Time-Hop (TH) code integrated into IR-UWB to allow multiple users to transmit within one symbol period. In [12], [22], [23] Win *et al* discussed both multiple access methods and the spectral density of UWB signals. In [24] Mireles *et al* discussed different signalling schemes for the UWB multipath channel. Molisch *et al* in [25], [26], [27] discussed channel models best suited to represent indoor multipath transmission for IR-UWB. Giannakis *et al* in [28], [29] analysed IR-UWB pulse shapes to improve the pulse spectral efficiency. Poor *et al* in [30] discussed different frame combining schemes for UWB receivers. Chiani and Giorgetti in [31] present interference issues between UWB and narrowband systems as both share the same bandwidth. In [32], [33], [34], [35] the performance of Aloha with IR-UWB are presented and discussed. Presently in the context of telecommunications, Ultra-Wideband can be described as data or information exchange via ultra-short pulses (typically nanoseconds or less in duration). IR-UWB has been proposed for applications such as location sensing, radar and imaging [36], [37], [38], [39], RFID systems [40] and Body Area Networks (BAN) [41]. Interest in IR-UWB applications over optical

fibre [42], [43] and design of UWB antennas [44] [45] [46] [47] [48] is ongoing as well.

UWB was legalized in 2002, when the American Federal Communications Commission (FCC) made a landmark decision to allow a wide band of the frequency (3.1 GHz to 10.6 GHz) to be used for unlicensed communications as long as the communication devices in this band did not interfere with existing fixed frequency, licensed and un-licensed services such as cellular networks and satellite systems [18]. To help ensure this, an emission limit of -41.3 dBm/MHz Effective Isotropic Radiated Power (EIRP) was specified by the FCC [49] for UWB. Following the FCC decision, the European regulatory authorities developed their own standards [50].

However, as is the case with every nascent mobile and/or wideband technology, reservations were expressed by the fixed services industry. For example, the Satellite Industry Association (SIA) requested a review stating that the C-band (3.7 GHz to 4.2 GHz) emission levels of UWB can interfere with Fixed Satellite Service (FSS) earth stations. The reason cited was that the 0 dBm interference to Noise level (I/N), used in deciding upon the UWB emission levels, is too high and is difficult to attain in practical satellite communication scenarios [49].

Ultra-Wideband systems are currently being looked at as a technology that can enable economic manufacturing of high data rate, short range and low power communication devices using a large unlicensed bandwidth of 7.5 GHz. One should note that the unlicensed band designated for UWB communications contains pre-existing narrowband services (such as cellular networks and satellite systems) with which UWB devices must not interfere. The IEEE 802.15 working group for Wireless Personal Area Networks (WPAN) considers UWB implementation for communications in personal area networks or short distance wireless networks [51]. For a brief overview of UWB history and applications, readers can refer to [52], [53], [54].

1.2 THESIS MOTIVATION

Most of the research in IR-UWB has been focused around using a time hop coded impulse radio signalling scheme based on PPM. While this allows multi-user transmission, it also decreases the transmitted data rates severely due to the presence of pseudo-random codes assigned to each user and inserted in the signalling format. A classical approach to allow high data rates is to transmit data through parallel streams using signals or waveforms which differ in either amplitude, frequency or phase. However, for IR-UWB signals, the transmitted signal is in the form of a pulse which is limited in time duration and has a wide spectrum. This is why it is alternatively referred to as pulse based transmission having wide bandwidth [5] [6] [55] [56] . Orthogonality is required to ensure that the pulse representing a particular data stream does not interfere with the other data streams. This is primarily achieved by modulating the transmitted pulses so that they have different pulse shapes, amplitudes or time slots as mentioned in the previous section.

A literature review (Chapter 2) shows that many modulation formats and pulse shaping technologies have been proposed for IR-UWB communications. Pulse Amplitude Modulation (PAM) and Pulse Position Modulation (PPM) are the most basic method of differentiating between pulses representing different information followed by complex Pulse Shape Modulation (PSM) and bi-orthogonal modulation based UWB transmission techniques. Whichever method is employed, the received pulses are distorted because of constructive or destructive interference induced by the multipath channel resulting in data loss. PPM and PSM follow the principles of pulse orthogonality in the time domain. PSM has been proposed as a time domain based alternative to PPM and has been applied in combination with PPM [17]. It requires matching the pulse shape rather than the pulse amplitude or pulse position. The focus of this thesis is on developing a new IR-UWB technique based on M-ary PPM orthogonal modulation with the primary objective being to increase the transmitted data rates in a multipath channel using less

complex receiver architecture.

1.3 THESIS CONTRIBUTION

The primarily contribution of this thesis is to investigate and develop a new approach towards achieving pulse orthogonality in the time domain by using an M-ary PPM IR-UWB system based on carrierless amplitude phase modulation (CAP). Previously CAP has been explored for wired communication in a simple channel model with continuous time signals having limited data rates. Its use for IR-UWB has not previously been studied, let alone that in a severe multipath channel environment. CAP is a two dimensional scheme which allows pulse orthogonality via the Hilbert transform. It allows M-ary PPM IR-UWB to transmit via an in-phase and orthogonal pulse hence thereby allowing double the throughput. Both the in-phase pulse $p(t)$ and its Hilbert orthogonal pulse $q(t)$ are used in data transmission. This thesis considers a single user uncoded transmission scenario. The new technique is referred to as M-ary PPM-CAP IR-UWB. The novel contribution of this thesis are listed below

- This thesis presents results for M-ary PPM IR-UWB in both additive white Gaussian noise (AWGN) and the IEEE 802.15.3a multipath channel model 1 (CM-1) and channel model 4 (CM-4).
- Results for M-ary PPM-CAP IR-UWB are presented for AWGN and the IEEE CM-1 and CM-4 channel models. These results are compared to M-ary PPM IR-UWB for both AWGN and multipath channels.
- Bit Error Rate (BER) results for different system parameters such as the order of modulation M, number of Rake taps and guard time required between symbols for good performance in the multipath channels are presented.
- M-ary PPM-CAP IR-UWB does not require phase information for demodulation at the receiver. It gives double the data rates of M-ary PPM IR-UWB. With a

modest amount of guard time the system is robust to the interference caused by the multipath channel.

- Simulation results show a Rake with 30 taps provides a good trade-off between complexity and performance for M-ary PPM-CAP IR-UWB.
- A feed-forward synchronization scheme is described for M-ary PPM-CAP IR-UWB. BER results show little performance degradation when using this scheme compared to a perfectly synchronized M-ary PPM-CAP IR-UWB system.

1.4 THESIS OVERVIEW

The rest of this thesis is organized as follows:

Chapter 2

This chapter presents an overview of wireless communication in the context of UWB. This is followed by a review of the different types of UWB communication schemes in use today. Next, an overview of possible pulse types is presented along with the pulse shape used in this thesis. This is followed by M-ary orthogonal modulation concepts and signal detection techniques used. The multipath channel is then discussed as UWB communication channels are modelled as multipath channels with large excess delay times in comparison to the pulse width. This is followed by an overview of the Rake receiver and its application to signal detection in the multipath channel. Finally, we present some current applications of UWB.

Chapter 3

In this chapter the M-ary PPM IR-UWB is described and its analytical and simulated results are presented. Then an M-ary PPM-CAP IR-UWB is described along with the transmitter and receiver structure. Next, we propose and simulate the M-ary PPM-CAP scheme. Finally, BER results in AWGN are presented and discussed.

Chapter 4

The focus of this chapter is to present the system model and BER results for M-ary PPM IR-UWB and M-ary PPM-CAP in an IEEE 802.15.3a CM-1 and CM-4 multipath channel. ML detection is used to obtain estimates of the received signal using a Rake receiver. First, the mathematical model for M-ary PPM IR-UWB is presented in the multipath channel. ML detection is used for obtaining the estimated received data. Next, we introduce M-ary PPM-CAP for the multipath channel and present signal detection using ML estimation. This is followed by simulated performance results and discussions for the proposed M-ary PPM-CAP scheme. The BER results presented are obtained assuming ideal channel estimation and synchronization at the receiver.

Chapter 5

This chapter investigates and presents system performance when using estimated synchronization in M-ary PPM-CAP IR-UWB. Synchronization is achieved by adding pilot symbols to the PPM-CAP data frame. First, a system model for PPM-CAP IR-UWB with synchronization pilot symbols is developed. System evaluation is done by simulations primarily for the multipath CM-1 channel. Results are presented for both perfect and imperfect synchronization at the receiver. System performance is shown by both BER and normalised mean square error (NMSE) plots.

Chapter 6

In this chapter, conclusions and potential areas of further research into M-ary PPM-CAP IR-UWB are presented. The results presented in chapters 2 through 4 are summarised and briefly reviewed for M-ary PPM-CAP IR-UWB. The performance gains between M-ary PPM and PPM-CAP IR-UWB are emphasized. Potential research areas for M-ary PPM-CAP IR-UWB are also discussed.

1.5 LIST OF PUBLICATIONS/RESEARCH OUTCOMES

This section lists the publications were submitted as a result of the work of this thesis. The primary research outcomes of this thesis are the design and evaluation of a PPM-CAP IR-UWB scheme and the development of a synchronization approach for PPM-CAP IR-UWB. The following papers based on the thesis have been submitted for publication:

1. Tahir Malik, Desmond P. Taylor and Philippa A Martin, "Impulse Radio using Carrierless Amplitude Phase Modulation", Submitted to the IEEE Transactions on Vehicular Technology, Under Review, November 2015.

   This paper first presents an overview of M-ary PPM IR-UWB in a multipath channel. It then develops and discusses the M-ary PPM-CAP scheme with similar multipath channel conditions. Lastly, It presents results and corresponding data rates achieved by using PPM-CAP. The results show that BER performance from using PPM-CAP degrades by approximately 2 dB from that of a PPM IR-UWB scheme. However, the advantage of using PPM-CAP is double data rates.

2. Tahir Malik, Desmond P. Taylor and Philippa A Martin, "Synchronization in Carrierless Amplitude Phase Modulated IR-UWB", Submitted to the IEEE Transactions on Vehicular Technology, Under Review, December 2015.

   This paper presents results for a PPM-CAP IR-UWB scheme with ideal and non-ideal synchronization. Simulation results show that for high values of signal to noise ratio, the BER achieved for both cases are identical.

Chapter 2

WIRELESS COMMUNICATION USING UWB

2.1 ULTRA-WIDEBAND COMMUNICATION

Ultra wideband was referred to as impulse, carrierless or non-sinusoidal transmission until 1989 when the US Department of Defence used the term Ultra-Wideband (UWB) [8], [28], [57]. Win and Scholtz in [12], [58], [59], [24] have described the ultra-wideband time domain pulse based communication as Impulse Radio UWB (IR-UWB). The simplest form of IR-UWB digital transmission consists of an impulse signal (extremely narrow time pulse) being used to represent a data bit. The receiver makes a decision by comparing the received pulse energy [54] against a threshold.

UWB systems can be time domain or frequency domain based. Time domain UWB systems transmit the input data via a series of UWB impulses employing some form of modulation such as pulse position modulation (PPM), pulse amplitude modulation (PAM), pulse shape modulation (PSM) or a combination of them [17]. The time duration of the transmit pulse is typically on the order of nanoseconds and occupies a very wide frequency band [12]. Time hop (TH) codes with IR-UWB have been used in [12], [18] to improve multiple access in a multiuser environment. UWB (non-impulse radio type) in the frequency domain is usually implemented via orthogonal frequency domain multiplexing (OFDM) [60].

Due to the nature of the wide bandwidth associated with pulse transmission, UWB radios operate at very low power levels, average Effective Isotropic Radiated Power

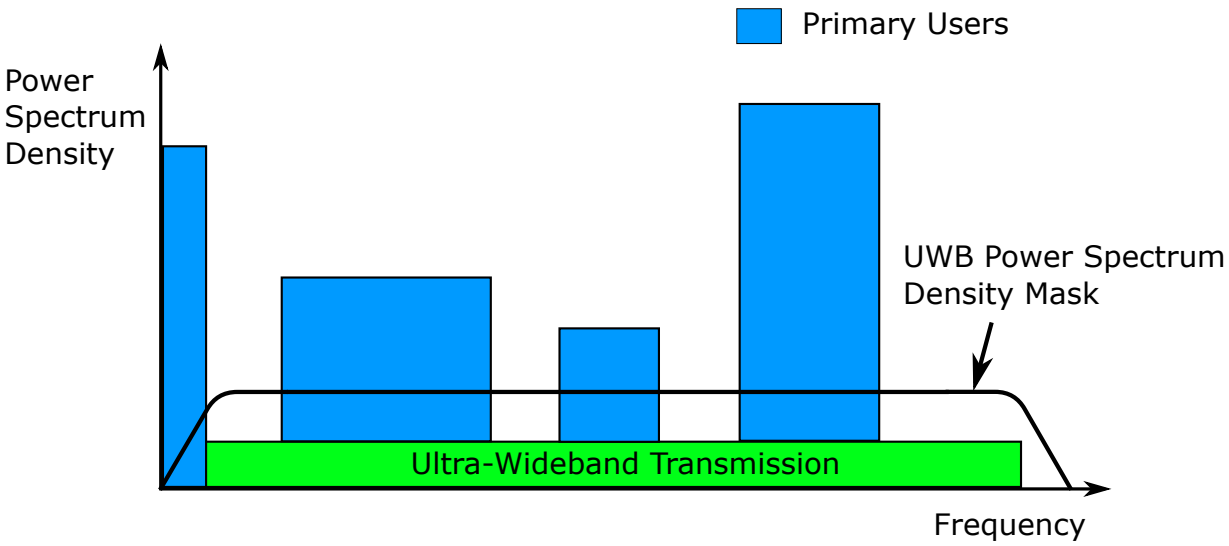

Figure 2.1: UWB radio spectrum comparison.

(EIRP) of about -41dBm per 1 MHz in the 3.1 GHz to 10.6 GHz band [50] and "47 C.F.R 15.519(f) - Technical Requirements for Hand Held UWB Systems" of the FCC [1]) so as not to cause interference to existing users. UWB communications is defined by both its *absolute bandwidth* and *relative or fractional bandwidth*. *Absolute bandwidth* refers to the actual bandwidth occupied by the signal. *Relative or Fractional bandwidth* is expressed as the percentage bandwidth occupied by the signal relative to its center frequency. UWB systems should have a bandwidth greater than 500 MHz and are referred to as having large absolute bandwidth [5] [61]. Large absolute bandwidth can be advantageous in providing high resilience to fading, interference resistance and greater accuracy of ranging and geolocation. This makes UWB attractive for certain applications such as being used in an underlay approach to spectrum sharing [62] [63] in environments where existing users and fixed band services already exist. Figure 2.1 gives an example of UWB bandwidth overlap over the other services without causing interference. An incoherent and low power architecture favors low data rate (LDR) to medium data rate (MDR) personal area networks (PAN) [28]. Possible applications can be remote

[1] http://www.gpo.gov/fdsys/granule/CFR-2010-title47-vol1/CFR-2010-title47-vol1-sec15-519/content-detail.html

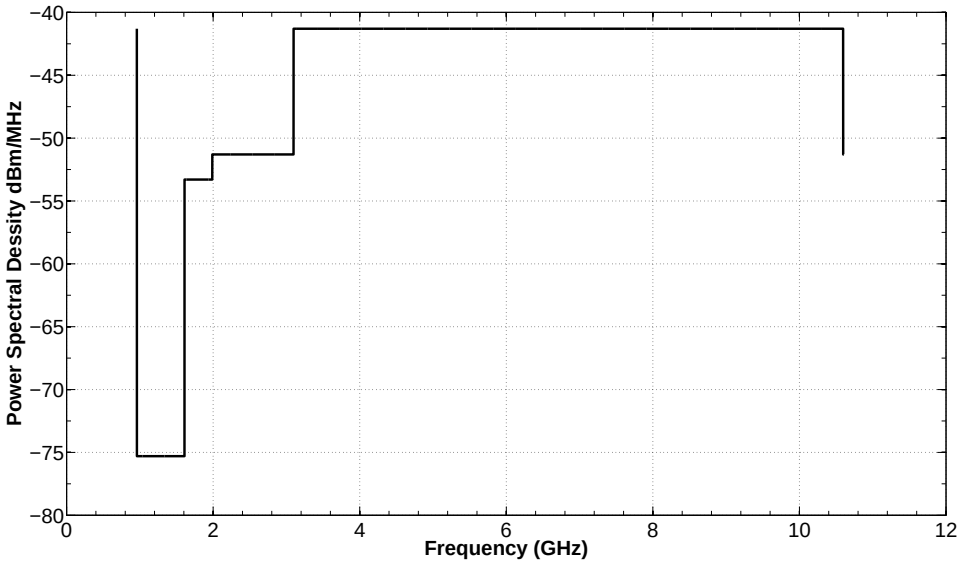

Figure 2.2: FCC UWB spectrum mask.

health monitoring, office automation and wireless sensor networks. Low average power consumption by UWB radios can be achieved by transmitting signals at low duty cycle and suitably limiting the peak power.

Figure 2.2 [50] shows a more specific power spectral density mask for UWB communication as allowed by the FCC. Other countries follow more or less the same spectral mask for UWB communication. Figure 2.3 sows the European UWB spectrum mask.

2.2 OVERVIEW OF ULTRAWIDE BAND (UWB) SYSTEMS

Ultra wideband communication can be categorized into five main types [6], [55]

1. Time Hopping Impulse Radio UWB (TH IR-UWB).

2. Direct Sequence Spread Spectrum Impulse Radio UWB (DS IR-UWB).

3. Multi-Band UWB (MB-UWB), for example OFDM based UWB.

4. Frequency Hopping-UWB (FH-UWB).

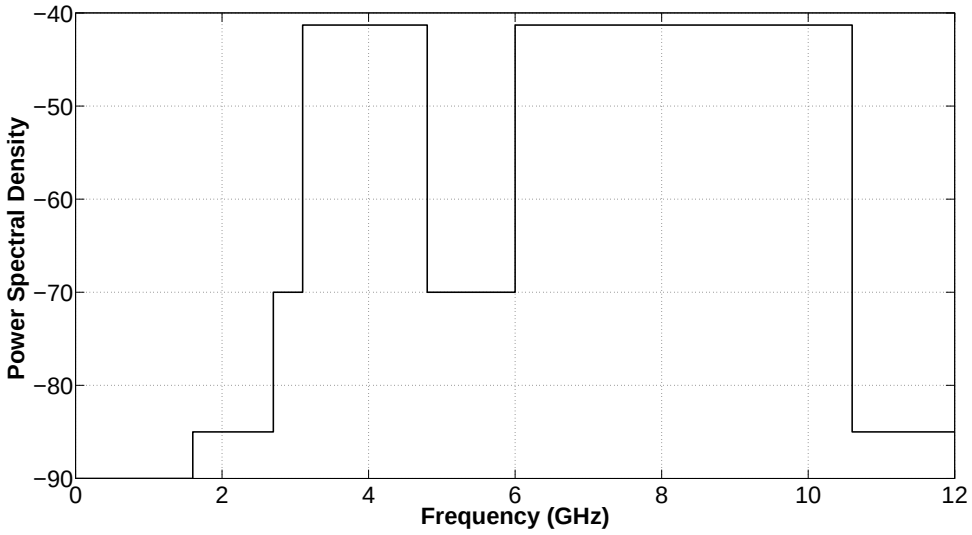

Figure 2.3: European UWB spectrum mask.

5. M-ary Pulse Position Modulated Impulse Radio UWB (PPM IR-UWB).

Figure 2.4 summarizes the current techniques used for implementing UWB i.e. time and frequency domain based methods. Time based UWB is known as IR-UWB while frequency based UWB is referred to as frequency modulated (FM) UWB and multi-band (MB) UWB. We will now describe the various implementation schemes for UWB in Section 2.2.1 to Section 2.2.5.

2.2.1 Time Hop Pulse Position Modulation Impulse Radio UWB (TH IR-UWB)

Time hop (TH) pulse position modulated impulse radio UWB (or TH IR-UWB) is a scheme in which each user is assigned a specific time hop code [6] [12] [55] [64] via which the user's data is represented in terms of time positions assigned to a series of pulses. It is multi-user centric and does not focus on high data rate transmission. A repetition code can be used with TH IR-UWB systems to reduce catastrophic collisions [6], [64] and [65]. Figure 2.5 shows a TH IR-UWB transmitter block diagram.

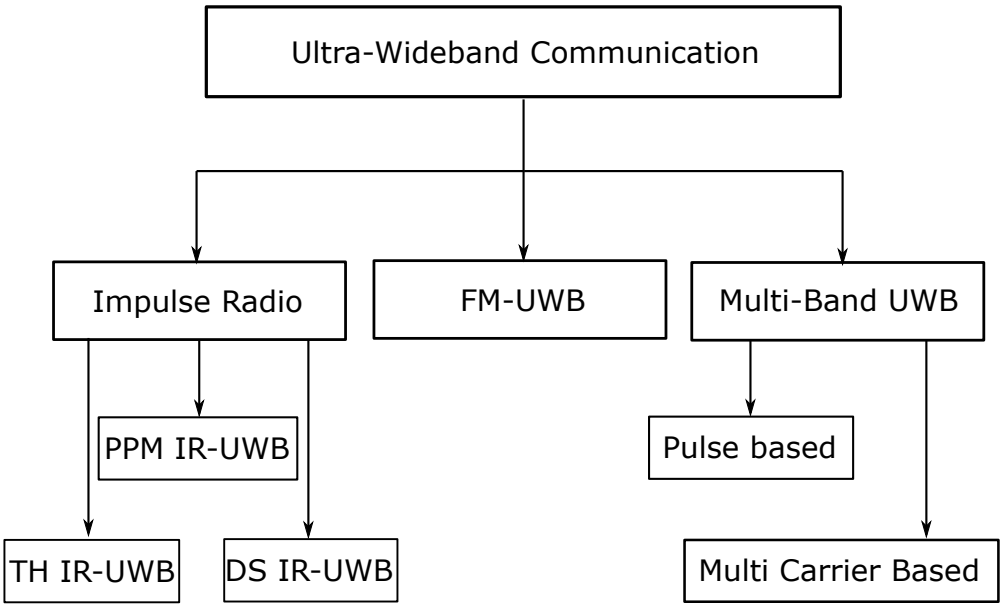

Figure 2.4: UWB implementation techniques.

TH IR-UWB was first implemented and studied by Scholtz [19], [20], [21] and Win [12], [23]. It focuses more on TH codes and less on pulse position modulation (PPM). It has been discussed in the context of bit by bit transmission [12], [18] and appears to be limited to binary transmission. The signalling elements of the Scholtz-Win TH IR-UWB transmission scheme are *chip*, *symbol* and *frame*.

Figure 2.6 shows a detailed format of the transmitted symbol in a TH IR-UWB scheme. The figure shows two frames each consisting of four chip slots. The input data bit is a '1' and the TH sequence is such that it assigns the pulse to the first chip in both frames. PPM is obtained by inducing a slight offset in the pulse within a chip duration as shown in the figure. For example, for an input binary data bit '1' the pulse lies in the second

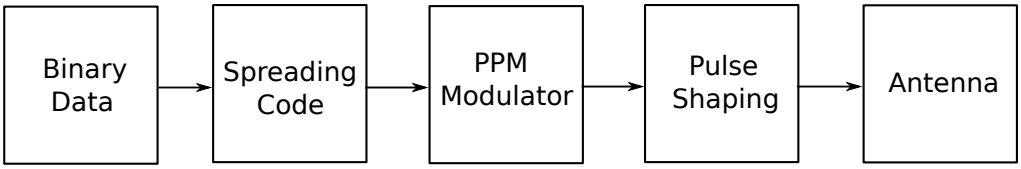

Figure 2.5: TH IR-UWB system block diagram.

half of the chip slot and for an input data bit '0' the pulse lies in the first half of the chip.

The proposed transmission scheme is shown in Figure 2.7. It consists of *chips*, *frames* and *symbols*. The minimum addressable time delay bin is a *chip* having a time duration T_c. Each user's information is contained in the form of a single pulse, which is positioned within the chip time slot that is assigned to the user by the time hop code. N_c chip time slots are grouped to form a *frame* having duration $T_f = N_c \times T_c$. A pseudorandom (PN) TH code is then inserted into this transmission scheme. This TH code allocates one chip position (out of N_c available chips within a frame) to the respective user's pulse.

PPM is incorporated within the transmit symbol format by inserting a time offset ϵ to the pulse position, while limiting the pulse to the allotted chip time boundary. An offset of ψ will denote a data bit '1' and no offset will denote a data bit '0'. This scheme considers separate transmitters for each user. The TH PN code is used to decrease data collisions between users and makes use of a correlation receiver to decode each user's data stream based on the PN code assigned to that user. A group of N_f frames is called a *symbol*, which has time duration $T_s = T_f \times N_f$. The receiver differentiates between users based on their assigned TH code sequence.

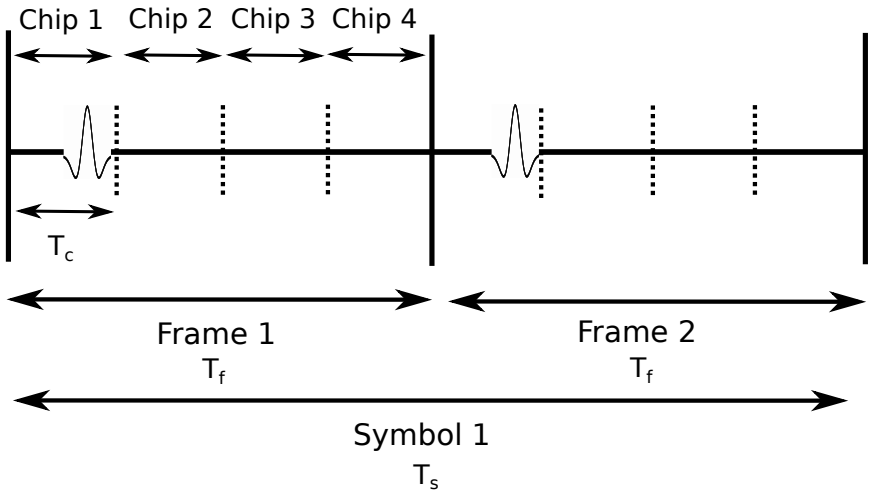

Figure 2.6: TH IR-UWB - transmitted symbol format.

Mathematically, this scheme can be formulated by first representing the binary data sequence $\mathbf{a} = (a_0, a_1, a_2, ..., a_{N-1})$ where N represents the number of bits in the binary sequence. After passing through a repetition coder which repeats each bit N_f times, the binary sequence can be represented as $\hat{\mathbf{a}} = (\hat{a}_0^0, \hat{a}_0^1, ..., \hat{a}_0^{N_f-1}, \hat{a}_1^0, \hat{a}_1^1, ..., \hat{a}_1^{N_f-1}, ..., \hat{a}_{N-1}^0, \hat{a}_{N-1}^1, ..., \hat{a}_{N-1}^{N_f-1})$. The repeated data bits can be represented as $\mathbf{b}$, where $b_i = \hat{a}_i \, \forall \, i$. This results in $\mathbf{b} = (b_0, b_1, b_2, b_3, ..., b_i, b_{i+1}, ...)$. This sequence has rate $R_b = 1/T_b$ bits/s and

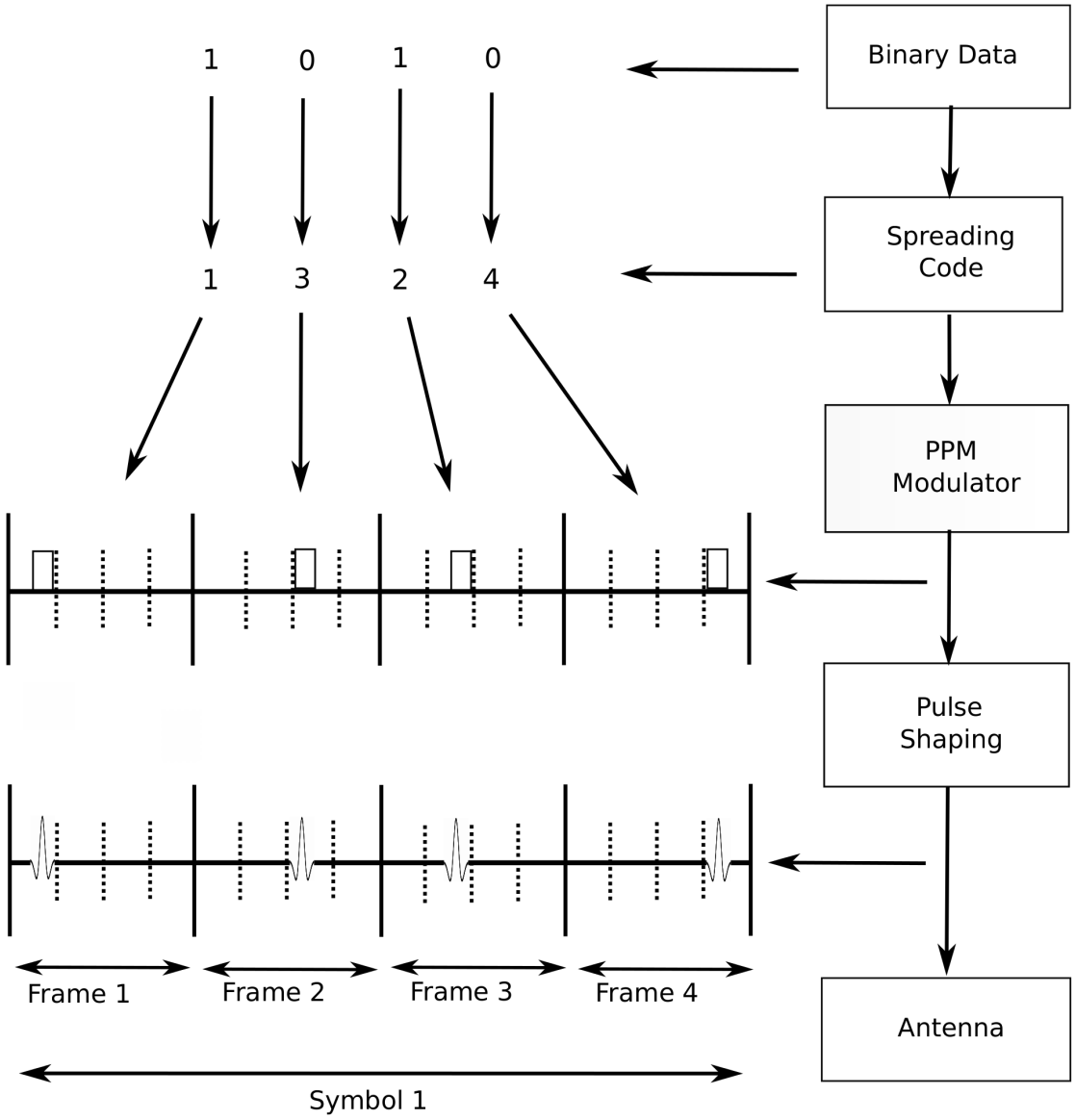

Figure 2.7: TH IR-UWB - transmitter diagram.

each element b_i represents one data bit.

A second block (transmission coder) codes the sequence $\mathbf{b}$ by a pseudo-random TH code $\mathbf{c} = (c_0, c_1, c_2, c_3, c_i, c_{i+1}, ...)$. In a multi-user environment each user can be assigned a different pseudorandom TH code. The sequence at the output of the transmission coder is then pulse position modulated. Generally, the periodicity of the code, N_p, is taken equal to the length of the repetition code, N_f. The PPM block introduces a time delay defined by

$$d_i = c_i T_c + b_i \psi, \tag{2.1}$$

where T_c (chip time) and ψ (time shift introduced by the PPM modulator) are constants chosen by the system designer. $c_i T_c + \psi < T_f$ for all c_i. $b_i \psi$ denotes a time offset within a chip interval, induced by the PPM modulator to differentiate a data bit '1' ($b_i \psi = \psi$) from a data bit '0' ($b_i \psi = 0$). The PPM delay $b_i \psi$ is modelled as half the chip time for convenience, i.e. the pulse lies in the first half of the chip if the input data bit is '0' and in the second half of the chip if the input data bit is a '1'. After PPM, the resulting sequence or symbol (which practically consists of N_c chips) is fed to the pulse shaper which transmits a pulse at the correct chip time. The transmitted signal has the form [6], [66],

$$s(t) = \sqrt{E_s} \sum_{i=0}^{+\infty} p(t - iT_f - c_i T_c + b_i \psi), \tag{2.2}$$

where i denotes the number of input data bits corresponding to a single user in TH-UWB. T_f denotes the time duration of one frame. The term iT_f denotes that the pulse is positioned within the i^{th} frame. T_c is the chip duration and $c_i T_c$ denotes the chip slot assigned by the i^{th} element of the TH code in the current frame. $p(t)$ is the pulse shape produced by the pulse shaper block.

TH-UWB can be used with [55],

- Pulse Shape Modulation (PSM) - pulses are orthogonal between users. This scheme can be used when there are multiple users transmitting. For example,

we can use wavelets or prolate spheroidal waveform functions (PSWF) to develop wideband orthogonal pulses [55] [17].

- Pulse Interval Modulation (PIM) - In which two pulses are transmitted and the time interval between them is used to represent the data [55].

These signalling formats can all be used with non-coherent reception of the signal, but they require accurate synchronization. Note that modulation generally refers to mapping of a baseband signal onto a high frequency carrier signal for transmission to the receiver. In this case, it is assumed that there is no high frequency carrier. Thus the term impulse radio (IR) is used.

Impulse Radio as described above is inefficient as it only considers bit by bit transmission. In addition, since the chip times only last a couple of nanoseconds at most, it can be extremely difficult for the receiver to decode multiple pulse positions, within a chip, based on a slight offset of ψ. Hence, development of a new framework for UWB transmission (of the Impulse Radio category) is needed as we cannot expect high data rates from the current scheme due to its limitation of employing bit by bit or binary transmission. One method of increasing throughput is to transmit groups of k-bits simultaneously and use a higher order scheme.

We neglect the repetition coder as multi-user transmission is not the focus of this thesis. Our main objective is to develop a scheme which allows an increase in throughput using an M-ary signalling format. The basic building blocks of this scheme are explained in the next section.

2.2.2 Direct Sequence Impulse Radio UWB

Direct sequence IR-UWB (or DS IR-UWB) spreads the spectrum using spreading codes and is classified as a form of impulse radio [6] [55]. This technique was developed alongside TH IR-UWB. A repetition coder is usually used to introduce redundancy. The bandwidth of the transmitted signal is determined by the chip rate of the spreading

sequence. In contrast to the PN TH code used in TH IR-UWB, DS IR-UWB utilizes a polarity based pseudorandom code along with TH requiring coherent reception. At the receiver the original data symbols can be recovered by correlation of the received signals with the same spreading code that is used at the transmitter [52]. In contrast to classical direct sequence spread spectrum techniques, which make use of a carrier modulated by a message signal, DS IR-UWB is carrierless. Multiple users can transmit at the same time as long as each user is assigned a unique PN TH code with polarity information. Figure 2.8 shows the DS IR-UWB transmitter block diagram [6].

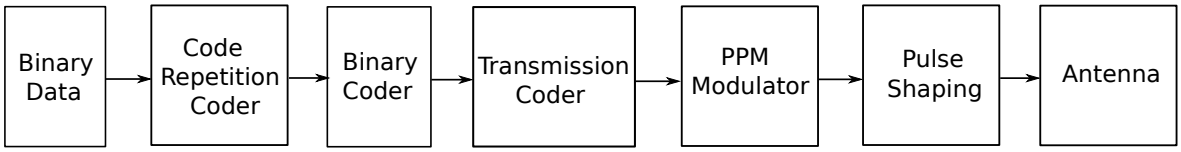

Figure 2.8: Direct sequence IR-UWB block diagram.

We consider a binary data sequence $\mathbf{b} = (b_0, b_1, ..., b_k, b_{k+1}, ...)$ with rate $R_b = 1/T_b$ bits/s. This sequence is fed to a (N_f,1) repetition coder, meaning each bit of the data sequence $\mathbf{b}$ is repeated N_f times. The output data sequence of the repetition encoder is denoted by

$$\tilde{\mathbf{a}} = (b_0^0, b_0^1, ..., b_0^{N_f-1}, b_1^0, b_1^1, ..., b_1^{N_f-1}, b_k^0, b_k^1, ..., b_k^{N_f-1}, b_{k+1}^0, b_{k+1}^1, ..., b_{k+1}^{N_f-1}, ...) \quad (2.3)$$

where $\tilde{\mathbf{a}}$ has a repetition rate of $\tilde{R}_{cb} = N_f/T_b = 1/T_f$ bits/s. $\tilde{\mathbf{a}}$ is then converted into positive and negative data sequences denoted by $\mathbf{a}$, where $\mathbf{a} = (a_0, a_1, a_2, ..., a_j, a_{j+1}, ...)$ with rate $R_{cb} = N_f/T_b = 1/T_f$ bits/s.

The next block is the transmission coder. The input to this block is the sequence $\mathbf{a}$ and it's output is the sequence $\mathbf{d}$. The transmission coder multiplication sequence $\mathbf{c}$ is a pseudorandom code of +1's and -1's having a period of $N_p = N_f$. This code helps differentiate one sequence from another at the receiver. Mathematically $d_j = a_j c_j$, where j refers to the individual sequence elements. Here, $\mathbf{d}$ is generated at a rate

$R_c = N_f/T_b = 1/T_f$ bits/s.

The sequence **d** is given as input to the pulse amplitude modulator for pulse polarity modulation corresponding to the unit pulses (positive or negative) at time jT_f and a rate of $R_p = N_f/T_b = 1/T_f$ pulses/second, as in Figure 2.8.

The last stage of the DS IR-UWB system is the pulse shaping filter. This takes as input unit pulses and transmits a desired pulse shape in place of the unit impulses. The transmitted pulse *p(t)* can be designed according to the available regional spectral mask so that UWB transmission does not interfere with narrowband systems. The sequence of transmitted pulses can be represented as [6]

$$s(t) = \sum_{j=-\infty}^{+\infty} d_j p(t - jT_s). \tag{2.4}$$

2.2.3 Multi-Band UWB

Multi-Band UWB is different from classical IR-UWB techniques. In MB-UWB transmission is done within multiple spectrum bands or sub-bands of the spectrum [56] [67]. This can allow greater spectral efficiency depending on pulse shape and scheme used, but increases complexity. To comply with FCC UWB regulations each sub-band must have a bandwidth greater than 500 MHz [55].

This approach to UWB transmission can provide better interoperability between UWB devices in different regions of the world- as different frequency ranges for UWB communication bands are defined in different geographical areas [50], and thus the devices can adjust their band of operation according to the radio environment. The sub-band approach can also increase user capacity by allowing the users to hop among different sub-bands according to a pseudo-random code [28]. Each sub-band can have a different bandwidth, centered around different frequencies depending on

1. the region in which the radio operates,

2. any existing active fixed band services,

3. Interference being caused to or from the existing UWB sub-band.

The pulse shaper in multi-band transmission shapes each pulse so that the spectrum of the pulse stays within its assigned sub-band and does not interfere with adjacent sub-bands or narrow band services. From the FCC mask, shown in Figure **??**, we observe that not every sub-band will be allowed to have the same transmit power level limit and the transmitter will have to limit both the width of the pulse and its power level. Rather than developing transceivers which have fixed circuits in them built for specific multi-band communication in particular regions, we can develop reconfigurable hardware in which the pulse shaper does the re-configuration portion by conditioning the pulse time and bandwidth. Two approaches to multi-band UWB are,

1. *Pulse sequence* based- Pulse sequence multi-band UWB consists of a sequence of pulses with different center frequencies (but the same bandwidth) being transmitted in series with a small guard time inserted between transmissions [56]. This scheme is carrierless. The spectrum of each pulse occupies a percentage (or sub-band) of the total available UWB spectrum (which can be up to 7.5 GHz wide in USA). The individual sub-bands are non-overlapping, hence the name multi-band UWB. Pulse shaping can be done by prolate spheroidal wave functions (PSWF), Hermite polynomials or other suitable methods so that they are limited in time.

   Data can be modulated in this scheme in a number of ways, the simplest being on-off keying. With multiple access, each frequency band can be allotted to a specific user. Figure 2.9 shows the transmitted signal of such a scheme and the sub-bands of the individual pulses. In this figure pulses are assigned a number. For example, Figure 2.9 assigns pulses '1' up to 'N'. The bands occupied by the respective pulses are appropriately labelled as shown in Figure 2.9 [55].

2. *Multicarrier* based- Two techniques are used to accomplish this.

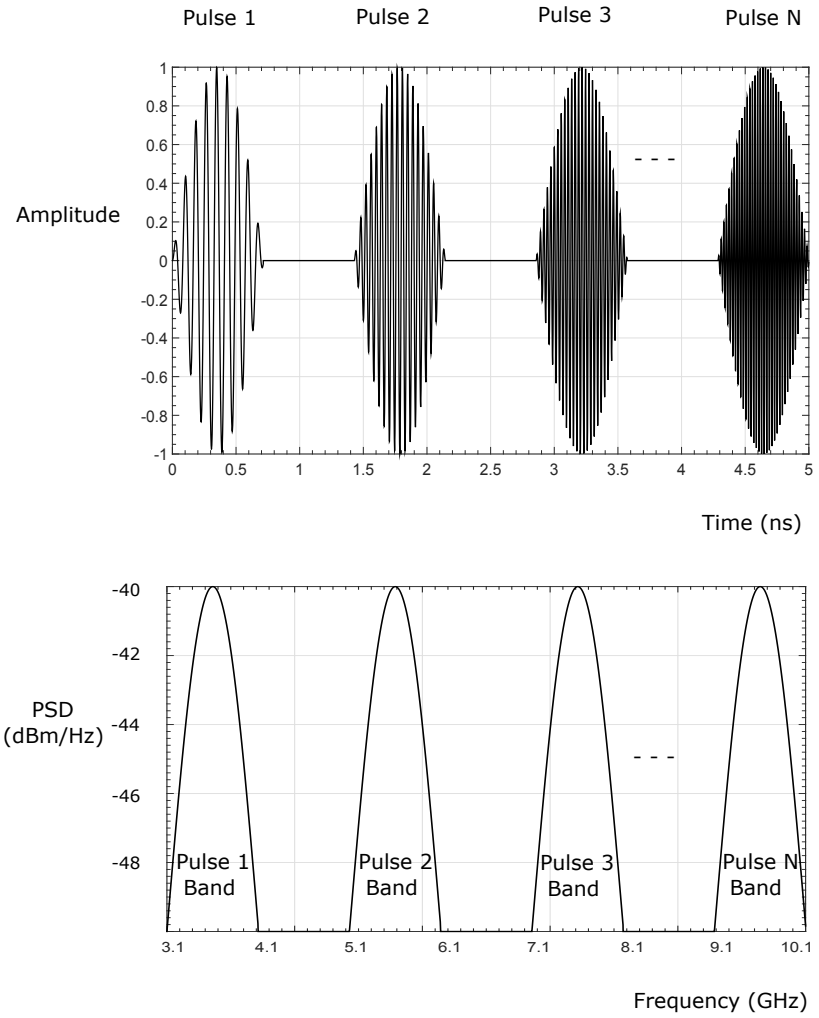

Figure 2.9: Pulse based multi-band UWB. Top figure shows the individual pulses being transmitted consecutively. Bottom figure shows their corresponding bands in the frequency domain.

(a) Multiple non-overlapping carriers- Multiple carriers are generated separately and data is modulated onto them as shown in Figure 2.10 [55] [56]. This technique reduces inter symbol interference (ISI) because each band can be exactly designed but increases hardware complexity. This technique is alternatively referred to as analog Orthogonal Frequency Division Multiplexing [5].

(b) Orthogonal Frequency Division Multiplexing (OFDM)- This technique can

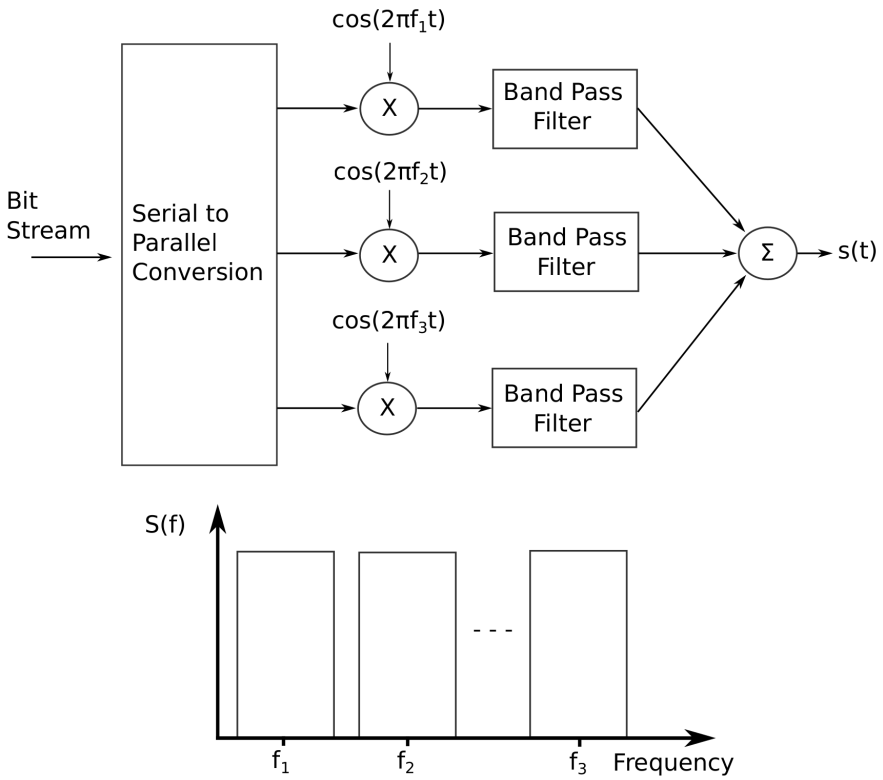

Figure 2.10: Carrier based Multiband-UWB.

be extended to OFDM with multiple access and be used to implement multicarrier UWB by transmitting information in parallel on a large number of subcarriers. The data stream is first converted from serial to parallel. Modulation is then performed digitally first by an inverse fast Fourier transform (IFFT) on the data. A fast Fourier transform (FFT) is performed at the receiver to recover the data [5], [55]. This eliminates the need for complex hardware components such as filters and mixers at the receiver end [60]. It can provide data rates as high as 480 Mb/s and can be used with a variety of modulations such as BPSK, QPSK, PAM, QAM, FSK etc. [68] [69].

2.2.4 Frequency Modulated UWB

FM-UWB was also proposed for UWB radio communication at low data rates. It is a frequency domain approach for UWB systems design [70]. FM-UWB (or UWB-FM) is a constant envelope frequency domain system [71]. It is a double FM scheme in which a low modulation index ($\beta_{digital}$) FSK is used first. This is followed by a high modulation index (β_{analog}) analog FM to achieve a wide bandwidth. However, it has not been worked upon during the last few years and so is not considered further.

2.2.5 M-ary Pulse Position Modulated IR-UWB

In contrast to the TH IR-UWB scheme, which is limited to binary transmission primarily due to large symbol times and lower throughput, an orthogonal M-ary PPM IR-UWB scheme aims to increase data throughput by transmitting blocks of data i.e. symbols constituted by grouping together k input bits. The channel can be shared between users using time division multiplexing or a token ring system rather than incorporating TH codes [72]. The PPM IR-UWB transmit signal structure is very similar to that of a TH IR-UWB scheme in that there are three basic blocks to it i.e. *pulse slot*, *symbols* and *frames*.

The *pulse slot* time is the smallest time interval in PPM IR-UWB transmission. Its duration is denoted by T_c and the number of pulse slots within a symbol are denoted by N_c. The UWB symbol represents k bits of data. Figure 2.11 shows a 8 PPM IR-UWB signal sequence which comprises of two distinct symbols. In classical binary TH IR-UWB schemes, the pulse time is optimally designed to be half of the chip time and an offset of $\psi = \frac{1}{2}T_c$ is introduced to differentiate between a bit '0' or '1' [6]. However, in M-ary PPM IR-UWB the pulse randomly occupies any of the M pulse slots depending on the combinations of the input k bits. Hence, an M-ary PPM IR-UWB system has $M = 2^k$ symbols in its signal space. The offset, ψ here can be represented by T_c or the pulse slot time. Next up in the hierarchy is the *symbol*. Symbol time is denoted by T_s

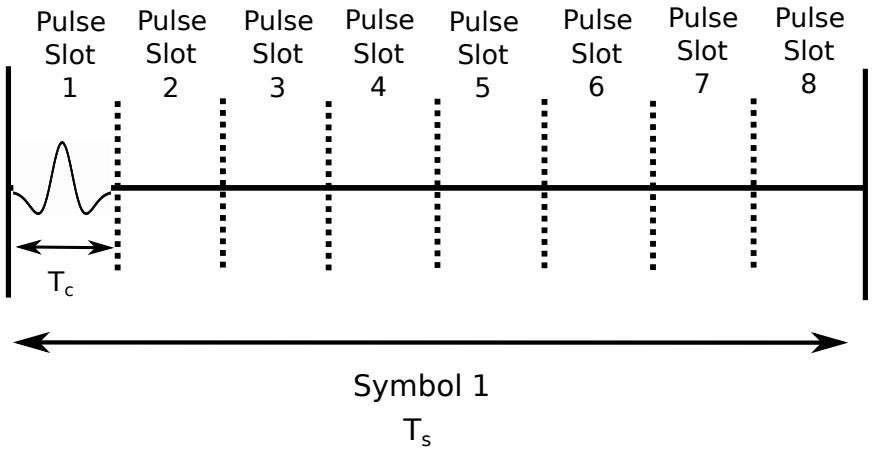

Figure 2.11: Uncoded 8-PPM IR-UWB transmitted symbol.

which is essentially $M \times T_c$. A *frame* is the longest member of this hierarchy. A frame consists of many symbols grouped together and has a time duration T_f. The number of transmitted symbols a_n, where $a_n \in 0, 1, 2, ..., M-1$, and $M = 2^k$, are assumed to have equal energy E_s, are independently distributed and represented vectorially as

$$\begin{aligned} a_0 &= (\sqrt{E_s}, 0, 0, \ldots, 0) \\ a_1 &= (0, \sqrt{E_s}, 0, \ldots, 0) \\ &\vdots \\ a_{M-1} &= (0, 0, 0, \ldots, \sqrt{E_s}). \end{aligned} \tag{2.5}$$

A PPM IR-UWB signal can be mathematically represented as

$$s_n(t) = \sqrt{E_s} p(t - nT_s - a_n T_c), \tag{2.6}$$

where $nT_s \leq t \leq (n+1)T_s$, E_s denotes the symbol energy, M is the number of possible symbols and T_s is the symbol time. The term nT_s denotes the n^{th} symbol time. T_c represents pulse slot time. The term $a_n T_c$ gives the pulse slot number in which the pulse is to be positioned, based on the number of bits grouped together to form a symbol. Figure 2.12 depicts the signal sequence for two symbols in a 8 PPM IR-UWB

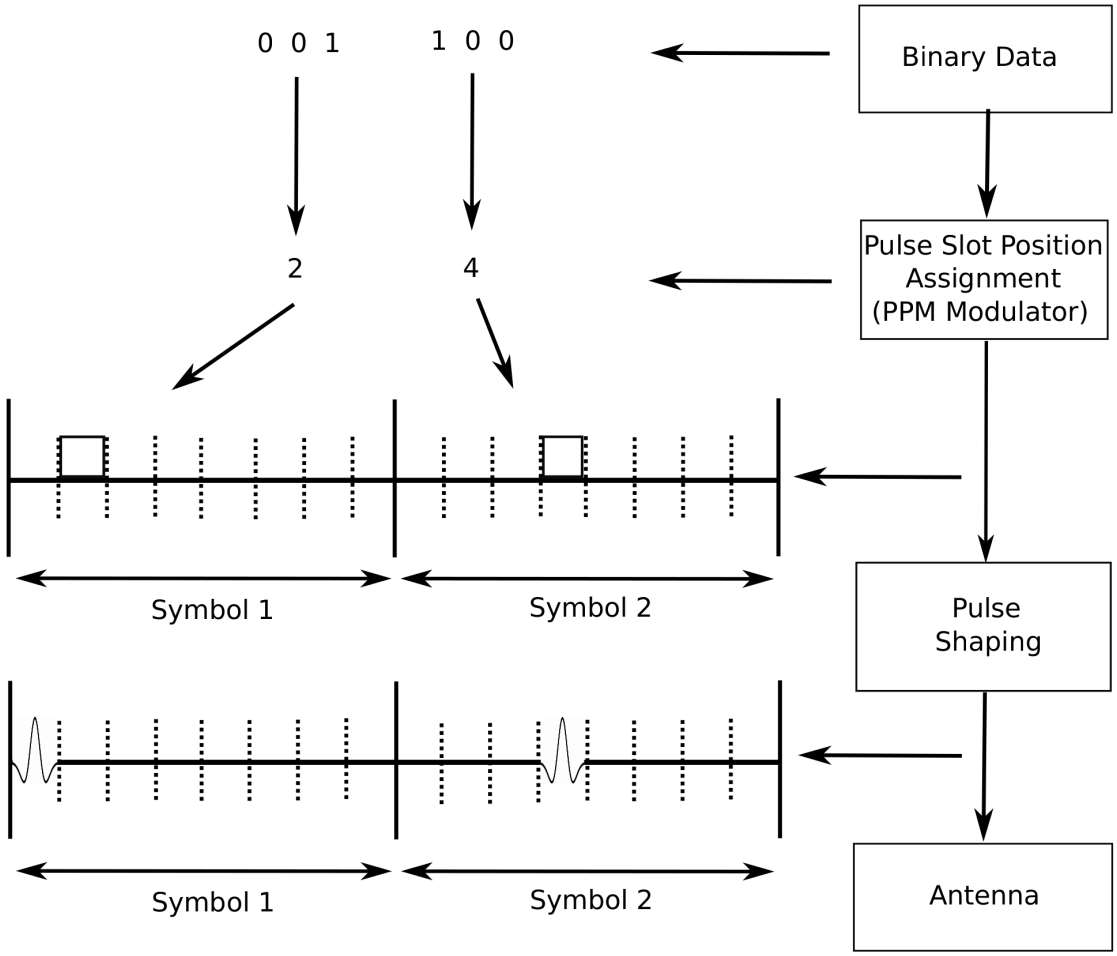

Figure 2.12: 8-ary pulse position modulated ultra-wideband (8 PPM IR-UWB) scheme.

scheme.

2.3 PULSE SHAPING IN ULTRA-WIDEBAND COMMUNICATIONS

Pulse shaping is used to keep the transmitted pulse within the mandated regulatory spectrum masks [24] [73] [74] [75]. It is an important aspect to consider in any UWB transceiver [76] [77]. As seen from Figure 2.2, the FCC mask is not a flat horizontal line but varies with frequency and specifies the allowable PSD level at different frequencies. IR-UWB is inherently carrierless and any form of modulation which requires a high frequency carrier is not consistent with classical IR-UWB [55]. Many proposed IR-UWB

schemes typically involve using pulse shapes such as the Gaussian, Gaussian doublets, sinusoidal polycycles, Rayleigh waves and raised cosine pulses. A major limitation is realizing physical circuits for their generation [78].

Assuming $P(f)$ to be the Fourier transform of $p(t)$, we can model its energy spectrum as

$$\Phi_{uu}(f) \approx \alpha \left|P(f)\right|^2, \tag{2.7}$$

where α is a constant.

It is preferred that $|P(f)|^2 = S_{FCC}(f)$, where $S_{FCC}(f)$ is the spectrum of the FCC mask [29]. Another useful term here is the normalized effective signal power (NESP), which is the ratio of power transmitted ($S_p(f) = |P(f)|^2$) in a chosen band (B_p) within the spectral mask to the total power permissible under the given mask. This can be mathematically written as $\overline{\psi} = \frac{\int_{B_p} S_p(f)df}{\int_{B_p} S_{FCC}(f)df}$. As $S_{FCC}(f)$ is either fixed or cannot be altered, we are left to maximize the value of $S_p(f)$ i.e.

$$\psi = \int_{B_p} S_p(f)df. \tag{2.8}$$

Equation (2.8) is used to determine how closely a pulse can approach the available spectrum mask. Pulse shaping can be implemented in a low cost package as proposed in [79]. Some of the main pulse shaping techniques are,

1. Gaussian Pulse.
2. Scholtz Monocycle.
3. Rayleigh monocycle.
4. Hermite Polynomial pulse design.
5. Prolate Spheroidal Wave Functions.
6. Wavelets.

Readers can refer to [7] [74] [77] [79] [75] [80] [81] [82] [82] [83] and [84] for insight into the pulse shapes and design methodologies. For the purpose of this thesis, a brief overview of the Gaussian pulses and the Scholtz monocycle are given as these are used in the literature extensively. This thesis uses the Scholtz monocycle pulse with a duration of 1 ns unless otherwise specified.

2.3.1 Gaussian Pulse

The simplest way to have carrierless transmission is to employ a Gaussian pulse function as the transmitted waveform [73] [6] [55]. However, a Gaussian pulse on its own is spectrally inefficient and does not approximate well the spectral mask allotted for UWB communication [85] [74]. The basic Gaussian pulse is given by

$$p(t) = \left\{ \pm(\frac{A}{\sqrt{2\pi}\sigma})(\exp(-\frac{t^2}{2\sigma^2})) \right\} rect\left(\frac{t}{T_p}\right), \tag{2.9}$$

where σ^2 is its variance, A is its amplitude and T_p is the pulse width in seconds. The Gaussian pulse (shown in Figure 2.13) is along with its odd order derivatives [73] are often used so as to increase the transmitted pulse center frequency and to minimize the average DC content for transmission, as the odd order derivatives tend to have no DC content. A linear combination of different derivatives of the basic Gaussian pulse can be used to produce a single pulse shape that achieves good spectral utilization and multi-user interference performance has been proposed [86]. The first derivative and second derivative pulse shapes of the Gaussian pulse are shown in Figure 2.14 and Figure 2.15. Theoretically the duration of any form of Gaussian pulse is infinite, however for analysis we can define a pulse width (T_p) which contains 99.99% of the pulse energy. This relates to $T_p = \alpha\sigma$, where α is set to achieve 99.99% pulse energy containment [87] [88]. Techniques using high frequency carrier signals [89], [90] have been proposed that combine a Gaussian pulse with a high frequency carrier for better managing the pulse bandwidth. However, such a technique does not conform to classical

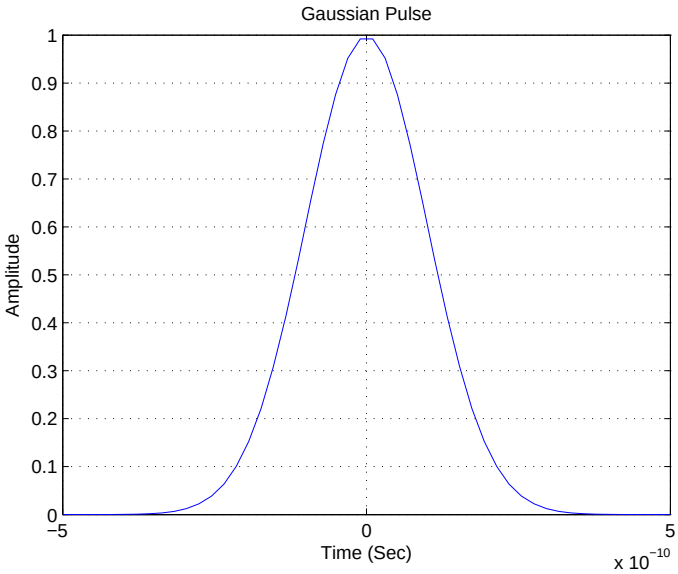

Figure 2.13: Gaussian pulse.

IR-UWB due to the presence of a sinusoidal carrier in the modulation. Pulse duration varies in the literature from 0.16 nanosecond to 1 nanosecond [91].

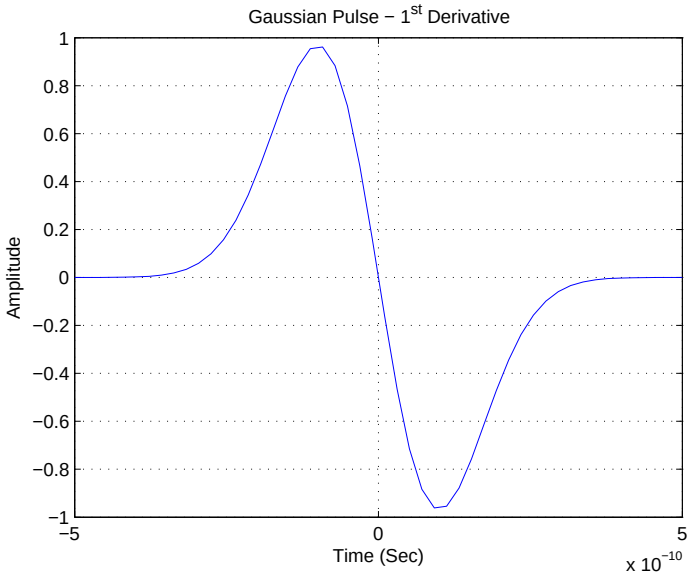

Figure 2.14: Gaussian pulse - 1^{st} derivative.

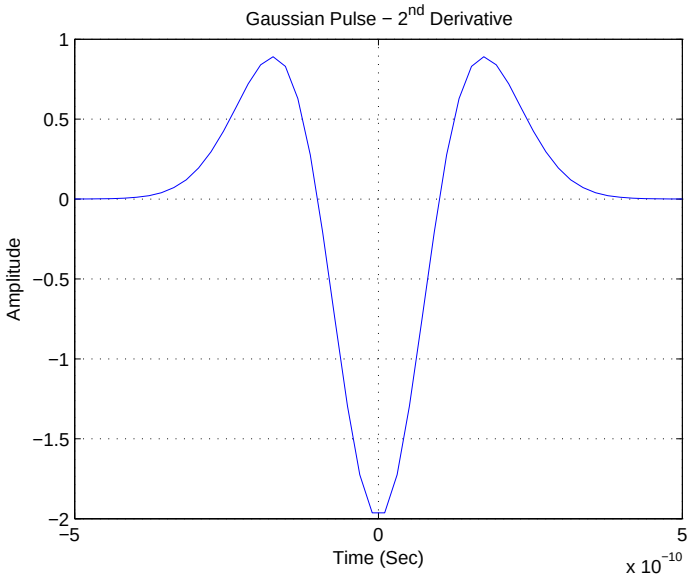

Figure 2.15: Gaussian pulse - 2^{nd} derivative.

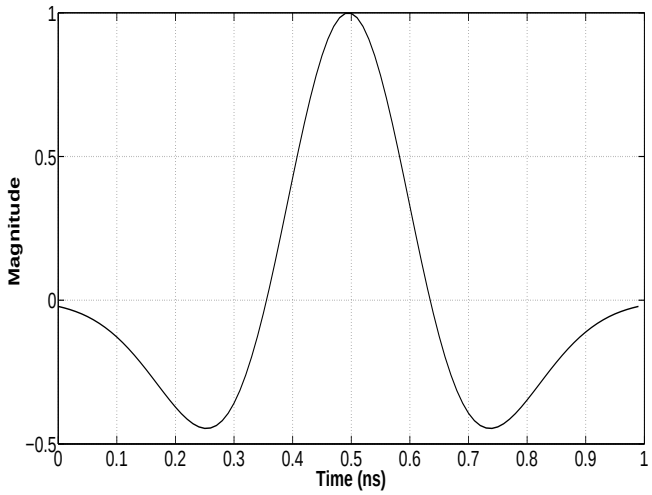

Figure 2.16: Scholtz monocycle pulse template.

2.3.2 Scholtz Monocycle

The Scholtz monocycle [28] was used during UWB work by both Win and Scholtz. Much of their pioneering work was done using this monocycle pulse [12] and is described as being a representation of a received pulse at the receiving antenna. Figure 2.16 shows a Scholtz monocycle based IR-UWB pulse template. This thesis uses the Scholtz monocycle so as to keep the pulse choice standardized [12] [20] [28] [58]. It can be mathematically represented by

$$p(t) = \left\{ \left[1 - 4\pi \left(\frac{t}{T_p} \right)^2 \right] \exp\left(-2\pi \left(\frac{t}{T_p} \right)^2 \right) \right\} rect\left(\frac{t}{T_p} \right), \tag{2.10}$$

where $0 \leq t \leq T_p$, T_p is the pulse width in seconds. For simplicity, in an M-ary PPM IR-UWB scheme the pulse width is taken as equal to the chip duration so that $T_p = T_c$.

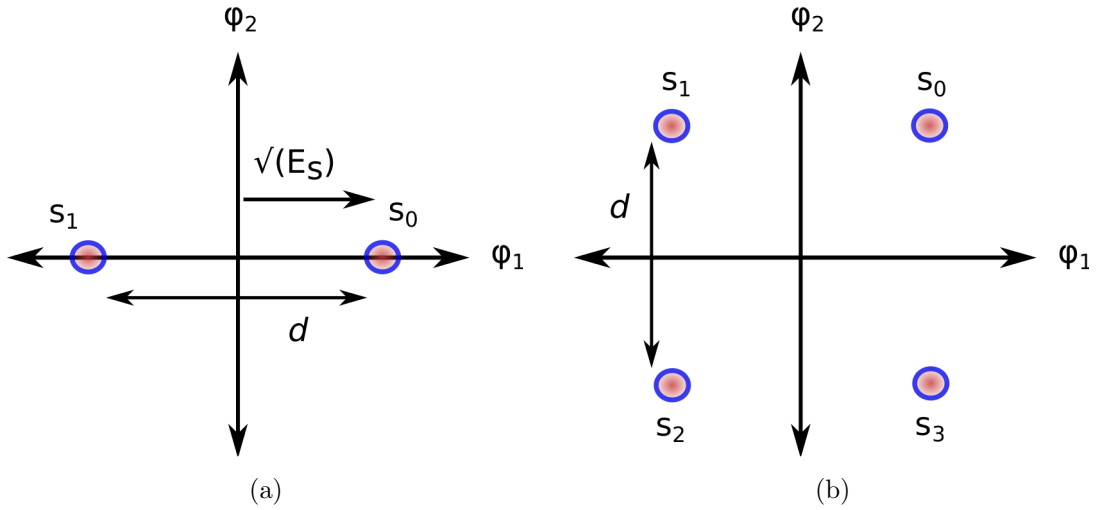

(a) (b)

Figure 2.17: Bit by Bit signalling scheme (a) binary signal space and (b) quaternary signal space.

2.4 UWB COMMUNICATIONS BIT BY BIT SIGNAL ANALYSIS VS. BLOCK ORTHOGONAL SIGNAL ANALYSIS

Block orthogonal signalling and bit by bit signalling have both been used for communications [92]. Bit by bit signalling [12] [28] [53] can be expressed using multi-dimensional models ranging from a simple 1D constellation having two points each of which represents a single bit, to a Hypercube model that can be used to represent any M symbols over a N dimensional vector space in which $N \leq M$. Figure 2.17(a), Figure 2.17(b) and Figure 2.18 depict some constellations with a varying number of symbols and dimensions. Here $M = 2^k$, where k represents the number of bits per symbol. However, while these models are widely used, they are complex to implement due to the requirement for phase information in their demodulation. In bit by bit signalling $E_s = E_b$, as each point in the signal space represents one bit. To achieve symmetry in the signal space for bit by bit signalling, bipolar modulation is often used.

The analytical probability of bit error $P(\epsilon)$ for such a binary constellation is given by

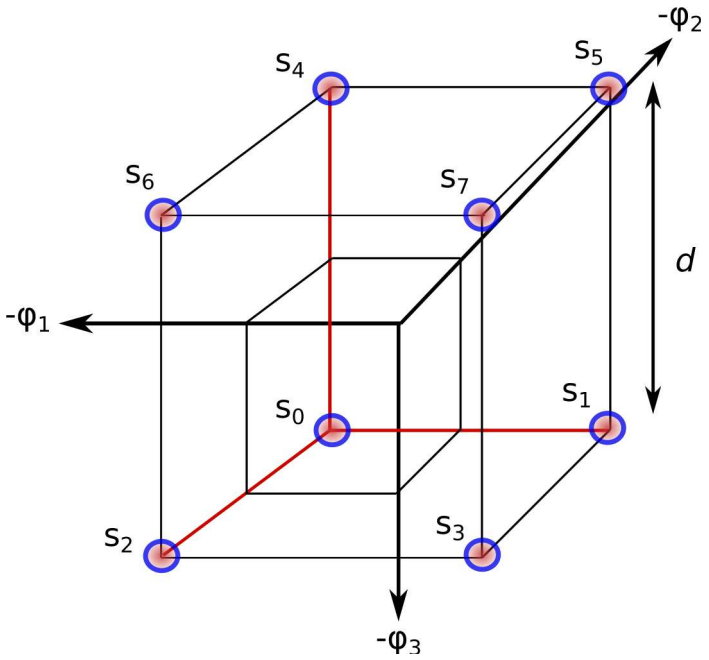

Figure 2.18: Hypercube signal constellation.

(2.11) [92],

$$P(\epsilon) = Q\left(\sqrt{\frac{2E_b}{N_0}}\right), \tag{2.11}$$

where E_b is the energy per bit, $N_0/2$ is the PSD and $k = 1$ is the number of bits per symbol for the binary case.

PPM is a special case of orthogonal modulation and is significantly different from bi-polar schemes [93] because the information is embedded entirely in the position of the pulse within a symbol whereas in bi-polar modulation the polarity of the pulse partly carries the information. For the special case of M orthogonal signals (each having equal energy E_s), we represent each signal on a single dimension. Thus $M = N$ for M-ary orthogonal signals. This representation leads to block signalling analysis in which can be represented by low complexity uncoded schemes. Two such schemes are an M-ary PPM system in the time domain, or a M-ary frequency based system in which each symbol is represented in the frequency domain by using sinusoidal carriers having M different frequencies. Figure 2.19(a) shows the simplest case where we have two signals

($M = 2$) being represented in two dimensions (i.e. $N = 2$) ϕ_1 and ϕ_2, respectively. The signals s_0 and s_1 are orthogonal to each other. Figure 2.19(b) shows the equivalent time domain binary PPM transmission scheme with two possible time slots. Each time slot represents one symbol. An orthogonal signal constellation is different from a biorthogonal constellation. For comparison, Figure 2.20 shows a biorthogonal constellation set for $N = 2$ and $M = 2N$ symbols. This constellation is obtained from an orthogonal set of N signals by taking the negative of each signal. For the simple case of a sinusoid, the negative is denoted by a phase shift of 180 degrees. The negative amplitude (or phase inversion) effectively cuts in half the number of dimensions required in a biorthogonal signalling space as compared to that required in orthogonal signalling space [92] [93], the trade off being that we need to employ coherent demodulation.

Orthogonal signalling is used in this thesis. For a binary orthogonal scheme, assuming an AWGN channel, the probability of symbol error that s_0 is transmitted and received incorrectly i.e. $p[\epsilon|s_0]$ is equal to $p[\epsilon|s_1]$ as we assume equiprobable symbols. $p[\epsilon|s_0]$ can be written as [92]

$$p[\epsilon|s_0] = \int_{d/2}^{\infty} \frac{1}{\sqrt{\pi N_o}} e^{-\alpha^2/N_o}\, d\alpha, \tag{2.12}$$

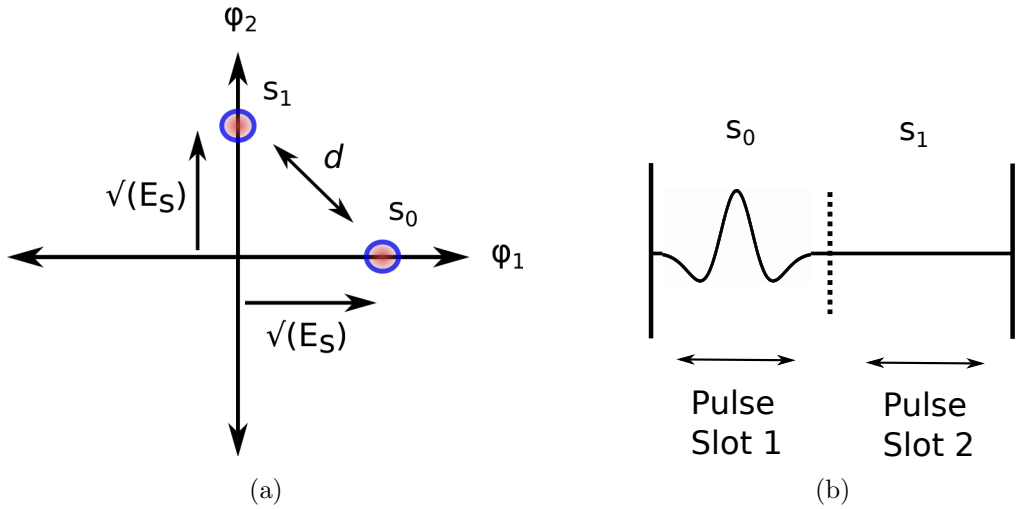

(a) (b)

Figure 2.19: (a) binary orthogonal signal space constellation and (b) binary PPM signal.

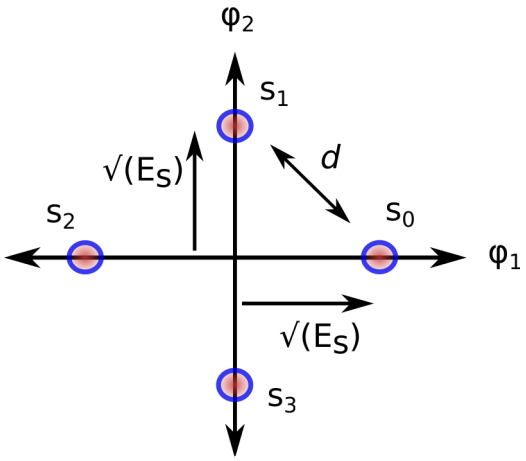

Figure 2.20: Biorthogonal signal constellation.

where d represents the distance between the two signal space points s_0 and s_1. α represents the received symbol. For binary orthogonal schemes $d = \sqrt{2E_s} = \sqrt{2kE_b}$, where E_b represents the energy per bit and k is the number of bits per symbol. For binary orthogonal schemes, $k = 1$. As both symbols are assumed to be equiprobable, a union bound on this is given by $p[\epsilon] = Q(\sqrt{E_s/N_o})$. This bound can be expanded to the M-ary case and is expressed as $p[\epsilon] \leq (M-1)Q\left(\sqrt{\frac{E_s}{N_0}}\right) < e^{-E_s/2N_0}$, where M denotes the number of orthogonal symbols. This upper bound applies to an M-ary PPM IR-UWB system [16] as an example of an orthogonal signalling scheme.

In contrast to bit by bit signalling, the probability of error for a scheme employing block orthogonal signalling can be made to go to zero by increasing either increasing E_b or k because E_s is directly proportional to both. Thus, by keeping E_b constant, k results in better $p[\epsilon]$. Whereas, in bit by bit signalling one has to increase E_b to decrease $p[\epsilon]$ [92].

2.5 M-ARY ORTHOGONAL SIGNAL DETECTION IN AWGN

Most detection techniques are derived for an AWGN environment and are optimal with respect to minimizing the probability of error of the received signal or maximizing the output signal to noise ratio at the receiver. Implementation of these techniques for mul-

tipath channels results in degraded detection performance, but may provide acceptable system performance with low complexity especially when the complexity of optimal detection cannot be afforded. Signal detection can be implemented using either time or frequency domain based techniques [92] [94] [93].

2.5.1 Maximum A Posteriori (MAP) Signal Detection

An optimum receiver aims to minimize the probability of error (or maximize the probability of detection) based on the received signal $r(t)$. Since we consider here a memoryless channel, we can make the decision per signal (or symbol) interval [92], [94], [93]. A decision rule that aims to maximize the probability of detection and based on the received symbol is called the *maximum a posteriori* probability (MAP) criterion. It is an optimal detection technique used for detection in AWGN. It takes into account the *a posteriori* probabilities, i.e. the probability that the transmitted a_i is conditioned on the received signal $r(t)$, which can be denoted vectorially as $\mathbf{r}$. The *a posteriori* probability is the probability that a_i was transmitted given r was received and can be expressed as $P(a_i \,|\, \mathbf{r})$, where $i = (1, 2, \ldots, M) \,\forall\, M$. MAP detection chooses the signal a_i, out of all possible M symbols, that has the highest posterior probability. Using Bayes rule, the *a posteriori* probability can be expressed in terms of the *a priori* probability of the transmitted a_i as

$$P(a_i|\mathbf{r}) = \frac{f(\mathbf{r}|a_i)P(a_i)}{f(\mathbf{r})}, \tag{2.13}$$

where $f(\mathbf{r}|a_i)$ is the conditional probability density function of the observed symbol given a_i is transmitted (i.e. the *likelihood function*) and $f(\mathbf{r})$ is the total probability of the received symbol i.e. $f(\mathbf{r}) = \sum_{m=1}^{M} f(\mathbf{r}|a_m)P(a_m)$. Note that for optimum detection MAP requires the *a priori* probabilities to be available at the receiver.

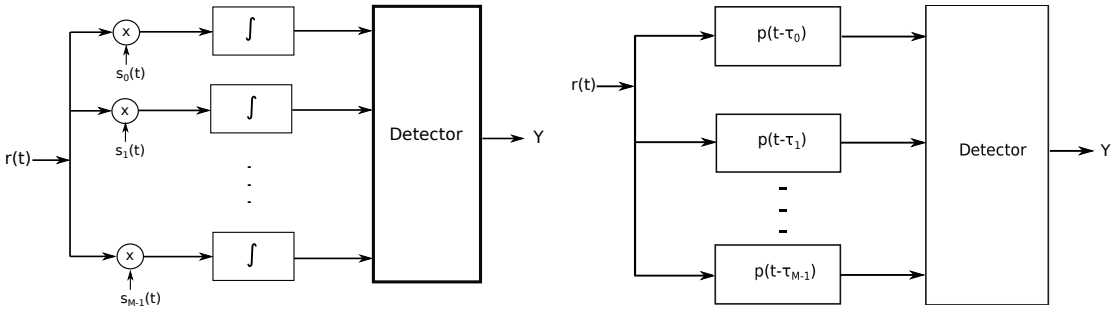

Figure 2.21: AWGN optimum signal detectors. (a) correlation receiver and (b) matched filter receiver.

2.5.2 Maximum Likelihood (ML) Signal Detection

We will assume equiprobable *a priori* probabilities of the M symbols, i.e. $P(a_m) = 1/M$. In addition, the term $f(\mathbf{r})$ can be ignored due to not having any dependency the on transmitted symbol. Hence, we are left with a simplified MAP criterion in which the probability of correct decision depends solely on choosing the symbol which maximizes $f(\mathbf{r}|a_i)$. This is referred to as *maximum likelihood* (ML) detection and provided that the *a priori* probabilities of the M transmitted symbols are equal, receivers based on either of the two detection criterias (MAP or ML) will produce the same result [95]. From [93], maximizing the probability of detection is equivalent to choosing that $\mathbf{a_i}$ which maximizes the correlation (or correlation metric) between the received signal and the M possible signals. The correlation metric may be expressed as

$$C(\mathbf{r}, \mathbf{a_i}) = 2\mathbf{r}.\mathbf{a_i} \quad \forall\, i = (1, 2, \ldots, M). \tag{2.14}$$

Receivers based on ML detection are optimum for detecting a signal (or pulse) in AWGN and can be realized by correlation based techniques as shown in Figure 2.21(a) or by a matched filter as in Figure 2.21(b) [92], [94], [93]. The symbol a_i that maximizes the output SNR, out of the M possible symbols, is taken to be the received symbol.

In PPM, the correlation receiver uses symbol length templates $s_i(t)$ where $i = 0, 1, ..., M-$

1. In contrast, the match filter receiver uses a filter matched to the pulse shape which is delayed successively in terms of τ_i for $i = 0, 1, ..., M-1$. This translates to $\tau_i = iT_c \,\forall\, i$. In both cases, the detector selects the value of that input branch, out of M input branches, having the maximum value.

2.6 SIGNAL DETECTION IN MULTIPATH CHANNELS

A multipath channel model [66] [96] [97] [98] [99] [100] [101] mathematically models the path gains and time delays induced in the transmitted signal by the environment. For transmission, the multipath model of the received signal consists of multiple pulses or echos, each having a different amplitude and time delay, where the amplitude and time delay of each received pulse or echo depends on the path. The channel gain coefficients are represented by $\mathbf{H} = (h_0, h_1, ..., h_{L_{channel}-1})$ and the time delay associated with the coefficients by $\boldsymbol{\tau} = (\tau_0, \tau_1, ..., \tau_{L_{channel}-1})$, respectively. The total number of multipath components in the channel impulse response is denoted by $L_{channel}$. Figure 2.22 illustrates a four tap multipath channel representation. $s(t)$ denotes the transmitted signal which consists of a single pulse $p(t)$. $h(t)$ denotes the multipath channel impulse response and τ_i denotes the time delay of the i^{th} multipath component. The total channel delay or time duration of the channel impulse response is denoted by $T_{channel}$. The received signal may be represented as

$$r(t) = \sum_{i=0}^{L_{channel}} h_i \, s(t - \tau_i), \tag{2.15}$$

where, $r(t)$ is the combined signal, $L_{channel}$ represents the number of multipath components or paths taken by the transmitted signal, h_i is the weight or gain of each path, τ_i is the time delay corresponding to h_i. However, the multipath channel illustrated in Figure 2.22 is rarely measured in a real world environment. The impulse response of the multipath channel is likely to have multipath components that are not equally spaced and will have random delays at the receiver. This necessitates channel impulse

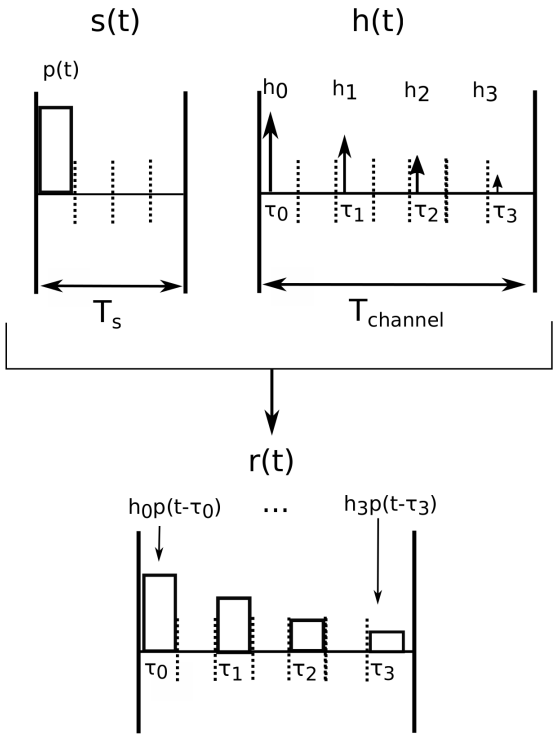

Figure 2.22: Multipath channel representation.

response measurements in the operating environment and designing the Rake receiver tap weights and delays according to obtained measurement readings. This could mean unequally spaced delays in the Rake receiver. Signal detection in multipath is significantly more difficult than for an AWGN channel. Multipath channels with long delay spread result in inter-symbol interference (ISI). ML detection in a multipath channel can yield good results provided some form of receiver architecture that employs equalisation techniques is used to collect and combine the energies of the received multipath distorted signal. One type of receiver that can accomplish this is the Rake receiver [102], [103] which has different taps or fingers each tuned to a specific path so as to capture and combine all the multipath components.

2.7 CORRELATION RECEIVER FOR MULTIPATH SIGNAL DETECTION

Ideally, the received multipath component signals are assumed to be completely orthogonal. This allows us to employ a receiver structure known as the multipath correlation receiver or *Rake* receiver [66] [93] [104] [105]. It is optimal in the sense that it maximizes output SNR in multipath channels. It comprises of L_p taps or fingers each matched to a delayed version of the transmit pulse$p(t)$. Figure 2.23 shows a typical Rake structure consisting of L_p taps or fingers. The correlators in Figure 2.23 can be realized by a correlation receiver as in Figure 2.21(a) or matched filter receiver as in Figure 2.21(b). Each tap is matched to the channel gain coefficients $\mathbf{H} = (h_0, h_1, ..., h_{L_P-1})$ and delay $\boldsymbol{\tau} = (\tau_0, \tau_1, ..., \tau_{L_p-1})$. The correlation or match filter template is generally taken as the transmitted pulse template. The number of branches depends on how much complexity in the Rake is afforded by the system designer.

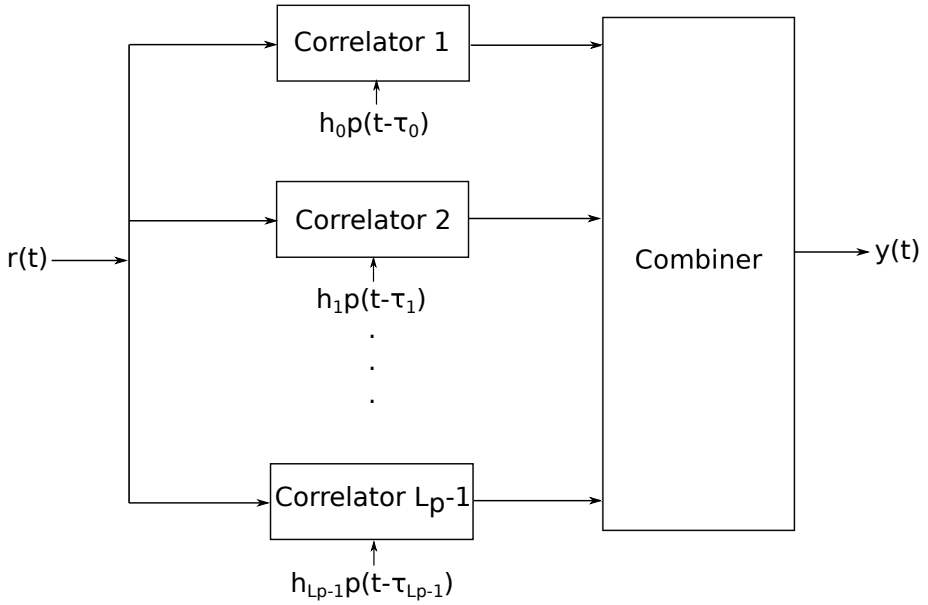

Figure 2.23: Rake receiver.

A Rake is referred to as diversity combining receiver because it adds up a number of (attenuated and delayed) copies of the transmit signal. The Rake has been successfully used for code-division multiple-access [106] and TH IR-UWB based schemes in [107],

[108], [109], [110], [111]. It can be divided into two categories which are based on the tap selection method for multipath energy combining. These Rake structures are *all*-Rake and the *selective*-Rake which are detailed in the next section.

2.7.1 All-Rake

The term *all*-Rake (A-Rake) or an ideal Rake [6] [66] is used to denote a Rake in which the number of Rake taps L_p are equal to the number of multipath components $L_{channel}$ in the channel. Referring to Figure 2.23, the number of taps L_p is equal to the number of channel multipath components $L_{channel}$. The A-Rake is optimal in the sense that it captures all the multipath energy and combines it for improved signal to noise ratios at it's output.

A special case of the A-Rake is when the first N multipath components of the received signal are collected at the receiver. This structure has less correlators compared to the A-Rake and is referred to as a *partial* Rake [6] [66] or simply a Rake having L_p taps where $L_p = N < L_{channel}$. It is suited to channels which have strong multipath components in the earlier portion of the channel impulse response.

2.7.2 Selective-Rake

A *selective*-Rake (S-Rake) [6] [66] refers to a Rake structure that collects the N strongest multipath components of the received signal for diversity combining. These N strongest components are then combined for increasing the signal to noise ratio of the received signal.

This is a fairly complex scheme in which accurate channel estimation and detection methods must be employed to determine those multipath components that have the highest energy. Depending on the multipath channel, the benefit of implementing such a Rake is that the number of correlators required can be significantly reduced compared to the ideal Rake. Those multipath components which have the highest energy are

selected for combining in a S-Rake. Multipath channels having an impulse response in which the strongest multipath components are not concentrated in the beginning but rather are distributed throughout the channel impulse response would benefit from such a Rake.

2.8 RAKE COMBINING TECHNIQUES

Another significant parameter selection in the Rake is the weight w assigned to the multipath components after they are combined. Figure 2.24 shows the Rake structure with weights assigned to each tap. These techniques aim to optimize the output SNR of the Rake receiver.

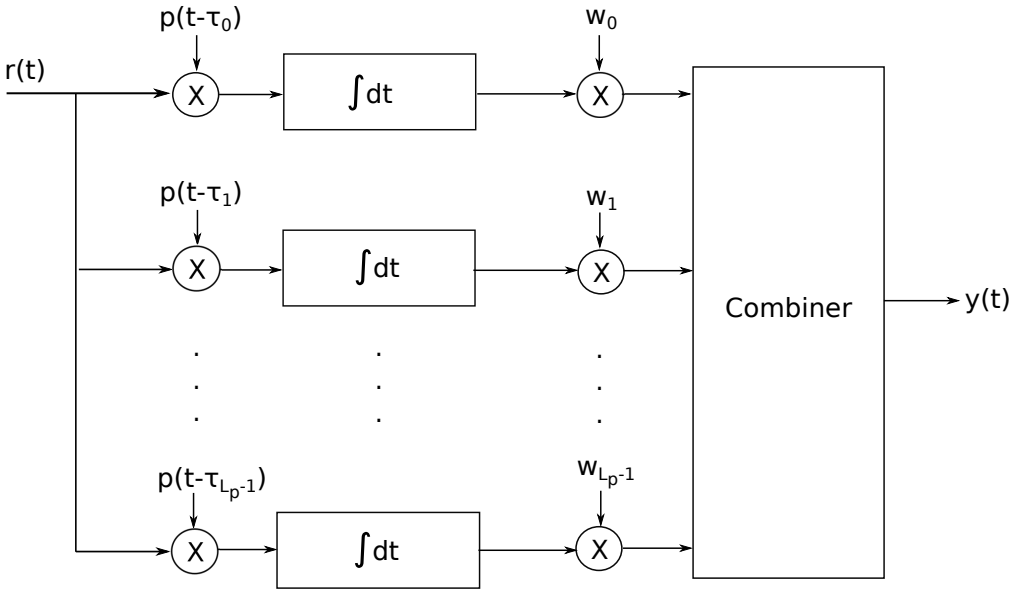

Figure 2.24: Rake receiver.

- *Equal Gain Combining (EGC)*

  EGC [6] [66] is a suboptimal, low complex technique, which does not require channel estimation. EGC assigns equal weights to all multipath components, resulting in Rake weights $\mathbf{w} = (w_0, w_1, ..., w_{L_p-1})$, where $w_i = 1$ for $i = 0, 1, ..., L_p - 1$.

- *Maximal Ratio Combining (MRC)*

  MRC [6] [66] is the optimal combining scheme. It requires knowledge of the channel state information at the Rake, hence it is more complex than EGC. MRC has higher performance gain than EGC. Assuming perfect CSI, the Rake weights are assigned as $w_i = h_i$ for $i = 0, 1, ..., L_p - 1$.

- *Selection Combining (SC)*

  SC [6] [66] involves selecting the branch that has the highest instantaneous SNR out of the $L_p - 1$ branches in the Rake. This is a much less complex scheme where the remaining Rake branches are ignored. The Rake weight in this case is $w_i = h_i$ for $i = max(\mathbf{H})$.

2.9 UWB CHANNEL MODEL

The UWB multipath channel has delay spreads significantly greater than the symbol length, resulting in ISI. This makes signal detection a challenge and requires complex equalisation/detection techniques. In general, due to the time limited nature of UWB pulses and the inter-symbol interference (ISI) caused by the channel, the received signal may consist of many uncorrelated and correlated signal copies (affected by amplitude attenuation and phase distortions) of the transmit pulse. To simplify analysis, the arriving multipath copies are generally considered to be uncorrelated.

A generalized multipath channel model was proposed in [98] by Turin and further developed in [97]. The model was based on experiments to further study the statistics of the signal transmission in an urban outdoor environment. These experiments involved the transmission and reception of narrow pulses at frequencies of 488 MHz, 1280 MHz and 2.9 GHz. The results suggested that the multipath signals follows a 'modified' Poisson arrival process and the amplitude distribution (or path gain/strength) follows a log-normal distribution. The 'modified' Poisson process reflects that initial paths arrive in groups at the receiver. Turins model was further investigated in [99] and [100]. The

model [98] which represents the received signal can be written as

$$p(t) = \sum_{k=0}^{\infty} a_k s(t - t_k) e^{j\theta_k} + n(t), \tag{2.16}$$

where $s(.)$ denotes the transmitted signal, k represents the number of paths, a_k is the gain of the kth path, t_k denotes the path delay and θ_k represents the random phase. $n(t)$ is the additive White Gaussian noise.

In [96] an indoor multipath channel model was proposed by Saleh and Valenzuela. Their experiments used radar like low power pulses having 10 ns pulse widths with a repetition period of 600 ns, in an indoor (office) environment. The result of their experiment was the formulation of a statistical channel model for indoor radio communication, now commonly known as the S-V channel model. The S-V model borrows concepts from the multipath propagation model originally proposed by Turin et al in [97].

The S-V model can be applied to UWB indoor communication because the received IR-UWB signal exhibits a similar multipath characteristic. IR-UWB pulses have the same time and frequency characteristics as those used to develop the S-V model. At the receiver the signal is received in 'clusters' and within each cluster are resolvable signals or 'rays' having an exponentially decreasing amplitude trend with respect to time. Successive clusters exhibit an exponentially decreasing amplitude with time as well, however the exponential decay rate of clusters and rays are different. The clusters are the result of the building structure and the signals or 'rays' within a cluster are the result of objects between the receiver and transmitter. Both follow a Poisson arrival process with fixed rate Λ for the clusters and λ for the individual rays within a cluster. There are generally many rays within each cluster hence, $\lambda >> \Lambda$. let T_l be the arrival time of the lth cluster, where $l = 0, 1, 2, ...$ Let τ_{kl} denotes the kth ray's arrival time (measured from the beginning of the lth cluster). The inter-arrival exponential probability density functions describing T_l and τ_{kl} are given by

$$p(T_l|T_{l-1}) = \Lambda \; exp[-\Lambda(T_l - T_{l-1})] \quad for \; l > 0, \tag{2.17}$$

$$p(\tau_{kl}|\tau_{(k-1)l}) = \lambda \; exp[-\lambda(\tau_{kl} - \tau_{(k-1)l})] \quad for \; k > 0. \tag{2.18}$$

The S-V channel model impulse response is given by

$$h(t) = X \sum_{l=0}^{L_c} \sum_{k=0}^{L_r} h_{kl} e^{j\theta_{kl}} \delta(t - T_l - \tau_{kl}), \tag{2.19}$$

where L_c and L_r represent the number of clusters and rays, respectively. The h_{kl} are statistically independent random variables following an exponential distribution and denote the path gains of the k^{th} ray within the l^{th} cluster. Log-normal fading is applied to each cluster and ray. θ_{kl} is the phase of the k^{th} ray in the l^{th} cluster. T_l is the arrival time of the l^{th} cluster. τ_{kl} is the delay associated with the k^{th} ray in the l^{th} cluster. X represents Rayleigh fading.

The IEEE 802.15.3a UWB multipath channel model [25] [26] [28] is used in this thesis. An alternate UWB channel model is proposed in [112], which takes into account antenna effects. Our work could be extended to include antenna effects, but this was outside the scope of this thesis. We consider the standard IEEE UWB channel model. The UWB channel model proposes several sets of different channel conditions for UWB communications. The channel models range from line of sight (LOS) to non-line of sight (NLOS) multipath channels, with varying multipath component densities. Since the UWB channel model is a real channel, (2.19) is modified by replacing $e^{j\theta_{kl}}$ with $\beta_{kl} \in \{-1, 1\} \, \forall \, k, l$ to account for random phase inversion in the UWB real channel, and then replacing h_{kl} with α_{kl} where $\alpha_{kl} = \zeta_l \, \rho_{kl} \, \beta_{kl}$. Here, ζ_l represents the fading associated with the l^{th} cluster and ρ_{kl} represents the fading associated with k^{th} ray of the l^{th} cluster both of which follow log-normal fading. Then (2.19) can be reduced to the simple form of

$$h(t) = X \sum_{l=0}^{L_c} \sum_{k=0}^{L_r} \alpha_{kl}\, \delta(t - T_l - \tau_{kl}). \tag{2.20}$$

The IEEE 802.15.3a UWB multipath channel model is used for high data channel modelling (20 Mbit/s or more) [5] [25] [26]. The standardised channel model is focused on communications within indoor distances of 10m and between the frequency range of 3 GHz to 10 GHz. The four channel models are channel model 1 (CM-1), channel model 2 (CM-2), channel model 3 (CM-3) and channel model 4 (CM-4). Except CM-1 which is line of sight (LOS), the remaining three channel models are non-line of sight (NLOS). In addition, CM-1 is the least dense channel and CM-4 is the most dense channel model with longer delay spread and greater number of multipath components. Table 2.1 shows the parameters used for the multipath channel models 1 to 4 with typical delay spreads of the channel models ranging from 100 ns to 200 ns. Moving horizontally across the table we note an increase in the values of parameters. This indicates that not only does the arrival rate of clusters increase but their decay times increases as well increasing the channel impulse response delay spread and multipath component density.

Model Parameters	CM-1	CM-2	CM-3	CM-4
Λ (1/nsec)	0.0233	0.4	0.0667	0.0667
λ (1/nsec)	2.5	0.5	2.1	2.1
Γ (cluster decay factor)	7.1	5.5	14.00	24.00
γ (ray decay factor)	4.3	6.7	7.9	12
σ_1 (dB)	3.3941	3.3941	3.3941	3.3941
σ_2 (dB)	3.3941	3.3941	3.3941	3.3941
σ_x (dB)	3	3	3	3

Table 2.1: IEEE 802.15.3a channel model Parameters.

2.10 APPLICATIONS OF ULTRA-WIDEBAND TECHNOLOGY

Due to the large spectrum available to ultra-wideband devices a number of applications can be realized. The main applications are in communications, radar and imaging,

1. Wireless Communications and Networking - information exchange or wireless sensor networks. UWB communication can be used for short range indoor communication or in an outdoor wireless environment. UWB relays can be used instead of wires or amplifiers in areas where a wired service is not feasible [28].

2. Impulse Radar / Vehicular Radar - can provide very high resolution. This allows for tracking of small targets and accurate distance determination [113] [114]. It is also used for monitoring the level of liquids in a tank or objects in the ground.

3. Imaging - can provide through wall imaging or medical imaging. Sub-pico second pulses can give good resolution [28].

4. Positioning Systems - UWB pulses can aid in position localization with centimetre level accuracy and a range of about 25 meters [37].

5. Body Area Networks (BANs) - These consist of a number of nodes placed at various distances on the human body. These can eliminate the need for wired nodes or textiles that are pre-wired and hence cause less discomfort or movement restrictions to the patient [48], [5].

2.11 SUMMARY

This chapter provides an overview of UWB techniques out of which M-ary PPM IR-UWB is further developed in the remaining chapters of this thesis. Both frequency and time domain techniques are presented with the thesis focus being on uncoded time domain IR-UWB. PPM based orthogonal modulation is preferred over bit by bit signalling or the more complex higher M order schemes so as to increase throughput and

have a less complex receiver structure. An ML detection scheme is introduced for PPM IR-UWB detection in an AWGN channel. The complexities of multipath propagation and the UWB channel model are presented and discussed. The multipath UWB channel has long delay spread and dense multipath components making demodulation a challenge. To counter this a suitable receiver called the Rake, which has many possible configurations for signal demodulation in a multipath channel is investigated.

The remainder of the thesis develops and evaluates a PPM based IR-UWB using a two dimensional scheme called carrierless amplitude phase modulation (CAP). System performance results are presented for both additive White Gaussian noise (AWGN) and the IEEE 802.15.3a channel models 1 (CM-1) and 4 (CM-4) using matched filter and Rake receiver structures, respectively. After presenting the performance under assumptions of ideal synchronization, in Chapter 5 the performance of PPM-CAP IR-UWB using a feed-forward data-aided (DA) synchronization scheme is explored and described.

Chapter 3

M-ARY PPM-CAP IR-UWB IN WHITE NOISE

3.1 INTRODUCTION

Chapter 2 provided a brief introduction to M-ary orthogonal modulation schemes. It showed that the benefits offered are simplicity and adequate data rate. One such M-ary orthogonal modulation scheme is pulse position modulation (PPM), which can be used in IR-UWB systems [12] [18] [28] [53] [54] [58] [115]. A M-ary PPM based IR-UWB scheme requires no phase information at the receiver because the presence or absence of a pulse in the intended pulse slot corresponds to the transmitted data. However, as with all digital systems, PPM IR-UWB requires synchronization but does avoid the complexities of phase and frequency synchronization that are required for most carrier based communication systems.

In this chapter, we extend PPM IR-UWB for use with carrierless amplitude phase modulation (CAP) assuming for the present an additive white Gaussian noise (AWGN) channel. The theoretical performance of PPM in AWGN is well documented [93], [92]. The resulting two dimensional scheme is called PPM-CAP IR-UWB and allows for increased data rates without increasing system complexity.

This chapter first discusses the bit error rate (BER) for a carrierless PPM system and then compares it with that of IR-UWB based on M-ary PPM. CAP is then introduced and the error rate results for a PPM IR-UWB system based on CAP are presented. Finally, conclusions are presented for the simulated results.

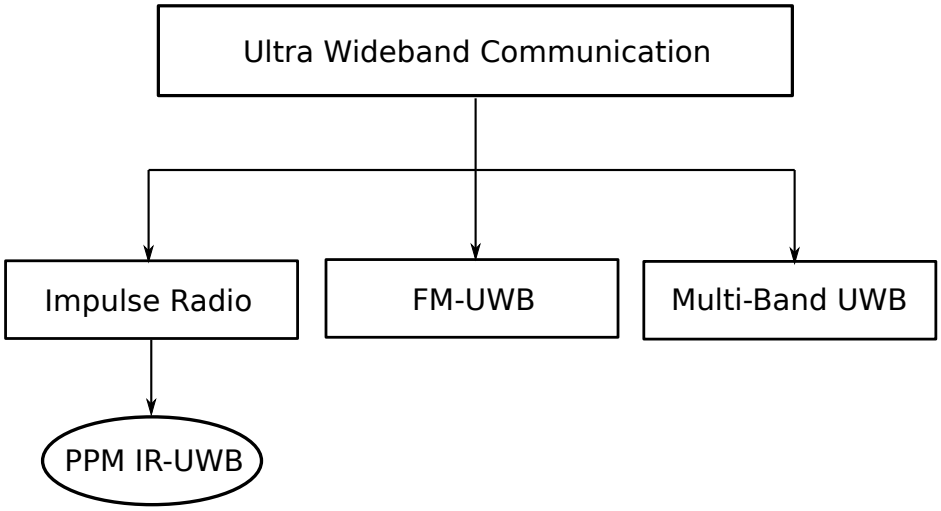

Figure 3.1: PPM IR-UWB.

Figure 3.1 presents a general overview of UWB implementation via different schemes which are reviewed in Chapter 2. It shows PPM IR-UWB is a time domain based scheme which will be considered in the rest of this thesis.

3.2 M-ARY PPM IR-UWB

The performance of M-ary PPM in AWGN has been described [92] [93] as being monotonically decreasing with the signal to noise ratio (SNR). M-ary PPM is an orthogonal modulation transmission scheme, where each symbol consists of M pulse slots with a pulse occupying one of the M pulse slots as shown in Figure 3.2. The pulse is denoted by *p(t)* and is time limited to the duration of a pulse slot. We consider uncoded M-ary PPM. An M-ary PPM scheme transmits k bits per symbol. The number of possible symbols is denoted by $M = 2^k$. The transmit M-ary PPM signal is represented by

$$s_n(t) = \sqrt{E_s}p(t - n(T_s) - a_n(T_c)) \quad n(T_s) \leq t \leq (n+1)(T_s) \forall\, n, \tag{3.1}$$

where E_s represents the pulse energy, $p(.)$ the pulse shape and n the n^{th} symbol. T_c denotes the pulse slot duration within a symbol and nT_s denotes the symbol start time.

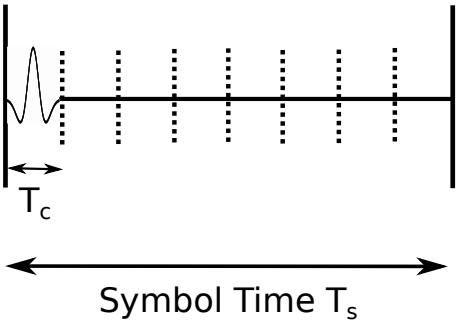

Figure 3.2: An example of a 8-PPM IR-UWB transmitted symbol.

$a_n \in \{0, 1, 2, ..., M-1\}$ denotes the slot number occupied by the data pulse. A M-ary PPM IR-UWB scheme can be vectorially defined as

$$\begin{aligned} a_0 &= (\sqrt{E_s}, 0, 0, \ldots, 0) \\ a_1 &= (0, \sqrt{E_s}, 0, \ldots, 0) \\ &\vdots \\ a_{M-1} &= (0, 0, 0, \ldots, \sqrt{E_s}), \end{aligned} \tag{3.2}$$

where $M = 2^k$ and the possible transmitted symbols $a_n \in 0, 1, 2, ..., M-1$ are assumed to have equal energy E_s and to be independently distributed. The number of dimensions in the vector signal space is denoted by N and the signal set is denoted by M. For an orthogonal scheme such as PPM $M = N$, i.e. there is one signal per dimension. Considering a binary orthogonal scheme we have $M = N = 2$ and the signal set becomes,

$$\begin{aligned} a_0 &= (\sqrt{E_s}, 0) \\ a_1 &= (0, \sqrt{E_s}), \end{aligned} \tag{3.3}$$

where a_0 and a_1 have equal energy and are independently distributed. The received PPM IR-UWB signal can then be written as

$$r_n(t) = \sqrt{E_s} p(t - n(T_s) - a_n(T_c)) + w(t), \tag{3.4}$$

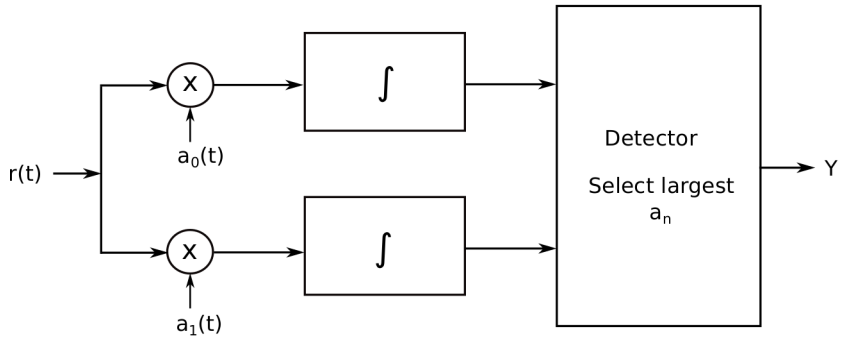

Figure 3.3: Correlation receiver.

where $n(T_s) \leq t \leq (n+1)(T_s) \forall n$. It can be written in compact form [94]

$$r_n(t) = s_n(t) + w(t), \tag{3.5}$$

which can be re-written vectorially as

$$\mathbf{r} = \mathbf{s} + \mathbf{w}, \tag{3.6}$$

where $\mathbf{r}$ is the received observation vector based upon which a decision is made and $\mathbf{s}$ is the transmitted symbol vector. $\mathbf{s}$ represents the signal set $[a_0, a_1]$ where a_0 and a_1 are independently distributed and given by (3.3). The components of $\mathbf{r}$ are denoted by $r_0 = [\sqrt{E_s} + n_0, n_1]$ and $r_1 = [n_0, \sqrt{E_s} + n_1]$, where n_0 and n_1 are statistically independent AWGN components. Based on the optimum receiver shown in Figure 3.3, the correlation metric obtained in (2.14) is modified for $M = 2$ and denoted as $C(\mathbf{r}, a_0)$ and $C(\mathbf{r}, a_1)$. The probability of error that a_0 is transmitted and a_1 is received is then given by [93]

$$P(\epsilon|s_0) = P[C(\mathbf{r}, a_1) > C(\mathbf{r}, a_0)] = P[n_1 - n_0 > \sqrt{E_s}]. \tag{3.7}$$

The $P(\epsilon|s_0)$ can be further written as

$$P(\epsilon|s_0) = \frac{1}{\sqrt{2\pi N_0}} \int_{\sqrt{E_s}}^{\infty} e^{(n_1-n_0)^2/2N_0} d\theta, \tag{3.8}$$

where the difference $(n_1 - n_0)$ can be denoted by θ. After substitution and change in limits, $P(\epsilon|s_0)$ can be written as [93]

$$P(\epsilon|s_0) = \frac{1}{\sqrt{2\pi N_0}} \int_{\sqrt{E_s/N_0}}^{\infty} e^{x^2/2}\, dx, \tag{3.9}$$

which can be denoted compactly by $Q\left[\sqrt{E_s/N_0}\right]$. Since it is assumed that all M signals are equiprobable, i.e. $P(\epsilon|s_0) = P(\epsilon|s_1)$, the average probability of error can be expressed as

$$P(\epsilon) = \frac{1}{2}P(\epsilon|s_0) + \frac{1}{2}P(\epsilon|s_1) = Q\left[\sqrt{\frac{E_s}{N_0}}\right]. \tag{3.10}$$

From (3.10), a practical upper bound on performance for an M-ary orthogonal (PPM) system can be given by [92] [16] [93]

$$P[\varepsilon] \leq (M-1)\, Q\left(\sqrt{\frac{E_s}{N_0}}\right) < M\, e^{-E_s/2N_0}. \tag{3.11}$$

The last part of (3.11), i.e. $Me^{-E_s/2N_0}$, clearly demonstrates the asymptotic performance achievable using an orthogonal signal set. Substituting $E_s = kE_b$ and $M = 2^k$, where k denotes the number of bits per symbol and E_b denotes the energy per bit, $P[\varepsilon]$ can be upper bounded as

$$P[\varepsilon] < Me^{-E_s/2N_0} = 2^k e^{-kE_b/2N_0}, \tag{3.12}$$

which can be rewritten as

$$P[\varepsilon] < 2^k e^{-kE_b/2N_0} = e^{-k(E_b/2N_0 - ln\, 2)}. \tag{3.13}$$

The right hand term of (3.13) shows [92] that provided $E_b/N_0 > 2\,ln\,2 \approx 1.39$, increasing k will monotonically decrease $P[\varepsilon]$ of any orthogonal modulation format including M-ary PPM system in AWGN.

3.3 CARRIERLESS AMPLITUDE PHASE MODULATION (CAP)

CAP is a two dimensional passband transmission scheme originally designed for digital subscriber loop (DSL) systems [116], [117], [118]. It's use has been largely superseded by discrete multitone (DMT) systems due to their ability to counter narrowband interference [119]. CAP has not been investigated for applications to IR-UWB. CAP provides increased bandwidth efficiency compared to conventional PPM based IR-UWB and low implementation costs. Wei *et al* in [120] found that it could benefit long range optical fibre networks. A lot of the pioneering work concerning CAP modulation over cable was done by Werner [118], [121].

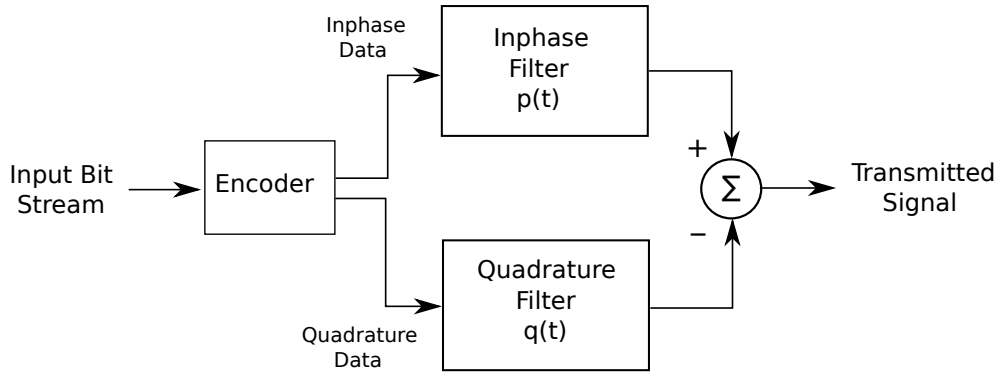

Figure 3.4: Carrierless amplitude phase modulation transmitter.

M-ary CAP is based on M-ary quadrature amplitude modulation (M-QAM) [121], but the implementation technique is quite different [122]. The inphase and quadrature signals are the Hilbert transform of each other and the CAP transmitted signal has a carrierless form. The inphase and quadrature signals provide two independent and orthogonal data paths. In an IR-UWB scheme, CAP can be designed to be carrierless by use of pulse shaping inphase and quadrature filters. An optimum receiver in AWGN for

CAP contains filters matched to the in-phase and quadrature pulses. Figure 3.4 shows the transmitter structure [94] [123] of a CAP system. In AWGN, a possible receiver implementation of CAP is shown in Figure 3.5.

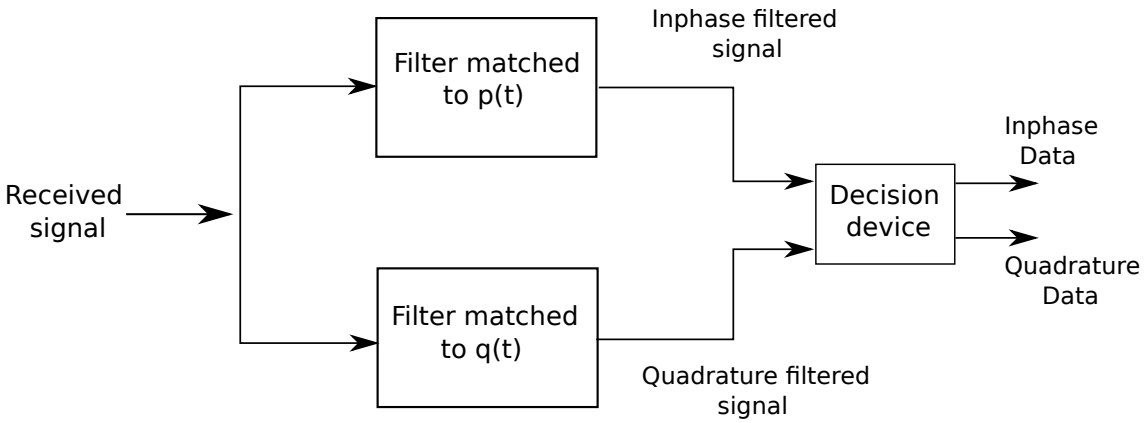

Figure 3.5: Carrierless amplitude phase modulation receiver.

The inphase pulse is denoted by $p(t)$ and the orthogonal Hilbert pulse by $q(t)$ as shown in Figure 3.6. The pulses are related according to

$$q(t) = p(t) \otimes \frac{1}{\pi t} = \int_{-\infty}^{\infty} \frac{p(t)}{t-\tau} dt, \tag{3.14}$$

where $\otimes$ denotes convolution and $\int_{-\infty}^{\infty} p(t)q(t)dt = 0$. We can represent the overall signal as $s(t) = p(t) + q(t)$. Although there are many possibilities for pulse shapes [73] [124] [86] [89] [90], here we use the Scholtz monocycle [12] [28] as the inphase pulse $p(t)$ for $0 \leq t \leq T_p$. It can be written as

$$p(t) = \left\{ \left[1 - 4\pi \left(\frac{t}{T_p} \right)^2 \right] \exp\left(-2\pi \left(\frac{t}{T_p} \right)^2 \right) \right\} rect\left(\frac{t}{T_p} \right), \tag{3.15}$$

where the *rect* function is used to window the pulse to within a single pulse duration. The Scholtz monocycle is used because it can fit most spectral masks [50] and has been extensively used in the literature [12] [58] [18]. The choice of pulse width is dependent on the system design. Pulse widths as narrow as 0.16 ns have been used while pulse

widths as wide as 2 ns are presented in the literature [67] [125–130]. In this thesis the pulse width is set to 1ns, which is an arbitrary choice.

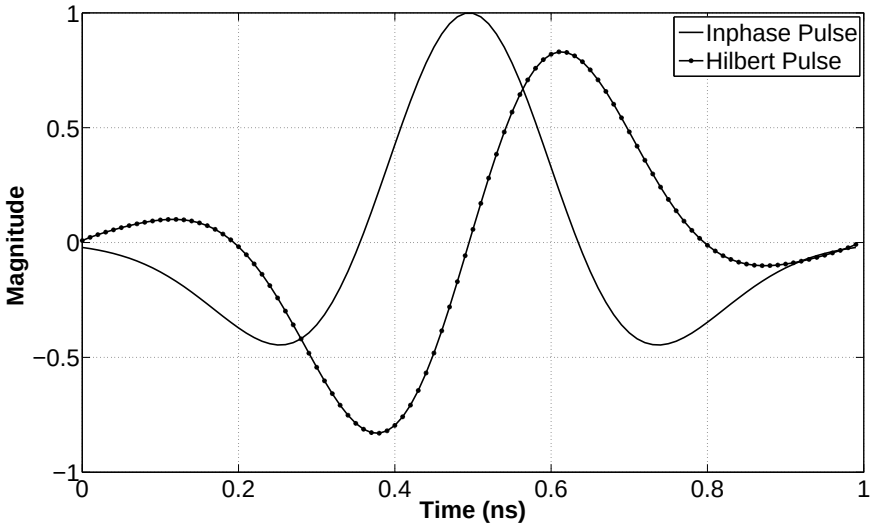

Figure 3.6: Scholtz monocycle pulse and its Hilbert transform.

3.4 M-ARY PPM IR-UWB BASED ON CAP

The basic CAP scheme of [94] proposes a transmitter based on a pair of filters and an encoder as shown in Figure 3.4. The encoder maps the data into symbols and then onto the inphase and quadrature channels. The purposes of the in-phase filter *p(t)* and the quadrature filter *q(t)* with respect to UWB transmission are two fold,

1. To shape the transmitted pulse bandwidth so as to remain within the designated band.

2. To generate pulses which are orthogonal to each other, i.e. $\int p(t)q(t)dt = 0$. An orthogonal or quadrature pulse $q(t)$ may be obtained by taking the Hilbert transform of the in-phase pulse $p(t)$. The combined signal $s(t)$ may be written as $s(t) = p(t) + q(t)$ [95].

The same concept holds for a M-ary block orthogonal coded scheme based on M-CAP. This can be considered to be a two dimensional form of pulse shape modulation [12], [14], [15], where the orthogonal pulse is obtained via the Hilbert transform. From Figure 3.4, the encoder separates the data stream $\mathbf{x} = (x_0, x_1, x_2, x_3, ..., x_\infty)$ into two streams a_n and b_n. These are input to the in-phase and quadrature filters. Both a_n and b_n are considered to be equiprobable random symbols from the set $\{0, 1, ..., M-1\}$. The transmitted signal $s_n(t)$ can then be written as

$$\begin{aligned} s_n(t) &= (\sqrt{E_s/2})p(t - n(T_s) - a_n(T_p)) \\ &\quad + (\sqrt{E_s/2})q(t - n(T_s) - b_n(T_p)) \\ &= s_n^a(t) + s_n^b(t), \end{aligned} \tag{3.16}$$

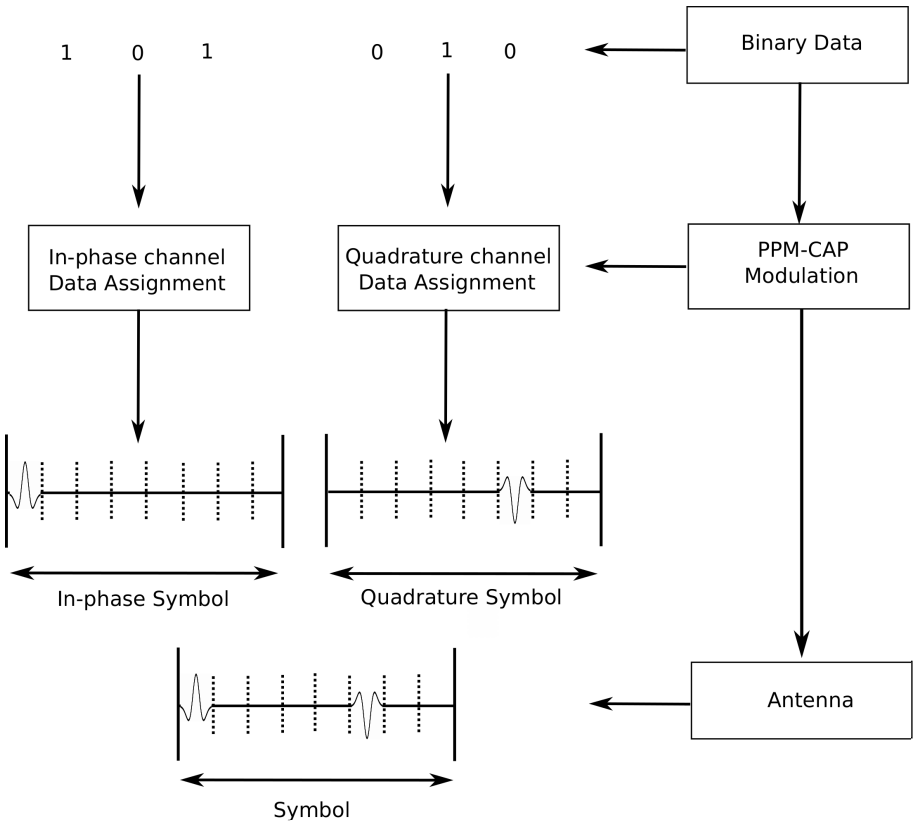

Figure 3.7: 8-ary PPM-CAP IR-UWB transmitted symbols.

where $E_s/2$ represents the pulse energy. n represents the n^{th} symbol where $n(T_s) \leq t \leq (n+1)(T_s) \forall n$. $a_n(T_p)$ and $b_n(T_p)$ specify the inphase and quadrature pulse positions within the n^{th} symbol.

Figure 3.7 shows the transmitter structure and a transmitted symbol for an 8-ary PPM-CAP IR-UWB system. PPM-CAP IR-UWB doubles data rate compared to the corresponding PPM IR-UWB scheme.

3.5 SIMULATION RESULTS

This section presents simulation results for M-ary PPM IR-UWB and M-ary PPM-CAP IR-UWB schemes in AWGN. The pulse used is the Scholtz monocycle with a time duration of 1 ns. Recall, Figure 3.6 showed both the Scholtz monocycle and its Hilbert transform, i.e. the quadrature pulse. Each transmitted frame consists of 200 symbols.

From (3.11) we get an analytical $P(\epsilon)$ for M-ary PPM which can be used as an perfor-

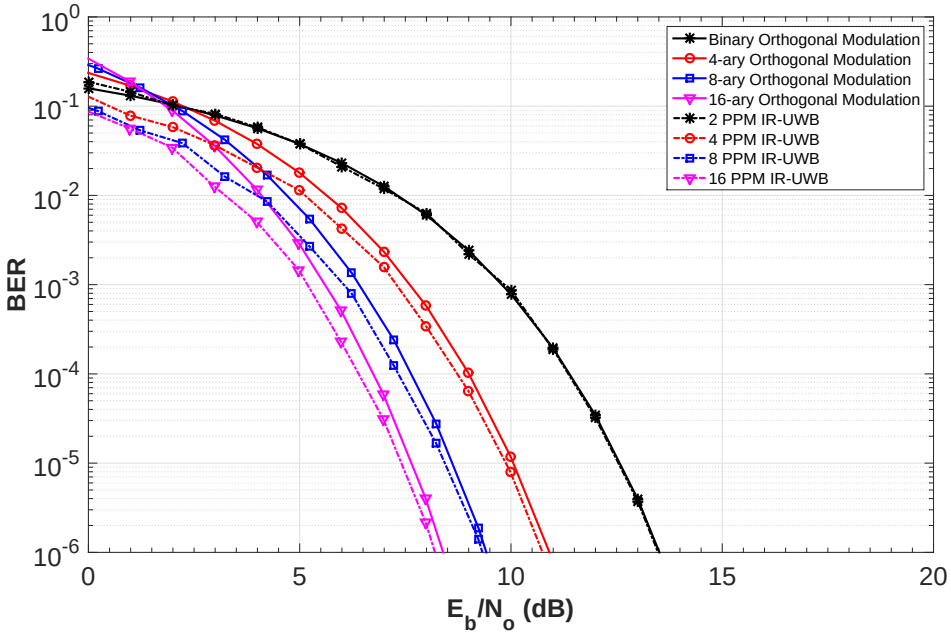

Figure 3.8: Simulated M-ary PPM IR-UWB plots and M-ary orthogonal modulation error plots from (3.11).

mance upper bound for M-ary PPM IR-UWB scheme. Figure 3.8 shows the error rate performance of the M-ary PPM IR-UWB scheme, with $M = 2, 4, 8$ and 16 compared with the upper bound obtained from (3.11) in an AWGN channel. It plots the simulated BER against E_b/N_o, where $E_b = E_s/k$ is the energy per bit and k represents the bits per symbol. The number of possible symbols is then $M = 2^k$.

From Figure 3.8 we see that M-ary PPM IR-UWB performance follows a similar asymptotic trend to the $P(\epsilon)$ plots obtained from (3.11). The upper bound is tight for increasing E_b/N_0 values. It can be observed that at a BER of 10^{-4}, the 2-ary scheme has performance which is approximately 6 dB worse than the 16-ary scheme. Since E_s is fixed for all schemes, the higher order scheme will always have a lower E_b than a lower order orthogonal scheme. As with M-ary orthogonal modulation we observe a clustering in the BER plots of PPM IR-UWB with increasing M which is a typical behaviour of orthogonal schemes. Figure 3.8 clearly shows the advantage of using a higher M modulation scheme mainly because of the increased number of bits per symbol and better

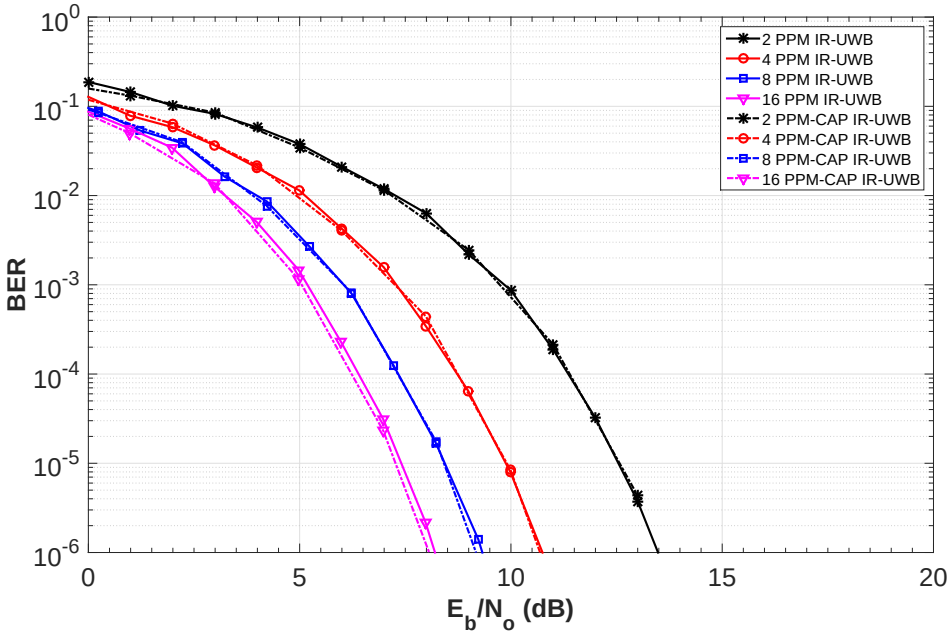

Figure 3.9: M-ary PPM and M-ary PPM-CAP in AWGN.

BER performance in terms of energy per transmitted bit.

The BER performance of M-ary PPM-CAP IR-UWB is shown in Figure 3.9 which show plots for 2, 4, 8 and 16 PPM-CAP IR-UWB and compares it with M-ary PPM IR-UWB. All plots are for a pulse width of 1ns using the Scholtz monocycle and its Hilbert transform. It is observed that both have similar error performance plots and the throughput of M-ary PPM-CAP IR-UWB is double that of M-ary PPM IR-UWB. M-ary PPM-CAP shows clustering effect with increasing M, i.e. the performance gain between successive error plots diminishes with increasing M. From Figure 3.9, at a BER of 10^{-4}, 16 PPM-CAP IR-UWB shows an improvement of approximately 6 dB compared to 2 PPM-CAP IR-UWB, but the performance improvement when compared to 8 PPM-CAP IR-UWB is approximately 1 dB.

3.6 CONCLUSIONS

In this chapter we have described M-ary PPM IR-UWB and M-ary PPM-CAP IR-UWB schemes and have evaluated their performance in an AWGN channel. A matched filter based detector is used for both schemes. We observe that M-ary PPM-CAP IR-UWB has similar BER performance to M-ary PPM IR-UWB. The main advantage of using PPM IR-UWB based on CAP is that it allows double the data rate.

Studying the performance of IR-UWB based on CAP in an AWGN channel is beneficial and provides insight into the usefulness of the transmission scheme. However, for it to be practically usable it must be investigated in a multipath channel. The UWB channel is often modelled as a dense multipath channel having a time duration significantly longer than the transmitted symbol time. Chapter 4 presents PPM IR-UWB and PPM-CAP IR-UWB transmission using the IEEE 802.15.3a multipath channel models CM-1 and CM-4.

Chapter 4

M-ARY PPM-CAP IR-UWB IN MULTIPATH CHANNEL

4.1 INTRODUCTION

This chapter starts by developing a multipath channel model for PPM IR-UWB based on the IEEE 802.150.3a multipath CM-1 and CM-4 channels. Then a receiver is developed for M-ary PPM IR-UWB following which we extend the work to the M-ary PPM-CAP signal transmission format and develop its system equations. Two transmission formats are presented for PPM-CAP IR-UWB. Performance results for a variety of receiver parameters, for both M-ary PPM IR-UWB and M-ary PPM-CAP, are presented and system trade-offs are evaluated. Then conclusions are drawn.

4.2 M-ARY PPM IR-UWB IN MULTIPATH CHANNEL

Figure 4.1 presents an uncoded PPM IR-UWB scheme. The binary input is first grouped together to form symbols which are then assigned pulse slots and input to a pulse shaper. The pulse used in this thesis is the Scholtz monocycle which is transmitted after the pulse shaper block. The received multipath signal is passed through a Rake which is

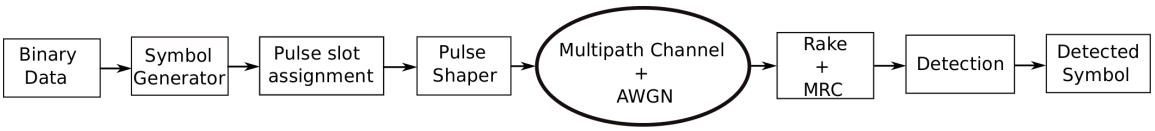

Figure 4.1: PPM IR-UWB system overview.

matched to the transmit pulse shape. The signal is then maximal ration combined (MRC) and input to the detector which chooses the largest based on ML criteria.

An M-ary PPM scheme transmits k-bit data symbols with each symbol occupying $M = 2^k$ pulse slots. We define the multipath channel transmission scheme in terms of *pulse slots*, *symbols*, *frames* and *guard time* between successive symbols for ISI mitigation denoted by T_c, T_s, T_f and T_g, respectively. Generally, $T_c < T_s < T_g < T_f$. The UWB pulse *p(t)* has time duration $T_p = T_c$. A pulse occupies only one of the M possible pulse slots. A *frame* consisting of N_s symbols has a duration of $T_f = N_s(T_s + T_g)$. For simplicity, we assume $T_g = n_g \times T_s$, where $n_g \in \{0, 1, 2, ..., N_g\}$ and N_g is a suitable number chosen by the system designer. We denote $T_{channel}$ as the duration of the multipath channel impulse response. A practical limit on N_g is $N_g \geq \frac{T_{channel}}{T_s}$ to ensure the received signal has sufficiently low ISI. Adequate T_g between successive symbols allows sufficient time for the pulse tails to decay to a negligible value. Therefore, the frame duration can be set to $T_f = 2^k N_s T_c(1 + n_g)$.

The position of the pulse within a symbol is represented by a variable $a \in \{0, 1, ..., M-1\}$ and is independently identically and uniformly distributed. The input bit stream to the transmitter, $\mathbf{x} = (x_0, x_1, x_2, x_3, ..., x_n)$, is coded onto a sequence of the symbol a which is PPM modulated onto a sequence of pulses $p(t)$. The transmitted signal $s_n(t)$ can then be written as

$$s_n(t) = \sum_{n=0}^{\infty} \sqrt{E_s} p(t - n(T_s + T_g) - a_n T_p), \tag{4.1}$$

where $n(T_s+T_g) \leq t \leq (n+1)(T_s+T_g) \forall\, n$, E_s is the symbol energy and $p(.)$ is the pulse shape. The term $n(T_s + T_g)$ includes the symbol guard time T_g and denotes the start of the n^{th} symbol. The term $a_n T_p$ denotes the pulse slot occupied by the data pulse such that $a_n T_p \in \{0, T_c, ..., (M-1)T_c\}$. The received signal is given by

$$r_n(t) = s_n(t) \otimes h(t) + w(t), \tag{4.2}$$

where $n(T_s + T_g) \leq t \leq (n+1)(T_s + T_g) \, \forall \, n$ and $w(t)$ is additive white Gaussian noise (AWGN) having power spectral density (PSD) $N_o/2$, $h(t)$ is the multipath channel impulse response and $\otimes$ denotes convolution.

From Chapter 2, the IEEE 802.15.3a channel model impulse response [26] [131] is represented as

$$h(t) = X \sum_{l=0}^{L_c} \sum_{k=0}^{L_r} \alpha_{kl} \, \delta(t - T_l - \tau_{kl}), \tag{4.3}$$

where L_c and L_r represent the number of clusters and rays, respectively. The α_{kl} are statistically independent random variables following an exponential distribution and denote the path gain of the k^{th} ray within the l^{th} cluster. T_l is the arrival time of the l^{th} cluster. τ_{kl} is the delay associated with the k^{th} ray in the l^{th} cluster and X represents overall log-normal fading which can be neglected for most purposes as it is a slowly time varying parameter.

The optimum receiver for a PPM IR-UWB system in a multipath environment consists of a bank of matched filters/correlators each matched to $p(t-\tau_l)$, where τ_l in general denotes the delay of the l^{th} channel multipath component. A receiver that essentially does this is the Rake receiver [102, 132, 133]. Ideally, the number of Rake matched filter/correlator branches (alternatively referred to as Rake taps or Rake fingers) equals the number of detectable channel multipath components, $\mathbf{h} = [h_1, h_2, ..., h_{L_{channel}}]$, where $L_{channel}$ denotes the number of components. We represent the individual channel multipath gains by $\alpha_i = h_i$ for $i = 1, 2, ..., L_{channel}$. In practice only the first L_p received multipath components are considered, where in general $L_p << L_{channel}$. This results in a Rake structure with L_p taps. The larger the number of taps, the greater the useful energy that can be captured by the Rake (at the cost of increased complexity). The output of each branch is maximal ratio combined (MRC) [102] with the weights denoted by $\mathbf{w}_{rake} = [w_1, w_2, ..., w_{L_p}]$, where $w_i = \alpha_i$ for $i = 1, 2, ..., L_p$. The received signal is

obtained by substituting (4.1) and (4.3) into (4.2) and can be written as

$$r(t) = (\sqrt{E_s}) \sum_{n=0}^{\infty} \sum_{l=0}^{L_c} \sum_{k=0}^{L_r} \alpha_{kl}\, p(t - n(T_s + T_g) - a_n T_p - T_l - \tau_{kl}) + w(t), \tag{4.4}$$

where we assume that all received symbols are statistically equal and X is ignored. To simplify analysis, consider only the first received symbol and ignore the ensuing $n(T_s+T_g)$ symbols. The channel impulse response $h(t)$ can then be reduced to a standard representation (tap-delay line) of a multipath model i.e. $\sum_{l=0}^{L_{channel}} \alpha_l\, \delta(t - \tau_l)$ [98], [97], where l now denotes the individual multipath components. We may then rewrite (4.4) as

$$r(t) = (\sqrt{E_s}) \sum_{l=0}^{L_{channel}} \alpha_l\, p(t - aT_p - \tau_l) + w(t), \tag{4.5}$$

where α_l represents the weights of the multipath components and $L_{channel}$ represents the number of received multipath components resolved. The MRC Rake outputs for the m^{th} pulse slot can then be written as

$$y_m^{a'} = \sum_{l_{rake}=0}^{L_p-1} w_{l_{rake}} \qquad \left(\int_{mT_p+\tau_{l_{rake}}}^{mT_p+T_p+\tau_{l_{rake}}} r(t) x_{ref}^{p(t)}(t - mT_p - \tau_{l_{rake}}) dt \right), \tag{4.6}$$

where $x_{ref}^{p(t)}$ is the reference pulse template. The M MRC Rake outputs corresponding to each symbol can be written in vector form as

$$\mathbf{Y}^{\mathbf{a}'_\mathbf{i}} = [y_0^{a'}, y_1^{a'}, ..., y_{M-1}^{a'}]. \tag{4.7}$$

Finally, the ML detected data estimate is calculated for each symbol as

$$a' = arg \max_m \mathbf{Y}^{\mathbf{a}'}. \tag{4.8}$$

4.3 M-ARY PPM-CAP MODULATION FORMAT A - T_G BETWEEN SYMBOLS

In Chapter 3 we saw that PPM-CAP is an extension of PPM IR-UWB where we use the Hilbert transform to generate an orthogonal pair of the pulses, i.e. the inphase pulse and Hilbert transform. The Scholtz monocycle is used as the inphase pulse. Figure 4.2 shows a 2 PPM-CAP IR-UWB symbol with modulation format A. Figure 4.2 is valid for a PPM IR-UWB scheme as well.

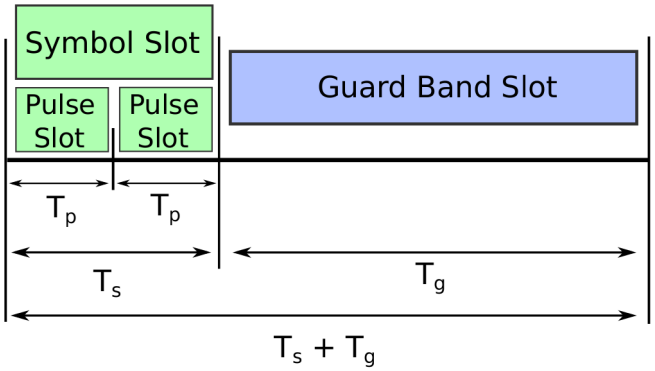

Figure 4.2: Modulation format A. 2 PPM-CAP IR-UWB symbol with guard band.

Guard bands are placed after each symbol to allow the channel impulse response enough time to decay sufficiently to have minimal impact on ensuing symbols. The choice of T_g is crucial to system performance and its effect is evaluated in the results section of this chapter. The effective symbol time is then $T_s + T_g$.

The input bit stream $\mathbf{x} = (x_0, x_1, x_2, x_3, ..., x_n)$ to the transmitter is demultiplexed into two parallel streams by the encoder. One stream consists of even indexed bits and the other of odd indexed bits. The two parallel bit streams are denoted by $a_n = x_n$ (where 'n' denotes the even indexed bits of bit stream $\mathbf{x}$) and $b_n = x_m$ (where 'm' denotes the odd indexed bits of bit stream $\mathbf{x}$). $\{a\}$ and $\{b\}$, are PPM modulated onto the inphase, $p(t)$, and quadrature, $q(t)$, pulses, respectively. The overall signal $s_n(t)$ can then be

written as

$$\begin{aligned} s_n(t) = &\sum_{n=0}^{\infty}(\sqrt{E_s/2})p(t - n(T_s) - a_nT_p) \\ &+ \sum_{n=0}^{\infty}(\sqrt{E_s/2})q(t - n(T_s) - b_nT_p), \end{aligned} \tag{4.9}$$

where $n(T_s) \leq t \leq (n+1)(T_s) \forall\, n,\ a, b \in \{0, 1, ..., M-1\}$ and a_nT_p, b_nT_p specify the pulse positions within the n^{th} symbol. Equation (4.9) denotes the transmitted signal with no guard time T_g between symbols. Guard time is important in channels with long delay spreads as it helps to reduce inter-symbol interference (ISI). After adding the T_g parameter, (4.9) can be re-written as

$$\begin{aligned} s_n(t) = &\sum_{n=0}^{\infty}(\sqrt{E_s/2})p(t - n(T_s + T_g) - a_nT_p) \\ &+ \sum_{n=0}^{\infty}(\sqrt{E_s/2})q(t - n(T_s + T_g) - b_nT_p), \end{aligned} \tag{4.10}$$

where $n(T_s + T_g) \leq t \leq (n+1)(T_s + T_g) \forall\, n$. It can be compactly written as

$$s_n(t) \quad = \quad s_n^a(t) + s_n^b(t), \tag{4.11}$$

where $s_n(t)$ denotes the combined transmitted signal, $s_n^a(t)$ denotes the in-phase transmitted signal and $s_n^b(t)$ denotes the quadrature component of the transmitted signal. The in-phase and quadrature IR-UWB signals are both real signals [66].

A multipath channel correlation receiver or Rake receiver, discussed in Chapter 2, is employed for PPM-CAP. This has two matched filter front ends which are matched to the inphase and quadrature pulse templates, respectively. The number of Rake taps for each is denoted by L_p and the taps are spread over multiple pulse slots to improve multipath energy capture and eventually to increase system performance. In an optimal system, the received pulse shape is taken as the filter template for the Rake. However,

in a practical scenario the receiver will only have knowledge of the transmit pulse shape, hence $p(t)$ and $q(t)$ are used as the Rake receiver filter responses.

$$\begin{aligned} r(t) = (\sqrt{E_s/2}) \sum_{n=0}^{\infty} \sum_{l=0}^{L_c} \sum_{k=0}^{L_r} \alpha_{kl}\, p(t - n(T_s + T_g) - a_n T_p - T_l - \tau_{kl}) \\ + (\sqrt{E_s/2}) \sum_{n=0}^{\infty} \sum_{l=0}^{L_c} \sum_{k=0}^{L_r} \alpha_{kl}\, q(t - n(T_s + T_g) - b_n T_p - T_l - \tau_{kl}) \\ + w(t), \end{aligned} \tag{4.12}$$

where we assume that all received symbols are statistically equal and X is ignored. To simplify analysis, consider only the first received symbol and ignore the ensuing symbols. The channel impulse response $h(t)$ can then be reduced to a standard representation (tapped-delay line) of a multipath model i.e. $\sum_{l=0}^{L_{channel}} \alpha_l\, \delta(t-\tau_l)$ [98], [97], where l now denotes the individual multipath components. We may then rewrite (4.12) as

$$\begin{aligned} r(t) = (\sqrt{E_s/2}) \sum_{l=0}^{L_{channel}} \alpha_l\, p(t - aT_p - \tau_l) \\ + (\sqrt{E_s/2}) \sum_{l=0}^{L_{channel}} \alpha_l\, q(t - bT_p - \tau_l) \\ + w(t), \end{aligned} \tag{4.13}$$

where α_l represents the weights of the multipath components and $L_{channel}$ represents the number of received multipath components resolved. The Rake outputs with respect to m can then be written for the m^{th} pulse slot within the symbol period as

$$y_m^{a'} = \sum_{l_{rake}=0}^{L_p-1} w_{l_{rake}} \qquad \left(\int_{mT_p+\tau_{l_{rake}}}^{mT_p+T_p+\tau_{l_{rake}}} r(t) x_{ref}^{p(t)}(t - mT_p - \tau_{l_{rake}}) dt \right), \tag{4.14}$$

$$y_m^{b'} = \sum_{l_{rake}=0}^{L_p-1} w_{l_{rake}} \qquad \left(\int_{mT_p+\tau_{l_{rake}}}^{mT_p+T_p+\tau_{l_{rake}}} r(t) x_{ref}^{q(t)}(t - mT_p - \tau_{l_{rake}}) dt \right), \tag{4.15}$$

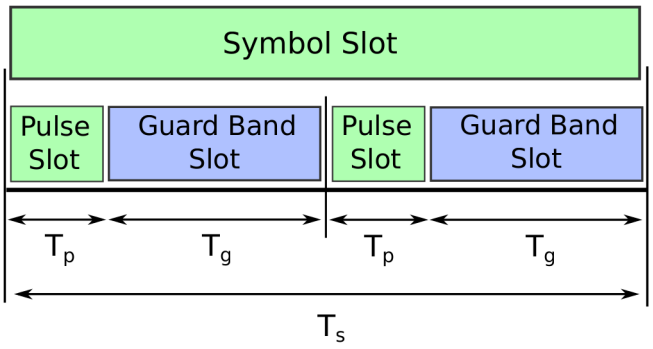

Figure 4.3: Modulation format B. 2 PPM-CAP IR-UWB symbol with guard band.

where $x_{ref}^{p(t)}$ and $x_{ref}^{q(t)}$ are the reference inphase and quadrature pulse templates which are set to be $p(t)$ and $q(t)$, respectively. The MRC Rake outputs can be written in vector form as

$$\mathbf{Y}^{\mathbf{a}'} = [y_0^{a'}, y_1^{a'}, ..., y_{M-1}^{a'}], \tag{4.16}$$

$$\mathbf{Y}^{\mathbf{b}'} = [y_0^{b'}, y_1^{b'}, ..., y_{M-1}^{b'}]. \tag{4.17}$$

Finally, the ML detected inphase and quadrature data estimates for the received symbol, are calculated as

$$a' = arg \max_m \mathbf{Y}^{\mathbf{a}'}, \tag{4.18}$$

$$b' = arg \max_m \mathbf{Y}^{\mathbf{b}'}. \tag{4.19}$$

4.4 M-ARY PPM-CAP MODULATION FORMAT B - T_G WITHIN SYMBOLS

This section discusses the insertion of guard time within the symbol format. Figure 4.3 presents a 2 PPM-CAP IR-UWB symbol diagram with guard bands placed between each pulse slot time. Each pulse slot time duration effectively becomes $T_p + T_g$ rather than just being T_p as in modulation format A. The overall symbol time for modulation format B is then denoted by T_s instead of $T_s + T_g$. While the location T_g changes significantly between the two modulation formats, the time duration required for one symbol inclusive of guard time for both transmitted formats i.e. $MT_p + T_g$ (format A)

and $M(T_p + T_g)$ (format B) is kept the same so as to allow a fair comparison.

To insert guard time T_g within the symbol we need to re-write (4.9) as

$$\begin{aligned} s_n(t) = &\sum_{n=0}^{\infty}(\sqrt{E_s/2})p(t - nT_s - a_n(T_p + T_g)) \\ &+ \sum_{n=0}^{\infty}(\sqrt{E_s/2})q(t - nT_s - b_n(T_p + T_g)), \end{aligned} \tag{4.20}$$

where $n(T_s) \leq t \leq (n+1)(T_s)\,\forall\, n$. It can be compactly expressed as in (4.11). The received signal for this case is obtained by substituting (4.20) and (4.3) into (4.2) and can be written as

$$\begin{aligned} r(t) = &(\sqrt{E_s/2})\sum_{n=0}^{\infty}\sum_{l=0}^{L_c}\sum_{k=0}^{L_r}\alpha_{kl}\, p(t - nT_s - a_n(T_p + T_g) - T_l - \tau_{kl}) \\ &+ (\sqrt{E_s/2})\sum_{n=0}^{\infty}\sum_{l=0}^{L_c}\sum_{k=0}^{L_r}\alpha_{kl}\, q(t - nT_s - b_n(T_p + T_g) - T_l - \tau_{kl}) \\ &+ w(t), \end{aligned} \tag{4.21}$$

where we assume that all received symbols are statistically equal and X is ignored. Considering the first received symbol and a tapped-delay line channel impulse response, the received signal can be written as

$$\begin{aligned} r(t) = &(\sqrt{E_s/2})\sum_{l=0}^{L_{channel}}\alpha_l\, p(t - a(T_p + T_g) - \tau_l) \\ &+ (\sqrt{E_s/2})\sum_{l=0}^{L_{channel}}\alpha_l\, q(t - b(T_p + T_g) - \tau_l) \\ &+ w(t), \end{aligned} \tag{4.22}$$

where α_l represents the weights of the multipath components and $L_{channel}$ represents the number of received multipath components resolved. The Rake outputs for the m^{th} pulse slot are then written as

$$y_m^{a'} = \sum_{l_{rake}=0}^{L_p-1} w_{l_{rake}} \left(\int_{mT_p+\tau_{l_{rake}}}^{mT_p+T_p+\tau_{l_{rake}}} r(t) x_{ref}^{p(t)}(t - m(T_p + T_g) - \tau_{l_{rake}}) dt \right), \quad (4.23)$$

$$y_m^{b'} = \sum_{l_{rake}=0}^{L_p-1} w_{l_{rake}} \left(\int_{mT_p+\tau_{l_{rake}}}^{mT_p+T_p+\tau_{l_{rake}}} r(t) x_{ref}^{q(t)}(t - m(T_p + T_g) - \tau_{l_{rake}}) dt \right), \quad (4.24)$$

where $x_{ref}^{p(t)}$ and $x_{ref}^{q(t)}$ are the reference inphase and quadrature pulse templates. The MRC outputs along with the ML detected inphase and quadrature data estimates are obtained by (4.14) to (4.19).

4.5 SIMULATION RESULTS

In this section, we evaluate the performance of M-ary PPM IR-UWB and M-ary PPM-CAP systems, via simulation, in IEEE CM-1 and CM-4 multipath channel environments. CM-1 is a less dense multipath channel whereas CM-4 exhibits higher multipath density and significantly longer delay spread. The channel is considered to be quasi-static, i.e. time invariant for the duration of a transmitted frame. Plots for comparison of the two system scenarios are shown. Plots for 2, 4 , 8 and 16 PPM and PPM-CAP IR-UWB are plotted for different parameters such as pulse width T_p, guard time T_g and number of Rake taps L_p. The symbol time T_s for the 2, 4, 8 and 16-ary schemes are 2 ns, 4 ns, 8 ns and 16 ns, respectively, unless otherwise stated. There are 200 symbols per frame and $T_p = 1$ ns for all schemes unless otherwise stated. The Rake receiver employs one of 5, 15 or 30 taps. The following steps summarize how the simulation works.

1. Generate random binary data bits.
2. Group bits into the desired M-ary symbols.
3. Use the PPM-CAP block to generate the pulse shapes $p(t)$ and $q(t)$, respectively.

4. Initialize channel parameters Λ,λ, Γ and γ along with cluster arrival time T_l.
5. Generate clusters with arrival rate Λ and decay rate Γ. Arrival time of first cluster is $T_l = \tau_{00} = 0$.
6. First path of first cluster is assigned a mean energy of 1.
7. Generate ray arrival times τ_{kl} within each cluster having inter-arrival rate λ and having exponential decay with rate γ with respect to energy of the first cluster.
8. Generate random values of $\beta_{kl} \in \{1, -1\}$.
9. Apply fading σ_1 and σ_2 to channel coefficients within each cluster.
10. Apply overall shadowing term σ_x.
11. Convolve transmitted signal with channel impulse response and add white noise.
12. Input the signal to the Rake block and apply MRC.
13. Use ML detection to estimate the received symbol.
14. Convert the decoded data symbol into bits and calculate bit error rate.

To allow a fair comparison between schemes the value of $T_s + T_g$ is fixed at 16 ns or 32 ns for all schemes. This allows direct evaluation of performance gain with increasing guard time. In general, by keeping $T_s + T_g$ fixed, the 2-ary scheme will always have the longest duration of guard time and the higher M-ary schemes will have progressively shorter guard time durations.

For M-ary PPM IR-UWB, the symbol duration can be written as $(M \times T_p) + T_g$. This results in the transmitted data rate in bits per second being expressible as $k/((M \times T_p) + T_g)$. Similarly, the data rate for M-ary PPM-CAP IR-UWB is given by $(2 \times k)/((M \times T_p) + T_g)$, with example data rates given in Table 4.1. Maximum attainable data rates in bits per second for M-ary PPM-CAP IR-UWB in a CM-4 channel are shown in Table 4.2 where $T_s + T_g$ is equal to 80 ns.

$T_s + T_g$	2 PPM-CAP	4 PPM-CAP	8 PPM-CAP	16 PPM-CAP
16 ns	124 Mb/s	250 Mb/s	374 Mb/s	500 Mb/s
32 ns	64 Mb/s	124 Mb/s	188 Mb/s	250 Mb/s
48 ns	40 Mb/s	82 Mb/s	126 Mb/s	166 Mb/s

Table 4.1: M-ary PPM-CAP IR-UWB effective data rates in CM-1 channel.

The performance results of modulation format A, with T_g inserted between transmitted symbols, are first presented. These results are for both CM-1 and CM-4 channels. Brief results for modulation format B, with T_g embedded inside the pulse slot duration i.e. within the symbol, are presented following the results section of modulation format A. However, most of the attention is focused on modulation format A.

From comparison of Tables 4.1 and 4.2 it is seen that for the CM-4 channel, the maximum data rates achievable is 100 Mb/s when $T_s + T_g$ is equal to 80 ns. Since data rate is inversely proportional to T_g, transmission through a dense channel is possible provided one can make do with low data rates and significantly long guard time between symbols.

$T_s + T_g$	2 PPM-CAP	4 PPM-CAP	8 PPM-CAP	16 PPM-CAP
80 ns	25 Mb/s	50 Mb/s	75 Mb/s	100 Mb/s

Table 4.2: M-ary PPM-CAP IR-UWB effective data rates in CM-4 channel.

4.5.1 Modulation Format A

This section presents results for PPM and PPM-CAP IR-UWB based on modulation format A which is described in (4.9) to (4.19). This section evaluates the effect of various system parameters on system performance. The effect of pulse width T_p on system performance is presented first. BER plots showing the importance of adequate guard time T_g are then presented for M-ary PPM-CAP IR-UWB. This is followed by the results for M-ary PPM IR-UWB being compared with those for M-ary PPM-CAP IR-UWB.

Figures 4.4 to 4.7 show M-ary PPM-CAP BER plots for two different values of T_p. M is equal to 2, 4, 8 and 16 with $T_s + T_g$ fixed at 32 ns. T_p is taken as either 0.5 ns or 1 ns. Channel model CM-1 is used in obtaining these results. In addition, the plots show system performance for different numbers of Rake taps. Two conclusions evident from the plots are that increasing the number of Rake taps results in a marked improvement in system performance and this improvement can be further increased by using a narrower pulse width.

The narrow pulse shows better performance when the number of Rake taps is 15 or fewer. When using 30 taps, the difference in BER plots decreases due to the Rake being allowed to collect more useful multipath components. For example, from Figure 4.6, for the 8 PPM-CAP case, we see that for 5 Rake taps $T_p = 0.5$ ns achieves a lower error floor than $T_p = 1$ ns. When the number of Rake taps is increased to 15 and 30, we observe an improvement of 3 dB and 1 dB at a BER of 10^{-3}, respectively. For the rest of this thesis we assume T_p equal to 1 ns.

In Figures 4.8 to 4.11 we present BER performance plots for M-ary PPM-CAP IR-UWB that show the impact of varying T_g. To collect all the multipath energy a Rake requires an infinitely large number of Rake taps which is not possible in any practical implementation. Often we get satisfactory performance by using quite a limited number of Rake taps without substantially increasing the system complexity. Hence, we keep

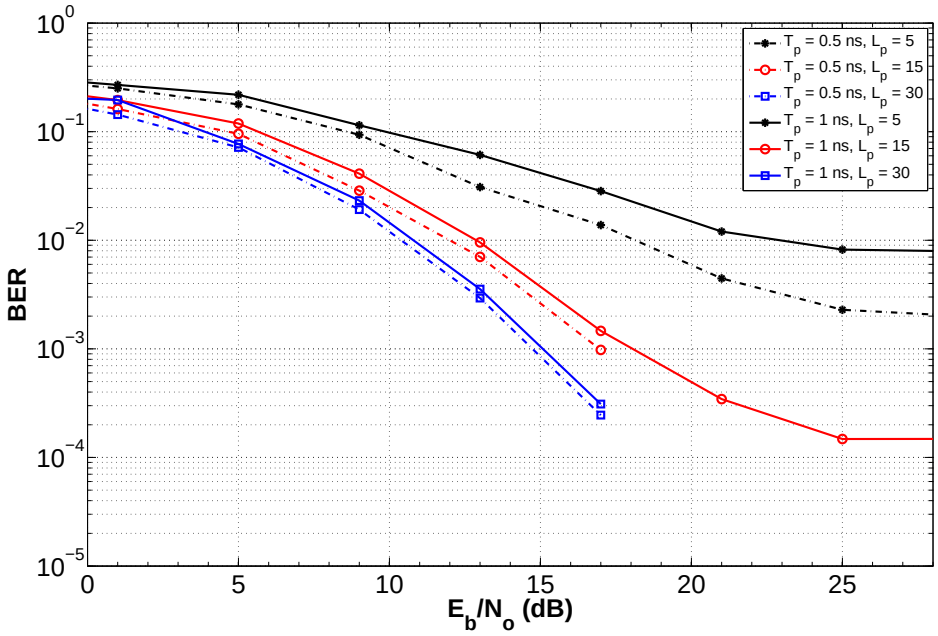

Figure 4.4: 2 PPM-CAP with T_p of 0.5 ns and 1 ns, $T_s + T_g$ of 32 ns, $L_p = 5$, 15 and 30 Rake taps and channel model CM-1.

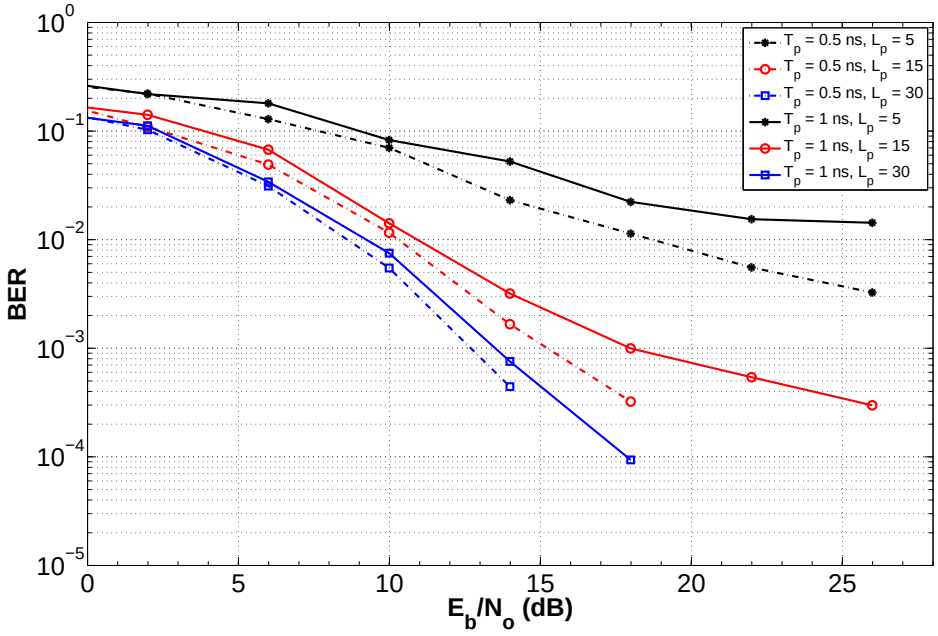

Figure 4.5: 4 PPM-CAP with T_p of 0.5 ns and 1 ns, $T_s + T_g$ of 32 ns, $L_p = 5$, 15 and 30 Rake taps and channel model CM-1.

the number of Rake taps fixed at 30 and $T_s + T_g$ fixed at 32 ns.

Figures 4.8 and 4.9 show the individual performance gain achieved by increasing T_g in 8 and 16 PPM-CAP IR-UWB schemes respectively. From Figure 4.8, i.e. the 8 PPM-CAP IR-UWB scheme, it is observed that the performance gain due to increasing T_g from 24 ns to 112 ns is not significant enough to warrant the increase. Instead, the effective data transmission rate decreases to 50 Mb/s from 188 Mb/s with a marginally improved error floor performance by increasing T_g to 112 ns. A similar trend can be observed in Figure 4.9 for 16 PPM-CAP IR-UWB scheme. It is observed that the performance with T_g equal to 32 ns is similar to that obtained by setting T_g equal to 16 ns. Considering the drop in data rate by increasing T_g from 16 ns to 32 ns without any significant gain in performance, the lower value of T_g is a better choice.

Figure 4.10 and Figure 4.11 show the M-ary PPM-CAP performance with $T_s + T_g$ of 16 ns and 32 ns respectively. It is observed that the BER plots tend to cluster as in any

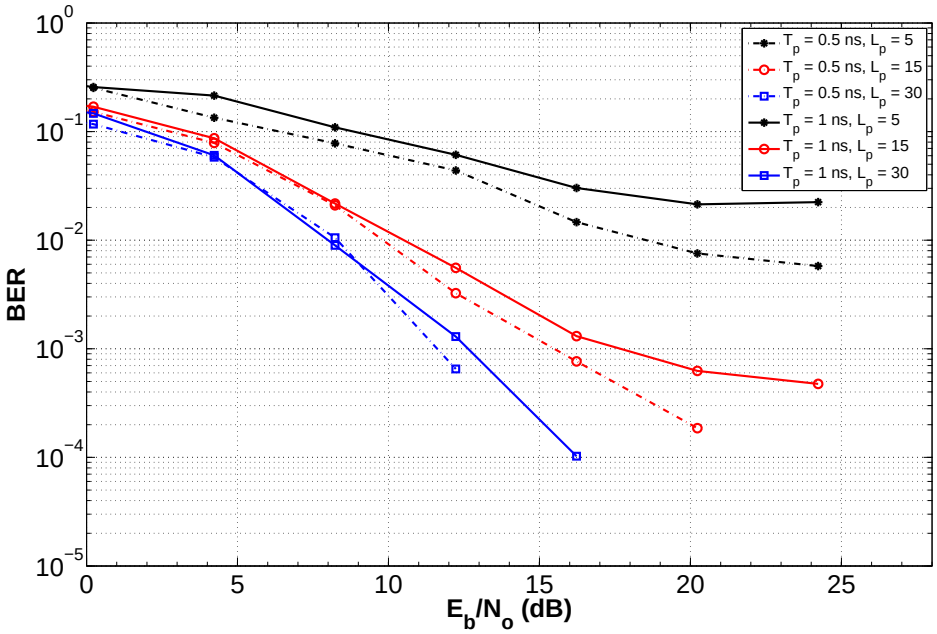

Figure 4.6: 8 PPM-CAP with T_p of 0.5 ns and 1 ns, $T_s + T_g$ of 32 ns, $L_p = 5$, 15 and 30 Rake taps and channel model CM-1.

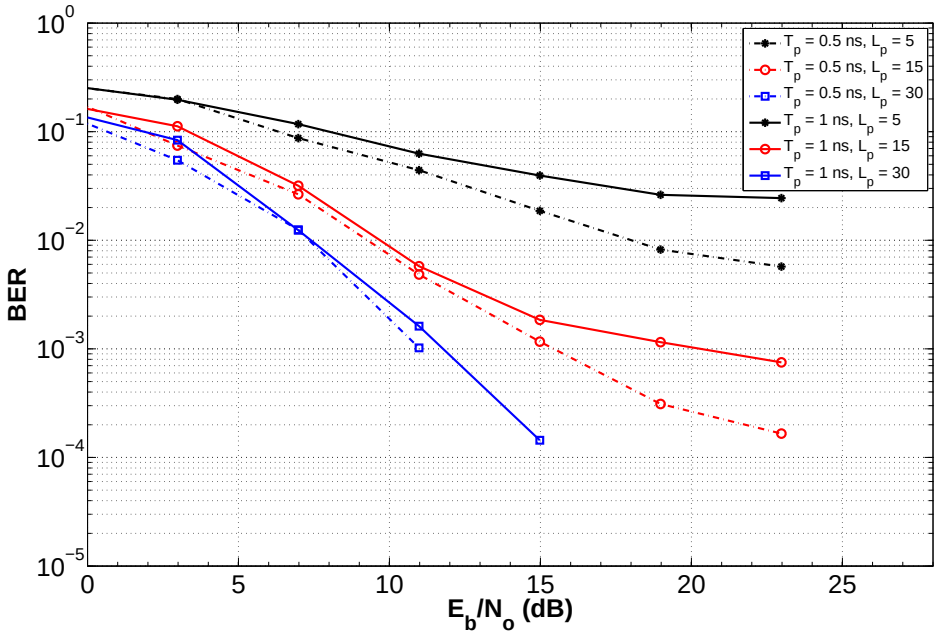

Figure 4.7: 16 PPM-CAP with T_p of 0.5 ns and 1 ns, $T_s + T_g$ of 32 ns, $L_p = 5$, 15 and 30 Rake taps and channel model CM-1.

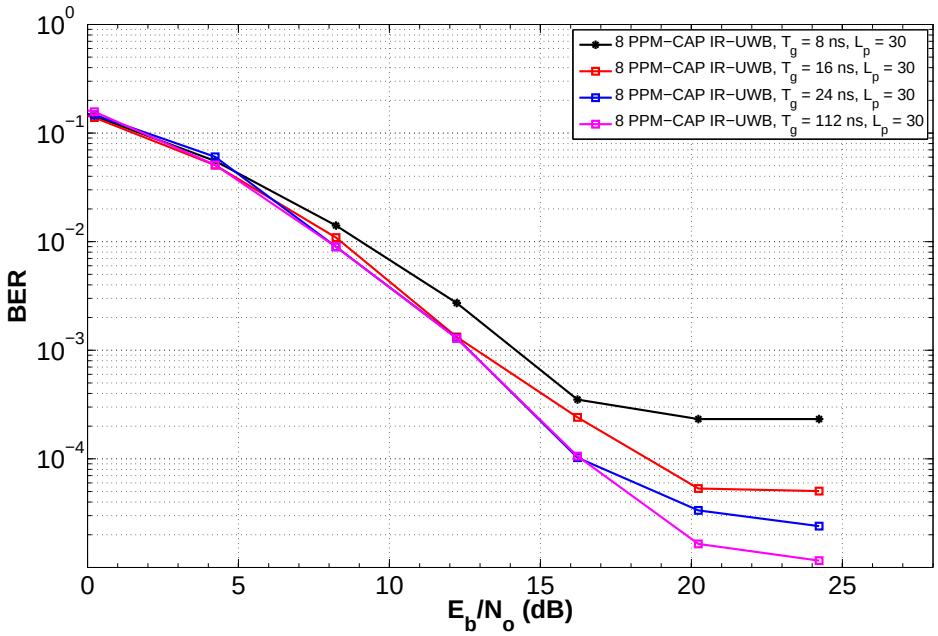

Figure 4.8: 8 PPM-CAP IR-UWB with $T_p = 1$ ns, different values of T_g, $L_p = 30$ Rake taps and channel model CM-1.

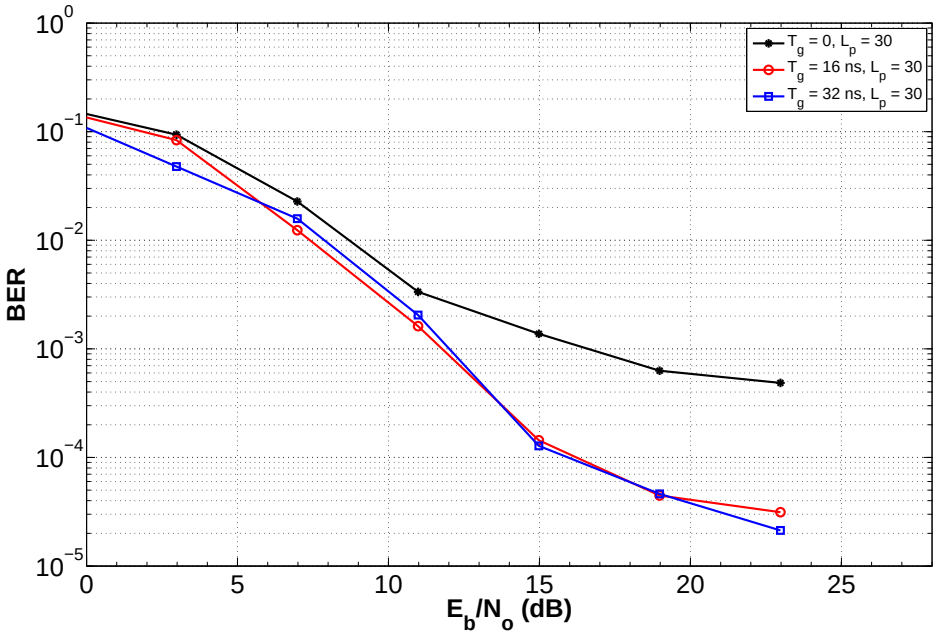

Figure 4.9: 16 PPM-CAP IR-UWB with $T_p = 1$ ns, different values of T_g, $L_p = 30$ Rake taps and channel model CM-1.

orthogonal modulation scheme. From Figure 4.10 it is observed that the larger M-ary scheme will error floor before any of the lower M-ary schemes due to having the least amount of T_g between symbols, provided the $T_s + T_g$ parameter is kept constant.

Lastly, we compare the BER performance of M-ary PPM IR-UWB with PPM-CAP IR-UWB. The results are presented for both CM-1 and CM-4 channel models. Figures 4.12 to 4.15 show the performance comparison for $T_s + T_g$ equal to 32 ns and CM-1 channel model. The number of Rake taps are 5, 15 and 30. From Figure 4.12 and Figure 4.15, i.e. the 2-ary and 16-ary schemes, it is observed for both PPM and PPM-CAP IR-UWB that lower error floor and high diversity gain can be achieved by increasing the number of L_p Rake taps corresponding to non-zero multipath channel components and the duration of T_g or effectively the $T_s + T_g$ parameter.

From Figure 4.12, looking at the 2 PPM-CAP IR-UWB plots, at a BER of 10^{-2} there is an improvement of 12 dB when L_p is increased from 5 to 30 Rake taps. A similar improvement can be observed from the PPM IR-UWB plots in Figure 4.12. A similar

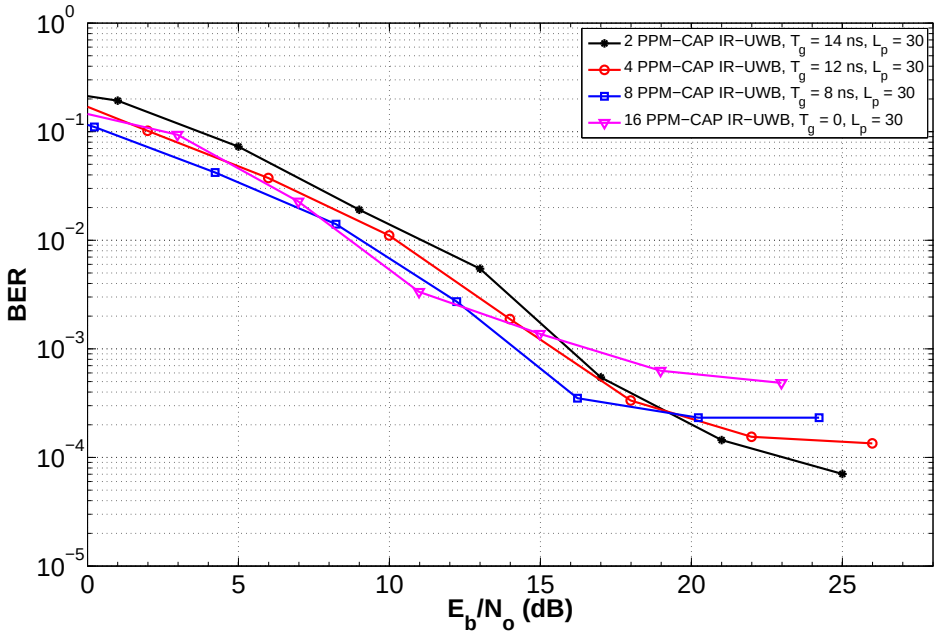

Figure 4.10: M-ary PPM-CAP IR-UWB with $T_p = 1$ns, $T_s + T_g$ of 16 ns, $L_p = 30$ Rake taps and channel model CM-1.

trend in performance gain is also seen for the 4, 8 and 16-ary schemes in Figures 4.13 to 4.15. From Figure 4.13 for 8 PPM-CAP IR-UWB, at a BER of 10^{-2}, the performance gain obtained from increasing L_p from 5 to 30 is approximately 12 dB. For 16 PPM-CAP IR-UWB, the performance gain at a BER of 10^{-2} is approximately 10 dB.

It is possible to increase performance further at the cost of increased hardware complexity by increasing L_p. In addition, it is observed that M-ary PPM IR-UWB shows slightly better performance than the equivalent M-ary PPM-CAP IR-UWB scheme, primarily due to timing offsets caused by the multipath channel leading to a loss of orthogonality between pulses. However, the data throughput achieved by PPM-CAP is double that achieved by PPM IR-UWB and the performance difference diminishes with an increasing number of Rake taps L_p and guard time T_g.

Figure 4.16 shows the M-ary PPM-CAP IR-UWB performance in CM-4 channel model for L_p equal to 30 taps, with $T_s + T_g$ equal to 32 ns. From the figure it is observed that all of the M-ary PPM-CAP IR-UWB schemes error floor out well above 10^{-3}

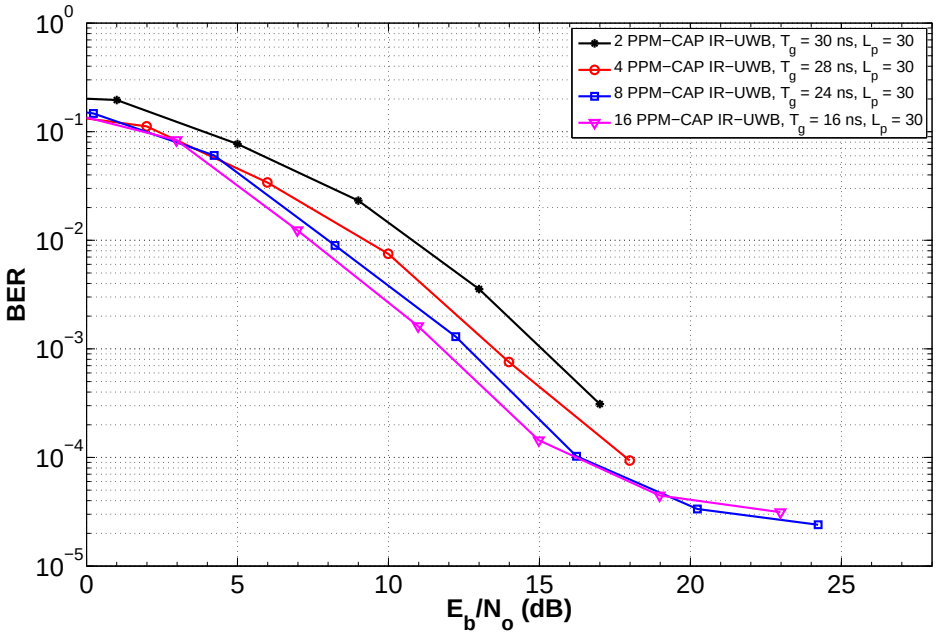

Figure 4.11: M-ary PPM-CAP IR-UWB with $T_p = 1$ns, $T_s + T_g = 32$ ns, $L_p = 30$ Rake taps and channel model CM-1.

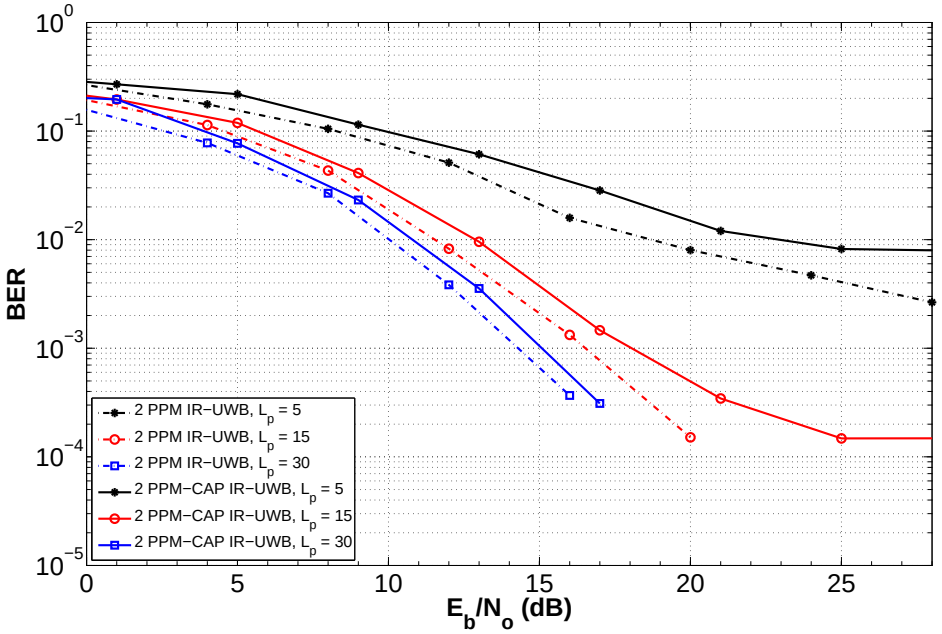

Figure 4.12: 2 PPM and 2 PPM-CAP IR-UWB with $T_p = 1$ ns, $T_s + T_g = 32$ ns, $L_p = 5$, 15 and 30 Rake taps and channel model CM-1.

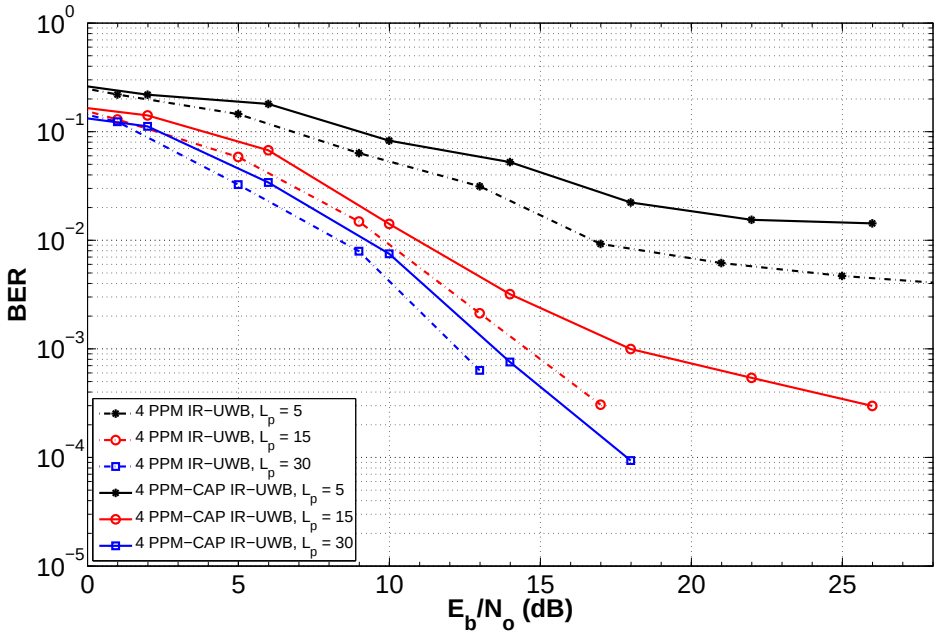

Figure 4.13: 4 PPM and 4 PPM-CAP IR-UWB with $T_p = 1$ ns, $T_s + T_g = 32$ ns, $L_p = 5$, 15 and 30 Rake taps and channel model CM-1.

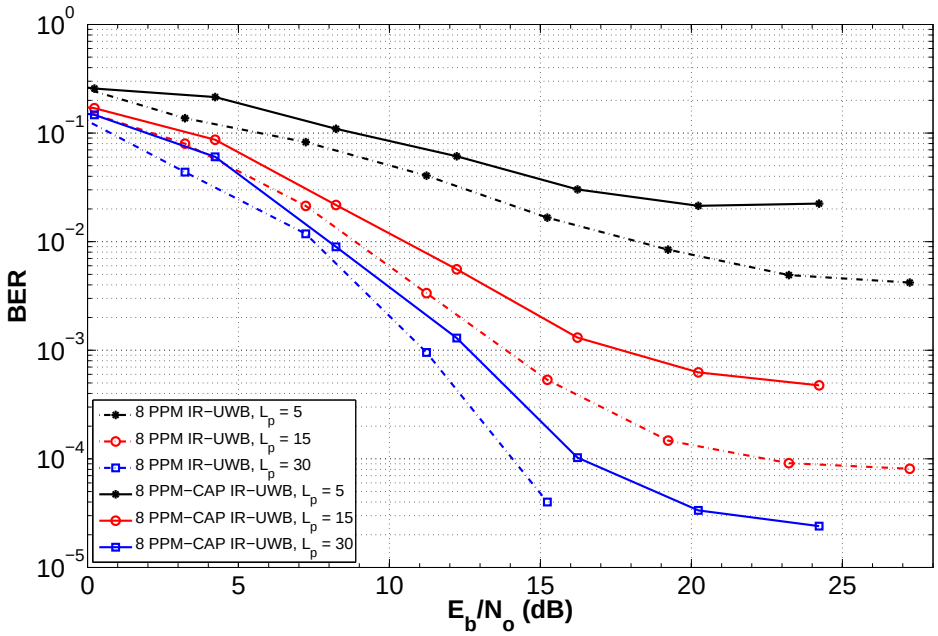

Figure 4.14: 8 PPM and 8 PPM-CAP IR-UWB with $T_p = 1$ ns, $T_s + T_g = 32$ ns, $L_p = 5$, 15 and 30 Rake taps and channel model CM-1.

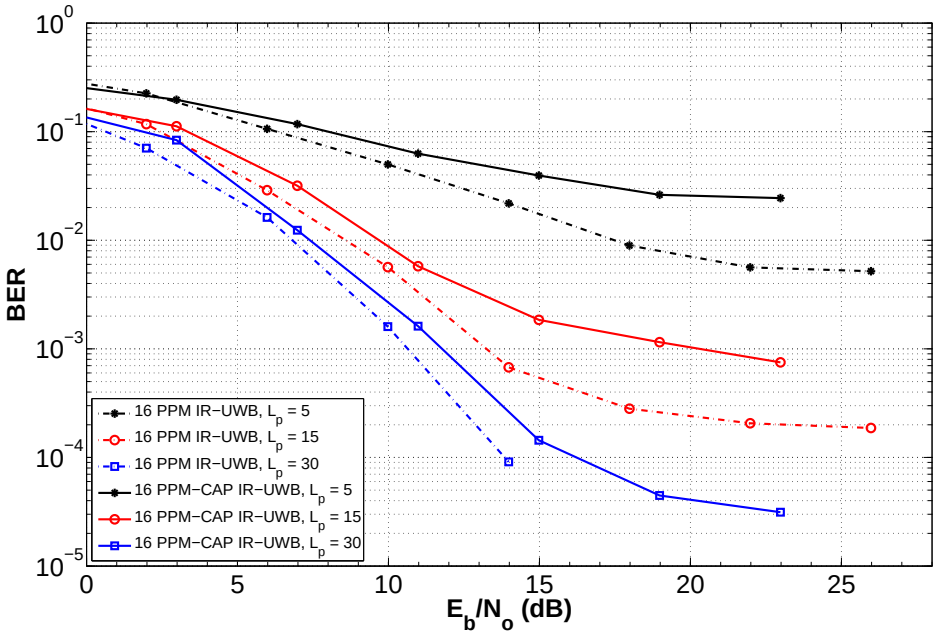

Figure 4.15: 16 PPM and 16 PPM-CAP IR-UWB with $T_p = 1$ ns, $T_s + T_g = 32$ ns, $L_p = 5$, 15 and 30 Rake taps and channel model CM-1.

hence rendering the choice of $T_s + T_g$ equal to 32 ns unusable. The rest of the CM-4 channel model results are based on $T_s + T_g$ equal to 80 ns. Figures 4.17 to 4.20 show the performance comparison for $T_s + T_g$ equal to 80 ns in channel model CM-4. The number of Rake taps are 5, 15 and 30. A similar trend is observed in the plots i.e. there is a performance gain for both M-ary PPM and M-ary PPM-CAP IR-UWB schemes with increasing L_p and T_g.

Comparing Figure 4.20 and Figure 4.15, for the 16 PPM-CAP IR-UWB scheme at $L_p = 30$ for CM-4 and CM-1 channel models, respectively, it is observed that the CM-4 channel requires a significantly larger $T_s + T_g$ of 80 ns to achieve a BER 10^{-3} and shows a loss of approximately 11 dB when compared its respective CM-1 channel model case. Unlike transmission in the CM-1 channel, it is observed from Figures 4.17 to 4.20 that any M-ary PPM-CAP IR-UWB scheme will require an L_p of 30 or more Rake taps coupled with a $T_s + T_g$ of 80 ns or more for suitable signal transmission.

Comparing 2, 4, 8 and 16 PPM-CAP IR-UWB for channel models CM-1 (Figures 4.13

to 4.15) and CM-4 (Figures 4.18 to 4.20), the performance loss caused by the CM-4 channel model at a BER of 10^{-3} and an L_p of 30 Rake taps is observed to be in the range of approximately 7 dB (for 2 PPM-CAP IR-UWB) to 11 dB (for 16 PPM-CAP IR-UWB), respectively.

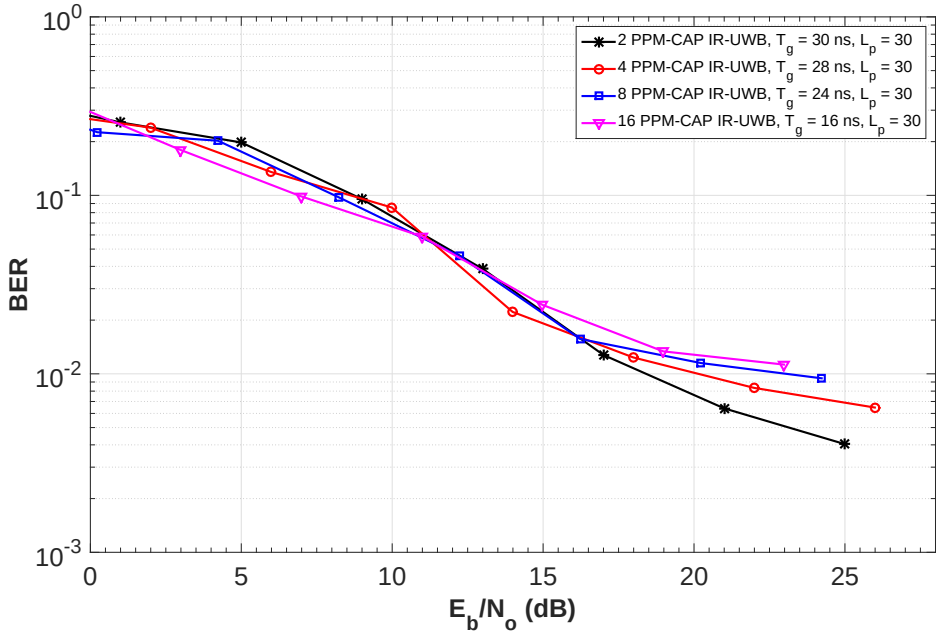

Figure 4.16: M-ary PPM-CAP IR-UWB with $T_p = 1$ ns, $T_s + T_g = 32$ ns, Rake taps are 5, 15 and 30 and channel model CM-4.

4.5.2 Modulation Format B

This section shows the BER plots for an M-ary PPM-CAP IR-UWB scheme using modulation format B, as described in (4.20) to (4.24). This format provides an alternative method to provide time spacing between symbols by integrating the guard time inside the pulse slots.

Figures 4.21 to 4.23 present results for a symbol time (inclusive of guard time) of 32 ns , channel model CM-1 is used and T_p is 1 ns. The number of Rake taps used are 5, 15 and 30. Figures 4.22 and 4.23 present acceptable performance via this scheme, which is comparable to modulation format A.

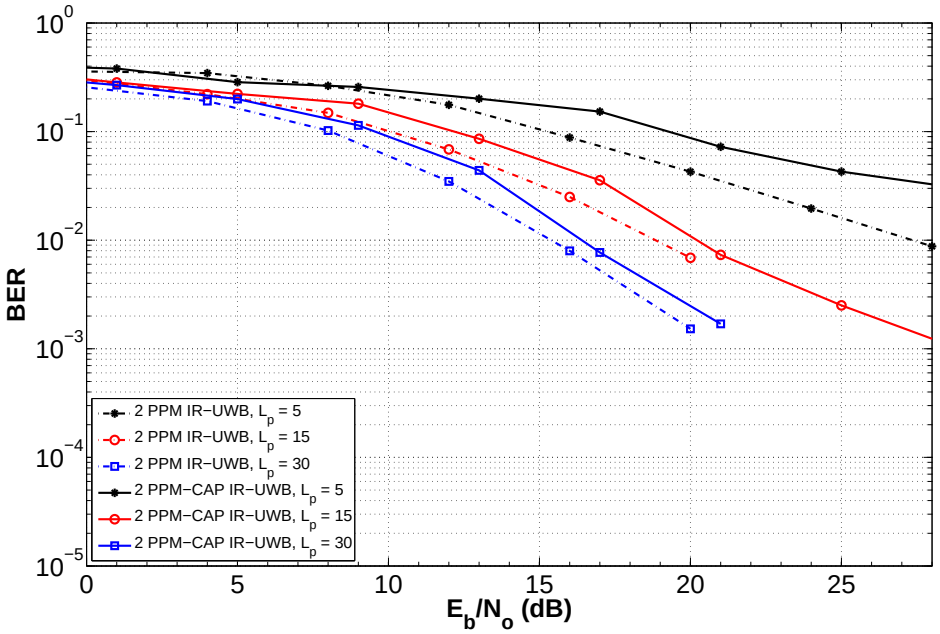

Figure 4.17: 2 PPM and 2 PPM-CAP IR-UWB with $T_p = 1$ ns, $T_s + T_g = 80$ ns, Rake taps are 5, 15 and 30 and channel model CM-4.

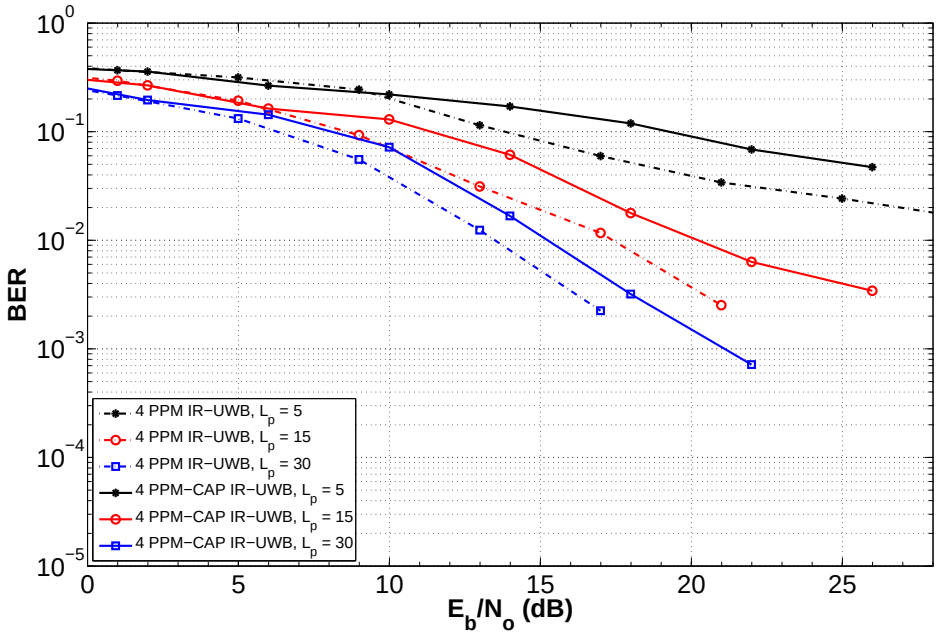

Figure 4.18: 4 PPM and 4 PPM-CAP IR-UWB with $T_p = 1$ ns, $T_s + T_g = 80$ ns, $L_p =$ 5, 15 and 30 Rake taps and channel model CM-4.

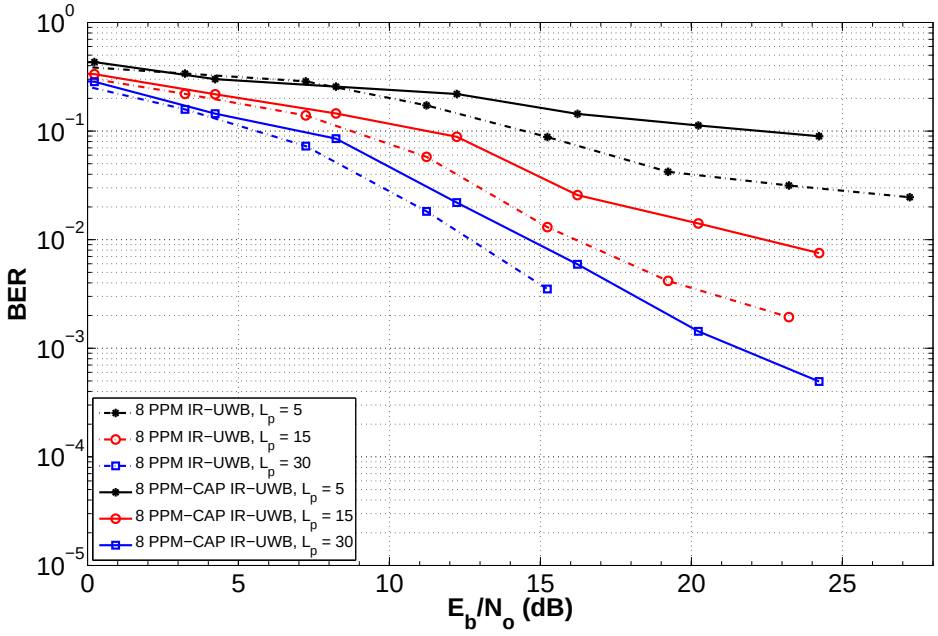

Figure 4.19: 8 PPM and 8 PPM-CAP IR-UWB with $T_p = 1$ ns, $T_s + T_g = 80$ ns, $L_p =$ 5, 15 and 30 Rake taps and channel model CM-4.

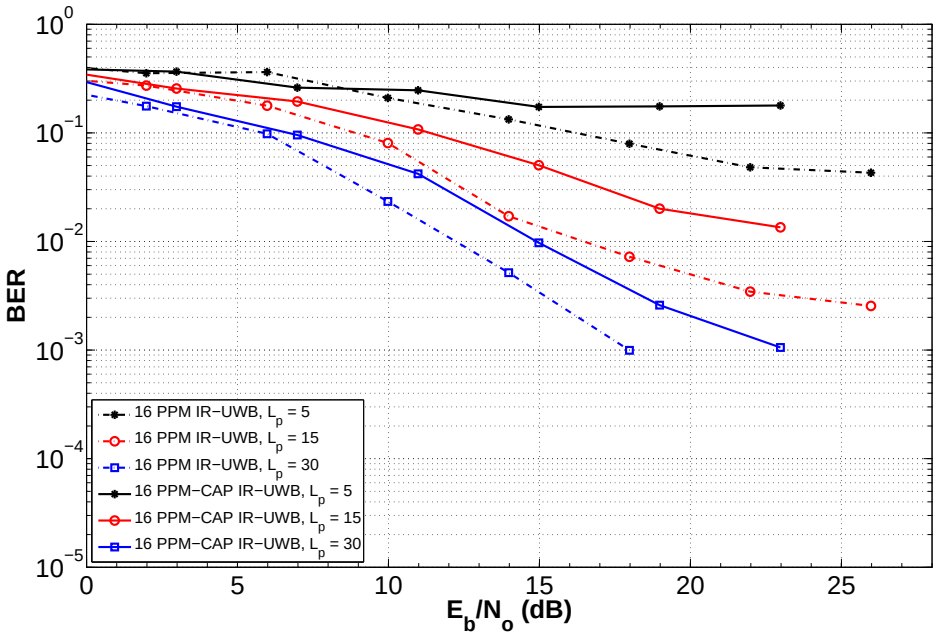

Figure 4.20: 16 PPM and 16 PPM-CAP IR-UWB with $T_p = 1$ ns, $T_s + T_g = 80$ ns, $L_p = 30$ Rake taps and channel model CM-4.

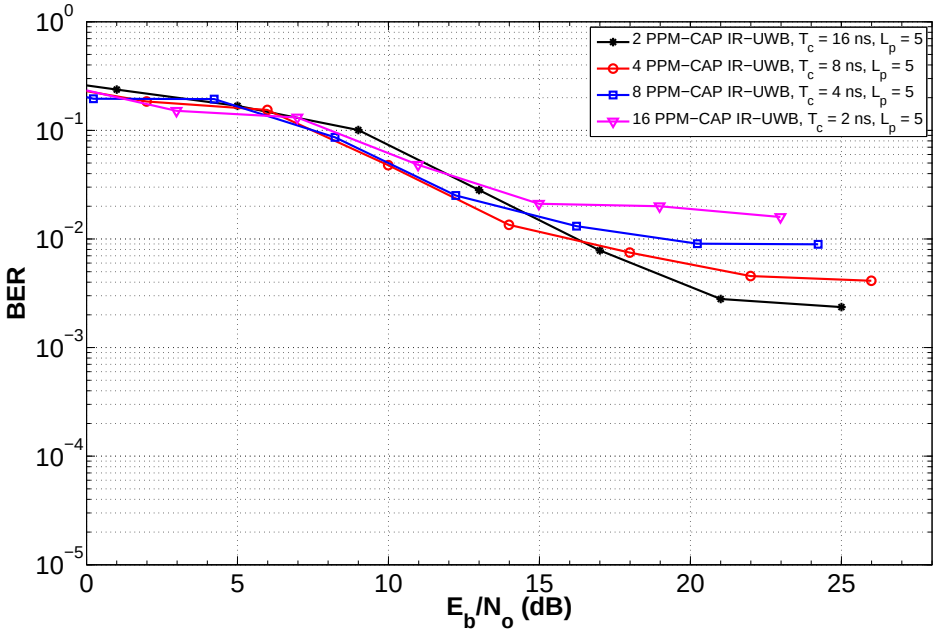

Figure 4.21: M-ary PPM-CAP with $T_p = 1$ ns, $T_s + T_g = 32$ ns, $L_p = 5$ Rake taps and channel model CM-1.

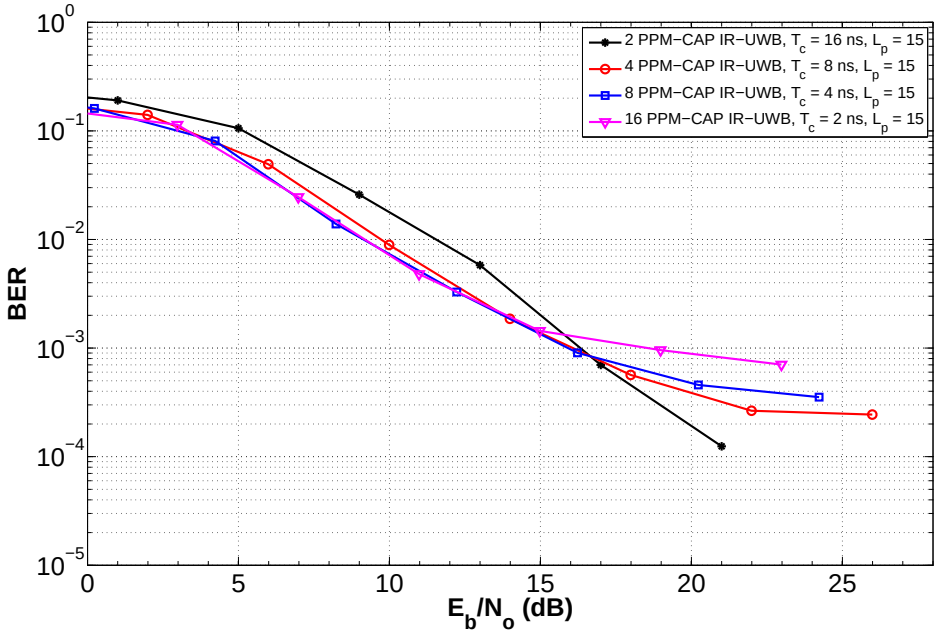

Figure 4.22: M-ary PPM-CAP with $T_p = 1$ ns, $T_s + T_g = 32$ ns, $L_p = 15$ Rake taps and channel model CM-1.

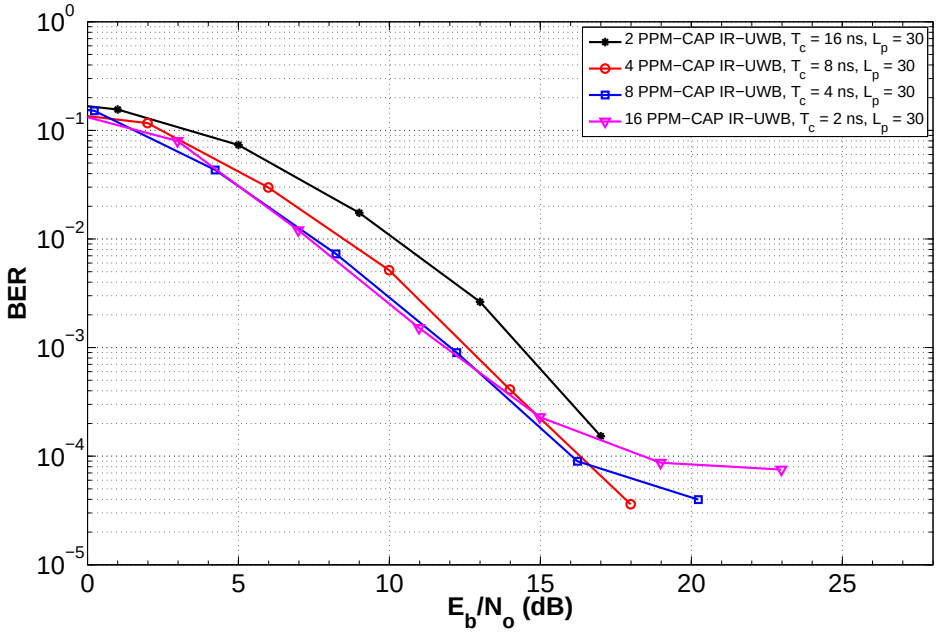

Figure 4.23: M-ary PPM-CAP with $T_p = 1$ ns, $T_s + T_g = 32$ ns, $L_p = 30$ Rake taps and channel model CM-1.

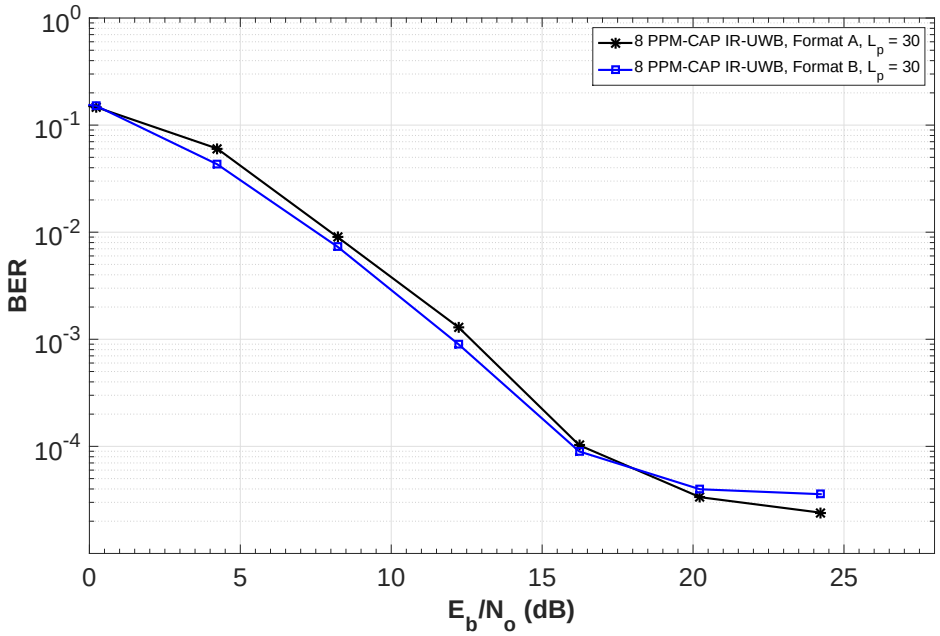

Figure 4.24: 8-ary PPM-CAP comparison between modulation format A and B, $T_p = 1$ ns, effective symbol time is 32 ns, $L_p = 30$ Rake taps and channel model CM-1.

4.5.3 Performance Comparison Between Format A and B

In this section we compare the BER performance obtained using the modulation formats A and B, as described in sections 4.3 and 4.4 respectively. For a fair comparison T_p is equal to 1 ns, the symbol time inclusive of guard time is equal to 32 ns for both schemes, L_p is equal to 30 Rake taps and the channel model is CM-1.

Figures 4.24 to 4.27 show the performance comparison of M-ary PPM-CAP IR-UWB using modulation formats A and B. From Figures 4.24 and 4.25 it is observed that modulation format A provides a slightly lower error floor for the high order modulation schemes, i.e. when M is equal to 8 and 16 compared to that attained by format B. In addition, it is observed that the performance loss in format A for $M = 8$ and 16 at a BER of 10^{-3} is approximately 0.5 dB and zero respectively. This shows that format A is preferable over format B provided the modulation order M is kept sufficiently high i.e. $M \geq 8$.

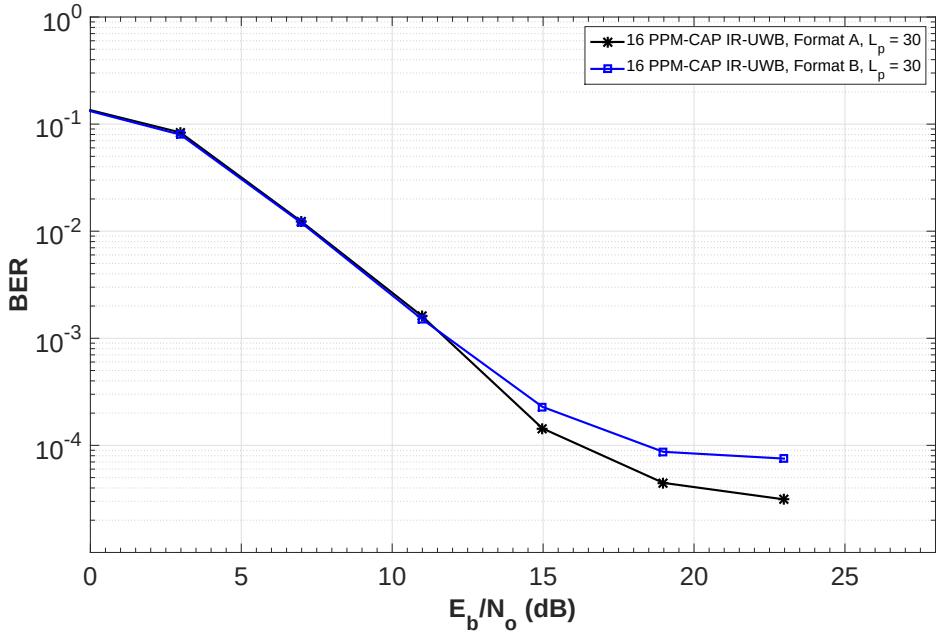

Figure 4.25: 16-ary PPM-CAP comparison between modulation format A and B, T_p = 1 ns, effective symbol time is 32 ns, $L_p = 30$ Rake taps and channel model CM-1.

Comparing both formats in Figures 4.26 and 4.27, for M equal to 2 and 4, it can be observed that format A shows slight performance loss over format B. From Figure 4.26 at a BER of 10^{-3} it is seen that format A shows a loss of just under 1 dB compared to format B. A similar trend can be observed from Figure 4.26 at a BER of 10^{-3}, i.e the performance loss suffered by format A over format B is approximately 1 dB. Since the UWB channel [21], [25], [134] has more high energy multipath components in the first quarter of its channel impulse response, by using format B shown in Figure 4.3, with M equal to 2 or 4 results in a longer minimal ISI region right after the pulse position rather than at the end of the symbol. In addition to minimizing ISI, this helps in attenuation of cross-correlation interference between inphase and its Hilbert pulse.

It can be concluded that format B is slightly advantageous for low values of M, while format A is an effective and robust scheme that provides consistent results and easier manipulation of the length of guard time which is completely separate from the M-ary symbol format.

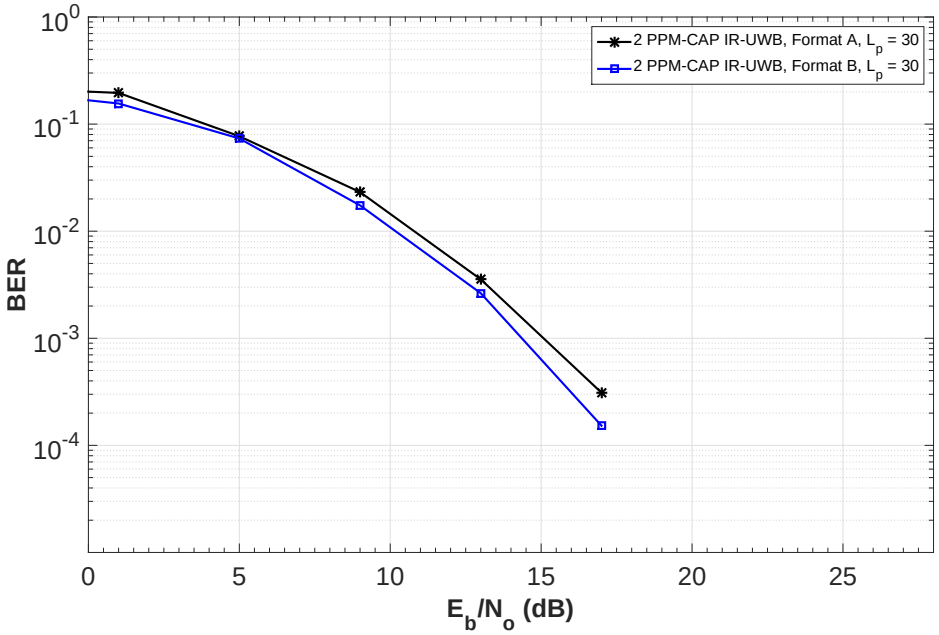

Figure 4.26: 2-ary PPM-CAP comparison between modulation format A and B, $T_p = 1$ ns, effective symbol time is 32 ns, $L_p = 30$ Rake taps and channel model CM-1.

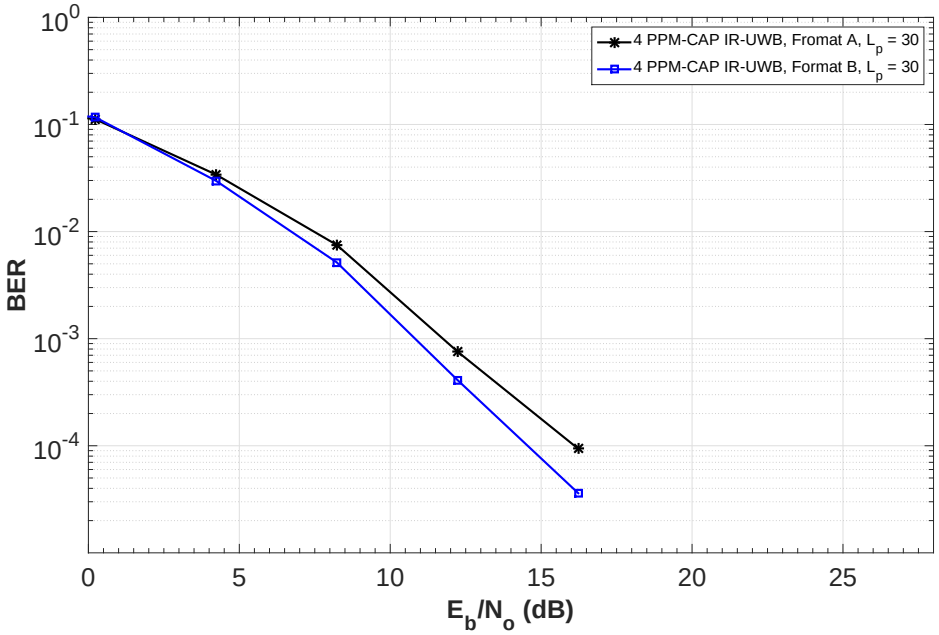

Figure 4.27: 4-ary PPM-CAP comparison between modulation format A and B, $T_p = 1$ ns, effective symbol time is 32 ns, $L_p = 30$ Rake taps and channel model CM-1.

4.6 CONCLUSIONS

This chapter describes the system models for M-ary PPM IR-UWB and M-ary PPM-CAP IR-UWB based on the IEEE 802.15.3a multipath channel model. It presents the methodology for data detection based on ML detection using a Rake Receiver. The two transmission formats are compared using different sets of system parameters. The performance results show the importance of guard times and multiple Rake taps. It is observed that better performance and lower error floors can be obtained by increasing both guard time between symbols and the number of Rake taps. Increasing the modulation order M results in better throughput and higher data rates for a fixed set of system parameters. However, in a CM-1 channel increasing the guard time beyond approximately 30 ns does not significantly increase the system performance, instead it decreases system throughput. Provided we keep $T_s + T_g$ constant for all M schemes, a clustering of the plots with increasing M is observed. In addition, the higher M-ary plots tend to exhibit an error floor earlier than the lower M-ary plots. Much of the published literature on IR-UWB considers bi-orthogonal IR-UWB systems, TH IR-UWB and frequency domain based UWB as reviewed in Chapter 2. In addition, different excess delays of the channel model are considered along with different channel model environments and parameters. An exact comparison of these schemes with the proposed carrierless amplitude modulated PPM-CAP IR-UWB scheme is not appropriate due to differences in system parameters used.

To date we have assumed perfect synchronization in all the transmission schemes. In Chapter 5, a simple synchronization scheme for M-ary PPM-CAP IR-UWB is presented. In addition, we present a system performance comparison of M-ary PPM-CAP IR-UWB with perfect synchronization and timing estimation via the proposed scheme.

Chapter 5

SYNCHRONIZATION IN M-ARY PPM-CAP IR-UWB

5.1 INTRODUCTION

Previous chapters developed and evaluated M-ary PPM-CAP IR-UWB under the assumption of perfect synchronization. They presented results for varying system parameters and channel conditions for M-ary PPM-CAP IR-UWB. In this chapter, PPM-CAP system performance is evaluated assuming that synchronization information is to be extracted from the received signal prior to data demodulation. This can be achieved either from the data bearing signal or from some form of pilot or training signal.

Synchronization is a critical aspect of system design in both wired [135–143] and wireless communication [144–150]. It can be achieved by means of either feed-forward data aided (DA), non-data aided (NDA) [148,149,151] techniques or by using phase lock loops [150]. DA techniques require synchronization pilot codes to be sent at the start of every data frame. Synchronization is then achieved when a local copy of the code at the receiver is perfectly matched in delay to the received version of the synchronization pilot code.

The narrow pulses in IR-UWB communication coupled with a high pulse repetition rate and propagation through a multipath channel with long delay spread makes getting an accurate synchronization lock extremely important and at the same time difficult. The techniques used for synchronization depend on a variety of factors such as the modulation format, channel characteristics and the system type itself e.g. coded or uncoded, single input and output (SISO), or multiple input and output (MIMO) etc.

Because of the slotted and framed nature of PPM schemes, synchronization can be obtained by achieving an accurate estimate of the start time of a data frame. Since in PPM IR-UWB, each symbol consists of a pulse within one of $M = 2^k$ slots, with k being the number of bits per symbol, each symbol within a particular M-ary scheme has equal time duration and by making the length of the frame fixed can make the process of demodulation of individual symbols a simple task after frame start time has been established.

This chapter presents a feed-forward DA frame start time estimator based on ML estimation. The effects of different numbers of synchronization pilot symbols is studied and system performance including timing estimation is evaluated through simulation. Once frame lock is achieved, the symbols within a frame remain synchronized and symbol synchronization may be maintained via a counter which releases the synchronized frame after the count is completed. This technique requires that knowledge of the number of symbols per frame be available at the receiver.

5.2 SYNCHRONIZATION IN PPM-CAP

Figure 5.1 shows the feed forward DA Rake receiver block diagram. The received signal consisting of the pilot codes for synchronization along with the data frame are received. The pilot symbols are initially processed by the frame start time estimation block to estimate the frame start time. Control is then passed to the data demodulation and detection block which maintains lock by counting at the symbol rate up to the number of symbols per frame.

This section presents ML frame timing estimation for PPM-CAP using pilot symbols and a feed-forward Rake matched to the transmitted synchronization pulse shape $x^d(t)$. Frame synchronization is carried out via ML estimation of the pulse slot location from within the synchronization pilot symbols. We denote the number of pilot symbols which are added to the data frame for timing estimation as N_d, where $N_d = [1, 3, 5, ...]$. Timing

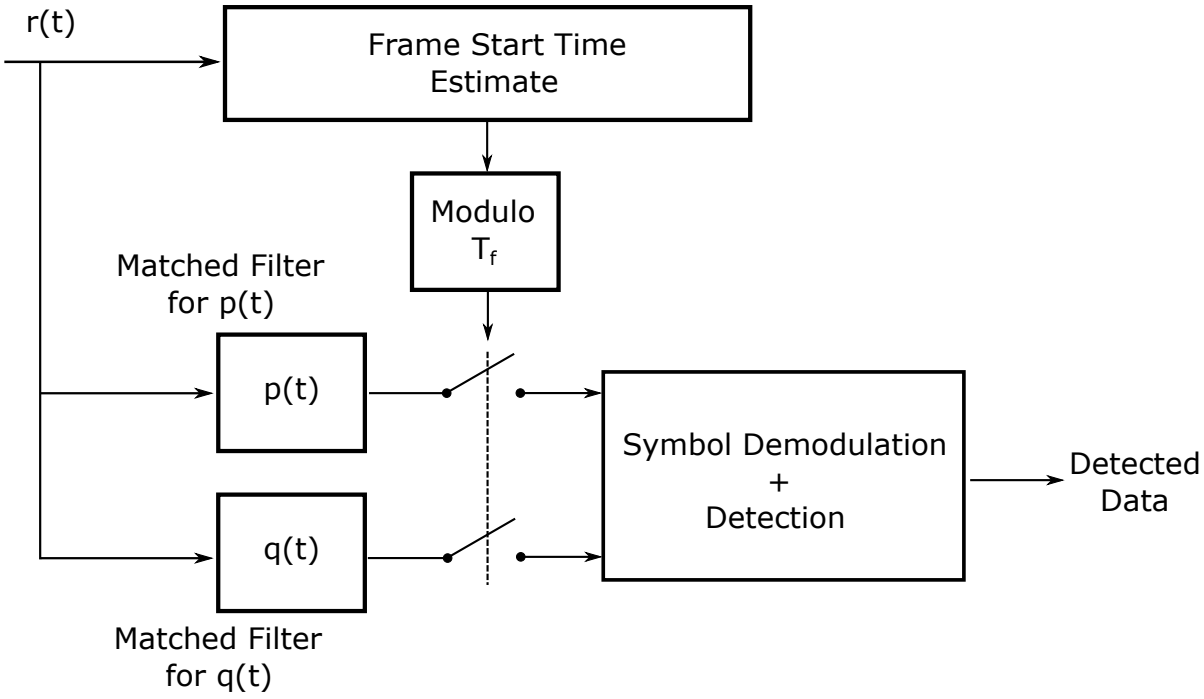

Figure 5.1: PPM-CAP IR-UWB receiver with feed forward open loop synchronization.

estimation is carried out by the quadrature pulse matched portion of the Rake, thus $x^d(t) = q(t)$. The transmitted signal with synchronization pilot symbols can be written as

$$\begin{aligned} s(t) = & \sum_{n_d=0}^{N_d-1} (\sqrt{E_s}) x^d(t - n_d(T_s^d + T_g^d) - a_{n_d} T_p^d) \\ & + \sum_{n=0}^{\infty} [(\sqrt{E_s/2}) p(t - (n + N_d)(T_s + T_g) - a_n T_p) \\ & + (\sqrt{E_s/2}) q(t - (n + N_d)(T_s + T_g) - b_n T_p)], \end{aligned} \tag{5.1}$$

where $(n + N_d)(T_s + T_g) \leq t \leq (n + N_d + 1)(T_s + T_g) \forall\, n,\ a_n, b_n \in \{0, 1, ..., M - 1\}$ and $a_n T_p$, $b_n T_p$ specify the pulse positions within the n^{th} symbol. E_s represents the pulse energy of the synchronization pulse. a_{n_d} represents the pulse slot position of the quadrature pulse and is fixed to $a_{n_d} = 0$, i.e. first pulse slot in a synchronization symbol

having $M-1$ slots for $n_d = \{1, 2, ..., N_d\}$. T_g^d represents the guard time in the pilot symbol. We can compactly express (5.1) as

$$s_n(t) = s_d(t) + s_n^a(t) + s_n^b(t), \tag{5.2}$$

where $s_d(t)$ represents the synchronization pilot frame. $s_n^a(t)$ and $s_n^b(t)$ represent the PPM-CAP in-phase and orthogonal symbols, respectively. From Chaper 2, the IEEE 802.15.3a channel model [26] [131] is represented as

$$h(t) = X \sum_{l=0}^{L_c} \sum_{k=0}^{L_r} \alpha_{kl}\, \delta(t - T_l - \tau_{kl}), \tag{5.3}$$

where L_c and L_r represent the number of clusters and rays, respectively. The α_{kl} are statistically independent random variables following an exponential distribution and denote the path gain of the k^{th} ray within the l^{th} cluster. T_l is the arrival time of the l^{th} cluster. τ_{kl} is the delay associated with the k^{th} ray in the l^{th} cluster. The received multipath signal is $r(t) = s(t) \otimes h(t)$ which after substituting equations (5.2) and (5.3) can be expressed as

$$\begin{aligned} r(t) = (\sqrt{E_s}) & \sum_{n_d=0}^{N_d-1} \sum_{l=0}^{L_c} \sum_{k=0}^{L_r} \alpha_{kl}\, x^d(t - n_d(T_s^d + T_g^d) - a_d T_p^d - T_l - \tau_{kl}) \\ & + (\sqrt{E_s/2}) \sum_{n=0}^{\infty} \sum_{l=0}^{L_c} \sum_{k=0}^{L_r} \alpha_{kl}\, p(t - (n + N_d)(T_s + T_g) - a_n T_p - T_l - \tau_{kl}) \\ & + (\sqrt{E_s/2}) \sum_{n=0}^{\infty} \sum_{l=0}^{L_c} \sum_{k=0}^{L_r} \alpha_{kl}\, q(t - (n + N_d)(T_s + T_g) - b_n T_p - T_l - \tau_{kl}) \\ & + w(t). \end{aligned} \tag{5.4}$$

The first part of (5.4) is used to estimate the frame start time via DA ML timing estimation. Here, the pilot symbol contains a single pulse having energy E_s. The data symbol has two pulses with each having half the energy of the pilot pulse. This makes

the total symbol energy of the data and pilot symbol to be equal.

5.2.1 Frame Start Time Estimation

Let $\boldsymbol{\eta} = [a_0, a_1, ..., a_{N_d-1}]$ be the true pulse slot locations of N_d pilot pulses within N_d synchronization pilot symbols. We denote $\hat{\boldsymbol{\eta}}$ as the pulse slot estimate deduced from the synchronization pilot symbols. The total number of pulse slots through which the receiver Rake searches can be expressed as $\eta_{total} = (N_d \times (T_s^d + T_g^d))/T_p$.

Due to the nature of the UWB channel, long delay spreads are common. This results in significant ISI unless a large guard time is used to mitigate the ISI. In order to increase energy capture a Rake matched to the synchronization pilot pulse shape is used. In this paper the Hilbert transform of the Scholtz monocycle is used as the pulse template for the Rake. Let $\mathbf{w}_{rake}^d$ be the rake weights used during timing estimation where for simplicity $\mathbf{w}_{rake}^d = \mathbf{w}_{rake}$. The pulse slot weight within each synchronization pilot symbol can be obtained from

$$y_i^{n_d} = \sum_{l_{rake}^d=0}^{L_p^d-1} w_{rake}^d \qquad \left(\int_{iT_p+\tau_{l_{rake}^d}}^{iT_p+T_p+\tau_{l_{rake}^d}} s_d(t) q(t - iT_p - \tau_{l_{rake}^d}) dt \right), \tag{5.5}$$

where $y_i^{n_d}$ denotes the weight of the i^{th} pulse slot in the n_d^{th} synchronization pilot symbol after matched filtering and multipath energy collection by the Rake. The output of the Rake can be denoted by $\mathbf{Y^{n_d}}$ and may be expressed as

$$\mathbf{Y^{n_d}} = [y_0^{n_d}, y_1^{n_d}, ..., y_{I_{total}-1}^{n_d}], \tag{5.6}$$

where I_{total} represents the total number of pulse slots in the n_d synchronization pilot symbol. The ML estimated pulse slots corresponding to each of the N_d synchronization

pilot symbols, i.e. the complete synchronization frame, can now be expressed as

$$\hat{\boldsymbol{\eta}} = arg \max_{\sum_{n_d=0}^{Nd-1} i} \mathbf{Y^{n_d}}, \tag{5.7}$$

where each $\hat{\eta_i} \in [0, (I_{total}) - 1]$. Majority logic decision is now applied to determine the data frame start time $\hat{\tau}_f$ from the ML estimates in (5.7). Correct data frame time estimation is determined only if any $\hat{\eta_i} = \eta_i \, \forall \, i \geq (N_d + 1)/2$. Once the correct start time is estimated, data symbol demodulation can be carried out by the Rake matched to the in-phase and quadrature pulses as described in Chapter 4. The Rake output with respect to m can be written for the m^{th} data pulse slot as

$$y_m^{a'} = \sum_{l_{rake}=0}^{L_p-1} w_{l_{rake}} \quad \left(\int_{mT_p+\tau_{l_{rake}}}^{mT_p+T_p+\tau_{l_{rake}}} r(t) x_{ref}^{p(t)}(t - mT_p - \tau_{l_{rake}}) dt \right), \tag{5.8}$$

$$y_m^{b'} = \sum_{l_{rake}=0}^{L_p-1} w_{l_{rake}} \quad \left(\int_{mT_p+\tau_{l_{rake}}}^{mT_p+T_p+\tau_{l_{rake}}} r(t) x_{ref}^{q(t)}(t - mT_p - \tau_{l_{rake}}) dt \right). \tag{5.9}$$

The MRC outputs along with the ML detected inphase and quadrature data estimates are obtained by (4.16) to (4.19). The normalized mean square error can be obtained from $\hat{\boldsymbol{\eta}}$ as

$$NMSE = E \left\{ \sum_{i=0}^{N_d-1} \left[\frac{\eta_i - \hat{\eta_i}}{I_{total}} \right]^2 \right\}. \tag{5.10}$$

Since the PPM-CAP data frame format has symbols preceding the synchronization pilot frame, hence the frame start time $\hat{\tau}_f$ corresponds to the start time of the first symbol $\hat{\tau}_s$ in the data frame i.e. $\hat{\tau}_f = \hat{\tau}_s$. After the first symbol's start time is established, symbol synchronization within the frame is maintained by a symbol rate counter that counts to the number of symbols in the data frame.

5.3 SIMULATION RESULTS

Simulated evaluation of the bit error rate (BER) as a function of E_b/N_0 and normalized mean square error (NMSE) as a function of E_p/N_0 are presented for an 8 PPM-CAP system. For the 4 and 16 PPM-CAP IR-UWB schemes BER plots are presented which show similar trends as that of the 8 PPM-CAP scheme. E_b represents the energy per data bit. E_p represents the transmitted pulse energy. The channel environment assumed is the IEEE multipath channel CM-1 [25]. The multipath channel is assumed to be time invariant for the duration of a transmitted frame i.e. quasi-static for T_f time duration. There are 200 symbols per data frame. T_p is 1 ns for all schemes. A Rake with $L_p = 30$ taps is used. $T_g + T_s$ is fixed at 32 ns. N_d synchronization pilot symbols are inserted before the data frame. Figure 5.2 shows the BER plots for the case of N_d equal to 1, 3 and 7 synchronization pilot symbols for determining frame start time. Following majority logic detection we consider the frame start time to be accurate if 1, 2 or 4 synchronization pilot symbols have $\hat{\eta}_i = \eta_i$, respectively. We observe from Figure 5.2 that the maximum SNR degradation between a perfectly synchronized system and one that has been synchronized via timing estimation is approximately 5 dB for $N_d = 1$. The degradation in BER diminishes by increasing the number of synchronization pilot symbols at the start of each data frame. For $N_d = 3$ and $N_d = 7$ we observe an improvement in BER. In addition, it is observed that the performance increase achieved by increasing N_d tends to reduce hence making the overhead of a number of large synchronization pilot symbols unnecessary.

Figure 5.3 shows the normalized mean square error of the 8 PPM-CAP scheme with N_d equal to 1, 3 and 7, respectively. It is observed that a reduction in error by approximately 4 dB at an NMSE of 10^{-3} is obtained by increasing N_d from one to seven synchronization pilot symbols. However, the synchronization frame overhead increases significantly due to the presence of guard time between individual synchronization pilot symbols.

Figures 5.4 and 5.5 show a 4 and 16 PPM-CAP IR-UWB scheme BER comparison with

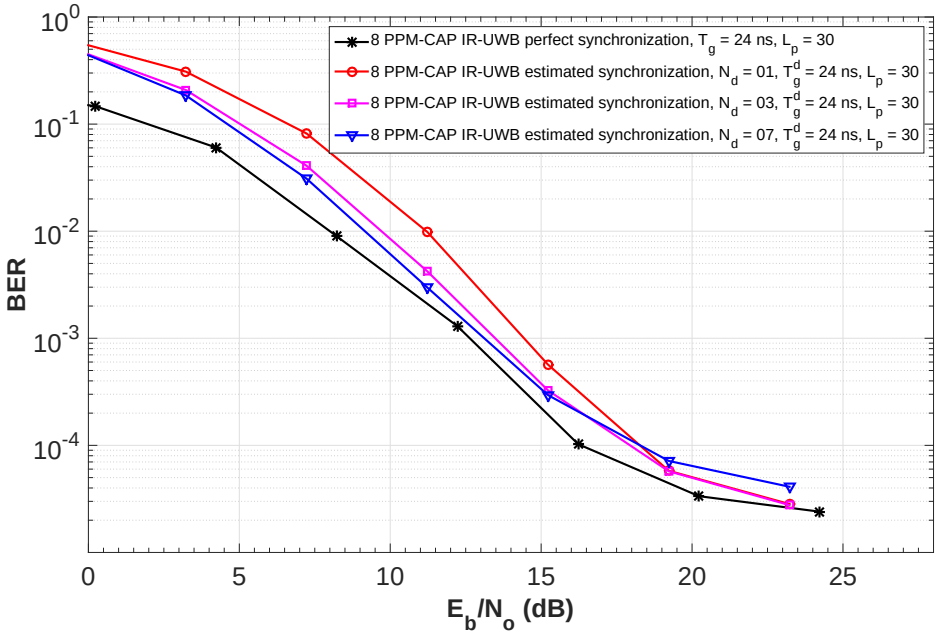

Figure 5.2: BER plots for 8 PPM-CAP IR-UWB with perfect and estimated frame start timing, $L_p = 30$ Rake taps and channel model CM-1.

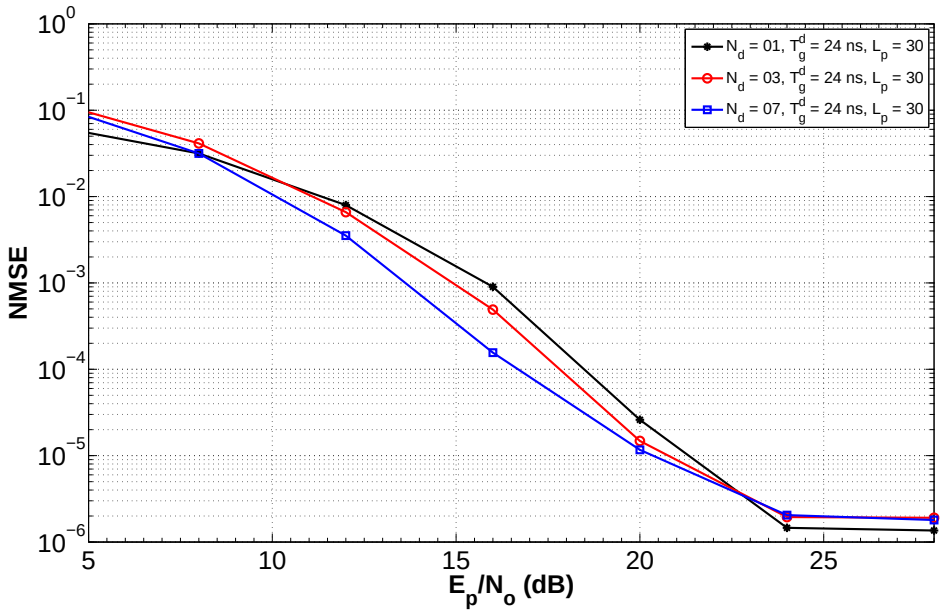

Figure 5.3: NMSE plots for 8 PPM-CAP IR-UWB with different number of pilot symbols N_d.

perfect synchronization and synchronization using timing estimation with 1, 3 and 7 pilot symbols i.e. N_d is equal to 1, 3 and 7. Both have $T_s + T_g$ equal to 32 ns and L_p equal to 30, respectively. From Figure 5.4, 4 PPM-CAP IR-UWB, when the BER is 10^{-2} and $N_d = 1$, has a BER approximately 3.5 dB worse than the perfectly synchronized case. For high E_b/N_o it is observed that the difference in BER performance is negligible. From Figure 5.4, the 16 PPM-CAP IR-UWB scheme, a similar trend can be observed. At a BER of 10^{-2} and for $N_d = 1$, the 16 PPM-CAP IR-UWB scheme with timing estimation is approximately 3 dB worse than the case in which perfect synchronization is assumed. For either high E_b/N_o values or choosing a higher value of N_d, this difference in BER performance becomes negligible when compared to the perfect synchronization case.

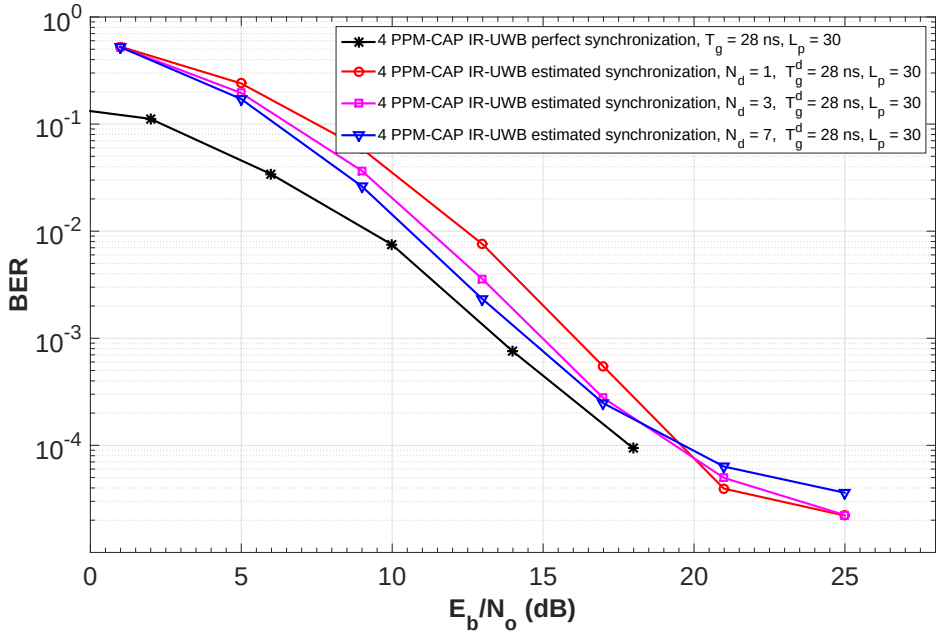

Figure 5.4: BER plots for 4 PPM-CAP IR-UWB with perfect and estimated frame start timing, $L_p = 30$ Rake taps and channel model CM-1

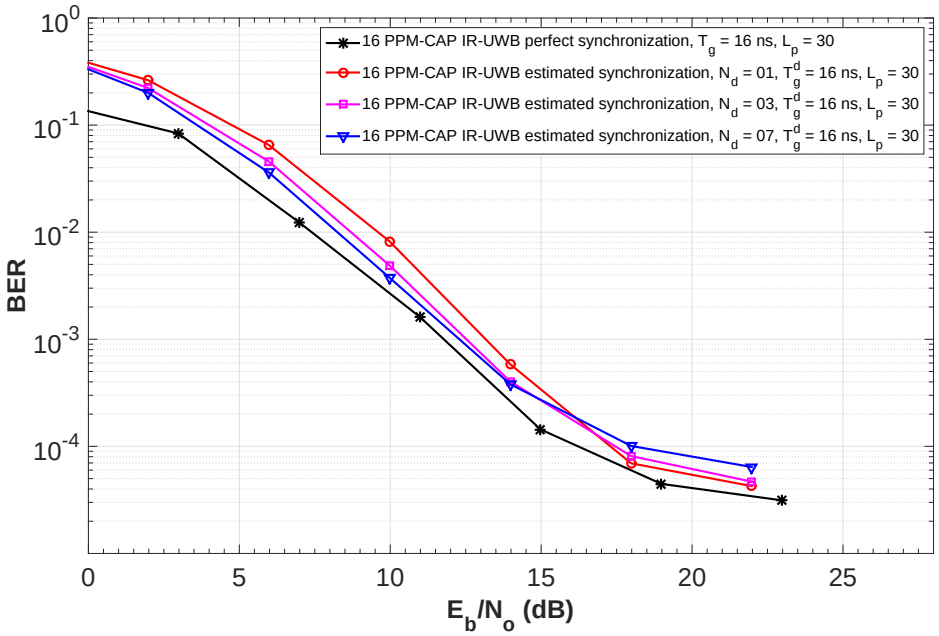

Figure 5.5: BER plots for 16 PPM-CAP IR-UWB with perfect and estimated frame start timing, L_p are 30 Rake taps and channel model CM-1

5.4 CONCLUSIONS

In this chapter a feed-forward data aided synchronization scheme for M-ary PPM-CAP IR-UWB is developed and evaluated. It requires estimation of the data frame start time and knowledge of the frame length at the receiver. Since PPM has fixed symbol lengths provided M is fixed, maintaining symbol synchronization requires a simple symbol rate counter with a count equal to the number of symbols per frame. Both M and the number of symbols per frames are parameters that are set by the system designer so that the receiver has knowledge of them.

Results show that the performance degradation between a PPM-CAP IR-UWB scheme using frame start time estimation is high for low values of transmit signal power or numbers of pilot symbols. This becomes negligible by either increasing transmit signal power or by increasing the number of timing estimation pilot symbols. The next chapter presents potential future work that can be explored for more insight into the PPM-CAP

IR-UWB scheme.

Chapter 6

CONCLUSION AND FUTURE WORK

This chapter reviews and presents conclusion of the work carried out in this thesis. Areas where possible extensions in M-ary PPM-CAP IR-UWB can be carried out are highlighted at the end.

6.1 CONCLUSIONS

A literature review showed that UWB can be implemented in both time and frequency based techniques. Time based UWB is referred to as IR-UWB. It can be implemented via TH coded or DS coded schemes based on PPM. It can even be implemented via uncoded PPM based schemes. In addition, IR-UWB schemes based on bi-orthogonal modulations or bi-polar pulses are also present in the literature, but these require phase information at the receiver for data demodulation. In the frequency domain based UWB schemes, OFDM has been proposed as an alternative with some success. In an AWGN channel, orthogonal pulses or coded schemes with and without bi-orthogonal modulation can be used for system performance evaluation. However, in a multipath channel this is not the case as slight timing offsets in the received components can result in inaccurate detection of one orthogonal pulse shape or code from the other and can even nullify orthogonality between pulses. This makes multipath channel detection techniques significantly different and difficult compared to AWGN channel detection techniques.

Two interesting areas surfaced where there is a lack of detailed performance results at present. The first one is the use of carrierless amplitude phase (CAP) modulation for PPM based IR-UWB. The second is the effect on UWB demodulation and detection when using the full IEEE multipath channel impulse response. Within the area of SISO systems, this thesis showed that using PPM-CAP IR-UWB over simple PPM based IR-UWB provides higher data rates accompanied with a marginal loss in performance, while retaining the same basic receiver structure. In addition, unlike carrier based schemes, PPM-CAP IR-UWB does not require phase information at the receiver for demodulation.

Most of the literature available presents conclusions based on IR-UWB transmission in an IEEE multipath channel that has been significantly truncated to be equal to a single symbol duration at most. Although this does simplify the research methodology, it does not give detailed insight into the full channel response of the proposed schemes because the UWB channel impulse response usually spreads across multiple symbol lengths. The results presented in this thesis are based on the full channel spread of the IEEE UWB channel.

The contributions of this thesis are listed below.

- In Chapter 3, results for PPM IR-UWB in an AWGN channel are first presented. It analytically showed that M-ary PPM IR-UWB can be modelled as an M orthogonal modulation scheme, where the orthogonality lies in using different pulse slots. It compared the analytical upper bound BER plots with those obtained by simulations of an M-ary PPM IR-UWB system. It presented the transmitter and receiver structures of M-ary PPM-CAP IR-UWB along with simulated results. The results showed that both schemes exhibit a similar BER performance. However, M-ary PPM-CAP IR-UWB provides double the data rates compared to M-ary PPM IR-UWB.

- Chapter 4 presented results of both PPM IR-UWB and PPM-CAP IR-UWB in

an IEEE multipath channel. Both of these results are novel and have not been presented in the literature before. Two multipath channel models, CM-1 and CM-4, were considered in this thesis. Simulations considered different pulse time durations, Rake taps, guard time between symbols and different values of M. The following conclusions can be drawn from Chapter 4,

- The pulse time duration effected system performance. A 0.5 ns pulse produced better results than a 1 ns pulse. The narrow pulse widths lead to better received multipath component resolution and hence improved BER rates.
- The results showed system performance for L_p of 5, 15 and 30 taps in both CM-1 and CM-4 models. System BER performance showed improvement by increasing the number of Rake taps L_p to 15 taps or more. However, L_p equal to 15 taps was sufficient to attain a BER of 10^{-3} in CM-1. In a CM-4 channel the system required L_p to be equal to 30 Rake taps or more for attaining a BER of 10^{-3}.
- An important parameter that improved system performance in a multipath channel is the choice of guard time T_g. The results showed that for 2, 4, 8 and 16 -ary schemes with L_p greater or equal to 15 Rake taps, a guard time of 30 ns, 28 ns, 24 ns and 16 ns respectively achieved system performance in the BER region of 10^{-4} for CM-1.
- Lastly, Chapter 4 described two different modulation formats for PPM-CAP IR-UWB along with a brief comparison of the two schemes. The results showed that both schemes perform similarly with some difference in error floor of the BER plots. However, format B gives slight performance gain over format A when M is equal to 2 or 4. The gain in performance is negligible for higher values of M, making format B the more versatile scheme with easier manipulation of the length of guard time to be inserted between ensuing symbols.

- Chapter 5 discussed a novel synchronization scheme for PPM-CAP IR-UWB. The scheme takes a feed-forward data aided approach to achieve frame synchronization. It showed that there is a performance loss ranging between 3 dB to 5 dB, depending on the factors such as channel model, Rake taps and number of synchronization symbols, compared to the relative case using ideal synchronization. The chapter assumes L_p equal to 30 Rake taps and varies the number of synchronization pilot symbols to present system performance.

In summary, M-ary PPM-CAP IR-UWB achieved good BER performance in a CM-1 channel provided that the Rake had 15 or more taps and a guard time of 24 ns or more inserted between symbols to minimize ISI. A higher M-ary scheme obtained better BER performance and data rates than a lower M-ary scheme as observed from the results. Two proposed modulation formats were described and simulated. Modulation format A is more robust in terms of BER performance. A feed-forward synchronization scheme was described, which relied on seven pilot symbols to attain a BER performance approximately equal to that achieved by an ideally synchronized scheme having equivalent system parameters. This reduces frame overhead hence increasing the effective data rate per transmission.

6.2 FUTURE WORK

This section presents possible future research direction to that already discussed in this thesis. The work in this thesis primarily focuses on single input single output impulse radio UWB communication. It assumes that perfect channel state information is available at the receiver. Pulse distortion caused by objects in the signal propagation path or antenna effects on pulse transmission are ignored. There is room for further extension of the current work as detailed below

1. PPM-CAP IR-UWB with different pulse shapes:

   The results in this thesis are presented using the Scholtz monocycle pulse. Chapter

2 briefly touches on literature covering pulse design for IR-UWB. It was seen that there are numerous pulse design techniques other than the one presented in this thesis. The performance of using pulse shapes based on the derivatives of the Gaussian function is an area of extension to the current work. By modelling other pulse design techniques for PPM-CAP IR-UWB we can explore the system performance dependance on choice of pulse shapes more accurately.

2. Effect of Antenna of PPM-CAP IR-UWB:

   Pulse distortion due to objects occurring in the path of pulse propagation and due to different pulse frequencies is an area that can increase the accuracy of received pulse shapes taking into account antenna design. By simulating a multipath channel which includes the effects of transmitting and receiving antennas on pulse shapes we can precisely model a PPM-CAP system from a hardware development aspect.

3. Effect of Channel Estimation:

   This thesis assumes that perfect channel state information is present at the receiver. However, in a multipath channel environment the receiver will need to estimate the channel components and perform some form of equalization before detection is carried out. Performance of PPM-CAP using channel estimation techniques will significantly increase the accuracy of the current system model.

4. Effect of System Coding on Performance:

   This thesis assumes uncoded IR-UWB communication employing PPM-CAP. It can be extended to multi-user systems by employing time hop codes in the signalling format that is used in TH IR-UWB.

   Another method for achieving orthogonality are using orthogonal codes. These can be applied to not only make multi-user performance possible but could potentially introduce better performance in the existing SISO system setup.

5. Closed Loop Synchronization:

   Closed loop synchronization techniques using phase lock loops or delay lock loops have been studies in the literature extensively. These techniques are significantly complex when compared to feed-forward synchronization techniques. A closed loop system for PPM-CAP IR-UWB remains an open area for investigation in both CM-1 and CM-4 channel model environments. This can potentialy increase the synchronization lock obtained in PPM-CAP IR-UWB.

6. PPM-CAP IR-UWB in IEEE 802.15.4a Channel Model:

   Channel model 802.15.4a is a relatively new channel model that defines UWB multipath propagation in a number of different scenarios. It has six channel models and presents different fading characteristics of the multipath channel. Simulating PPM-CAP IR-UWB in these channel environments will provide insight into performance in body area networks and low frequency communication systems.

7. Statistical System Performance Analysis:

   System performance can alternatively be presented by statistical modelling of IR-UWB systems. Such modelling results in approximations to analytical equations that deduce probability of error primarily due to the complex mathematical forms involved. It will be useful to derive closed form statistical solutions for PPM-CAP IR-UWB in the multipath channel.

8. Location Tracking and Asset Localization:

   Current UWB devices manufactured by companies such as Decawave and Zebra Technologies can provide centimeter level accuracy in asset location detection even in the presence of objects that induce a multipath channel environment. Indoor asset localization and object tracking are two interesting and commercial applications in which UWB is being considered due to low power consumption. PPM-CAP IR-UWB follows closely the classical IR-UWB principles and is an improvement to current IR-UWB schemes. Its dual pulse nature provides not only high data rates

but accurate synchronization requiring a small number of pilot symbols. Further research into hardware design will give insight into its performance for accurate location tracking.

9. Energy requirements of PPM-CAP IR-UWB systems:

   Energy and battery life requirements of any communication scheme plays an important role in its commercial deployment. While energy comsumption is very much dependant on the technology used in manufacturing the device along with its intended application, UWB in general has seen transceivers being introduced for commercial use by companies such as Decawave due to having low power consumption (as low as 0.230mW for their DW1000 UWB tranceiver having range of up to 300m). Current research into UWB tranceivers is in the 65 nm CMOS technology having power consumption as little as 3.5mW [152] [153] [154]. Implementing PPM-CAP IR-UWB in CMOS technology would enable its use in low power consumption applications such as location tracking or RFID tags.

REFERENCES

[1] D. Cichon and W. Wiesbeck, "The Heinrich Hertz wireless experiments at Karlsruhe in the view of modern communication," in *Proc. International Conference on 100 Years of Radio*, September 1995, pp. 1 –6.

[2] W. Wlesbeck and D. J. Clchon, "The link from Heinrich Hertz to modern communication," in *Proc. European Microwave Conference*, vol. 2, September 1995, pp. 886 –894.

[3] C. Susskind, "Heinrich Hertz: a short life," *IEEE Transactions on Microwave Theory and Techniques*, vol. 36, no. 5, pp. 802 –805, May 1988.

[4] J. Kraus, "Heinrich Hertz-theorist and experimenter," in *IEEE MTT-S International Microwave Symposium Digest*, vol. 1, May 1988, pp. 271 –272.

[5] B. Allen, M. Dohler, E. E. Okon, W. Q. Malik, A. K. Brown, and D. J. Edwards, *Ultra-Wideband Antennas and Propagation for Communications Radar and Imaging.* Chichester, West Sussex, England : John Wiley & Sons Ltd., 2007, ISBN 13 978-0-470-03255-8 (HB).

[6] G. Giancola and M.-G. Di Benedetto, *Understanding Ultra wideband Radio Fundamentals*, ser. Prentice Hall communications engineering and emerging technologies series. Upper Saddle River, N.J. : Prentice Hall PTR, 2004, ISBN 9780131480032.

[7] A. F. M. I. O. C. P. Maria-Gabriella Di Benedetto, Thomas Kaiser and D. Porcino, *Ultra-Wideband Communication Systems-A Comprehensive Overview.* Hindawi Publishing Corporation, 2006, ISBN 977-5945-10-0.

[8] J. M. Wilson, "Ultra-Wideband / a Disruptive RF Technology ?" Intel Research and Development, Version 1.3, USA, Tech. Rep., September 2002.

[9] G. Marconi, "Wireless telegraphy," *Journal of the Institution of Electrical Engineers*, vol. 28, no. 139, pp. 273 –290, April 1899.

[10] S. Marconi, "Radio Telegraphy," *Proceedings of the Institute of Radio Engineers*, vol. 10, no. 4, pp. 215 – 238, August 1922.

[11] G. Marconi, "Radio communications by means of very short electric waves," *IRE Transactions on Antennas and Propagation*, vol. 5, no. 1, pp. 90–99, January 1957.

[12] M. Z. Win and R. A. Scholtz, "Impulse Radio: How It Works," *IEEE Communications Letters*, vol. 2, no. 2, pp. 36 – 38, February 1998.

[13] F. E. Aranda, N. Brown, and H. Arslan, "Rake Receiver Finger Assignment for Ultra-Wideband Radio," in *IEEE Workshop on Signal Processing Advances in Wireless Communications*, June 2003.

[14] M. Sahin and H. Arslan, "Inter-symbol interference in high data rate UWB communications using energy detector receivers," in *Proc. International Conference on Ultra-wideband*, 2005, pp. 176–179.

[15] F. Ramirez-Mireles, "Performance of UWB N-Orthogonal PPM in AWGN and Multipath Channels," *IEEE Transactions on Vehicular Technology*, vol. 56, no. 3, pp. 1272–1285, May 2007.

[16] H. Zhang and T. Gulliver, "Biorthogonal pulse position modulation for time-hopping multiple access UWB communications," *IEEE Transactions on Wireless Communications*, vol. 4, no. 3, pp. 1154 – 1162, May 2005.

[17] S. Majhi, A. Madhukumar, A. Premkumar, and F. Chin, "M-ary Signaling for Ultra Wideband Communication Systems Based on Pulse Position and Orthogonal Pulse Shape Modulation," in *Proc. WCNC*, 2007, pp. 2795–2799.

[18] R. A. Scholtz, D. M. Pozar, and W. Namgoong, "Ultra-Wideband Radio," *EURASIP Journal on Applied Signal Processing*, vol. 3, pp. 252–272, 2005.

[19] F. Ramirez-Mireles and R. Scholtz, "System performance analysis of impulse radio modulation," in *Proc. IEEE Radio and Wireless Conference (RAWCON)*, August 1998, pp. 67 –70.

[20] R. Scholtz, "Multiple access with time-hopping impulse modulation," in *Proc. IEEE Military Communications Conference (MILCOM)*, vol. 2, October 1993, pp. 447 –450.

[21] R. Scholtz, R.-M. Cramer, and M. Win, "Evaluation of the propagation characteristics of ultra-wideband communication channels," in *IEEE Antennas and Propagation Society International Symposium*, June 1998.

[22] M. Win, "Spectral density of random time-hopping spread-spectrum UWB signals with uniform timing jitter," in *Proc. IEEE Military Communications Conference Proceedings (MILCOM)*, vol. 2, 1999, pp. 1196 –1200.

[23] ——, "Spectral density of random UWB signals," *IEEE Communications Letters*, vol. 6, no. 12, pp. 526 –528, December 2002.

[24] F. Ramirez-Mireles, M. Z. Win, and R. A. Scholtz, "Signal Selection for the Indoor Wireless Impulse Radio Channel," in *IEEE Vehicular Technology Conference (VTC)*, May 1997.

[25] A. F. Molisch, J. R. Foerster, and M. Pendergrass, "Channel models for ultrawideband personal area networks," *IEEE Magazine on Wireless Communications*, vol. 10, no. 6, pp. 14 – 21, December 2003.

[26] A. Molisch, "Ultra-Wide-Band Propagation Channels," *Proc. of the IEEE*, vol. 97, pp. 353–371, 2009.

[27] Y. Wu, A. Molisch, S.-Y. Kung, and J. Zhang, "Impulse radio pulse shaping for ultra-wide bandwidth (UWB) systems," in *Proc. PIMRC*, vol. 1, September 2003, pp. 877 – 881.

[28] L. Yang and G. B. Giannakis, "Ultra-Wideband Communications: An Idea Whose Time Has Come," *IEEE Signal Processing Magazine*, vol. 21, no. 6, pp. 26–54, November 2004.

[29] X. Wu, Z. Tian, T. N. Davidson, and G. B. Giannakis, "Optimal Waveform Design for UWB Radios," *IEEE Transactions on Signal Processing*, vol. 54, no. 6, pp. 2009–2021, June 2006.

[30] S. Gezici, H. Kobayashi, and H. Poor, "A comparative study of pulse combining schemes for impulse radio UWB systems," in *Proc. IEEE/Sarnoff Symposium on Advances in Wired and Wireless Communication*, April 2004, pp. 7 – 10.

[31] M. Chiani and A. Giorgetti, "Coexistence between UWB and Narrow-Band Wireless Communication Systems," *in Proc. of the IEEE*, vol. 97, no. 2, pp. 231–253, February 2009.

[32] M. Fatehy and R. Kohno, "Variable Spread Slotted Aloha Simulation Analysis over IEEE 802.15.6 Using IR-UWB for Wireless Body Area Networks," in *Proc. European Modelling Symposium (EMS)*, November 2013, pp. 572–577.

[33] T. Paso, J. Haapola, and J. Iinatti, "Feasibility study of IEEE 802.15.4e DSME utilizing IR-UWB and S-Aloha," in *Proc. Personal Indoor and Mobile Radio Communications (PIMRC)*, September 2013, pp. 1863–1867.

[34] H.-X. Tan, R. Patro, M.-C. Chan, P.-Y. Kong, and C.-K. Tham, "Performance of Slotted-Aloha over TH-UWB," in *Proc. IEEE International Conference on Ultra-Wideband (ICUWB)*, September 2007, pp. 868–873.

[35] J. Metzner, "Interference-Avoiding features of Ultra-Wideband Communication and Wideband ALOHA," in *Proc. Asilomar Conference on Signals, Systems and Computers*, vol. 2, November 2004, pp. 1453–1457.

[36] M. G. M. Hussain, "Waveform design and modulation schemes for impulse communications and radar," in *Waveform Diversity and Design Conference*, June 2007.

[37] S. Gezici and H. Poor, "Position Estimation via Ultra-Wide-Band Signals," *Proceedings of the IEEE*, vol. 97, no. 2, pp. 386 –403, February 2009.

[38] W. Liu, H. Ding, X. Huang, and Z. Liu, "TOA Estimation in IR UWB Ranging with Energy Detection Receiver Using Received Signal Characteristics," *IEEE Communications Letters*, vol. 16, no. 5, pp. 738 –741, May 2012.

[39] A. Fujii, H. Sekiguchi, M. Asai, S. Kurashima, H. Ochiai, and R. Kohno, "Impulse Radio UWB Positioning System," in *IEEE Radio and Wireless Symposium*, January 2007.

[40] N. Decarli, F. Guidi, and D. Dardari, "Passive UWB RFID for Tag Localization: Architectures and Design," *IEEE Sensors Journal*, vol. 16, no. 5, pp. 1385–1397, March 2016.

[41] H. Liu, J. Sarrazin, T. Mavridis, L. Petrillo, Z. Liu, P. De Doncker, and A. Benlarbi-Delai, "Performance Assessment of IR-UWB Body Area Network (BAN) based on IEEE 802.15.6 Standard," *IEEE Antennas and Wireless Propagation Letters*, vol. PP, no. 99, pp. 1–1, February 2016.

[42] M. Malekizandi, Q. T. Le, A. Emsia, D. Briggmann, and F. Kuppers, "Generation of UWB Doublet Pulse Based on Directly Modulated Laser and Chromatic Dispersion," *IEEE Photonics Technology Letters*, vol. 28, no. 3, pp. 343–346, February 2016.

[43] K. Xu, X. Wu, J.-Y. Sung, Z. Cheng, C. W. Chow, Q. H. Song, and H. ki Tsang, "Amplitude and Phase Modulation of UWB Monocycle Pulses on a Silicon Photonic Chip," *IEEE Photonics Technology Letters*, vol. 28, no. 3, pp. 248–251, February 2016.

[44] M. Yang, X. Yin, Y. Li, and L. Liu, "Ultra-Wideband Planar Gaussian Tapered Rhombic Antenna for Short Pulse Applications," *IEEE Antennas and Wireless Propagation Letters*, vol. 15, pp. 48–51, February 2016.

[45] R. Krishna and R. Kumar, "A Dual-Polarized Square-Ring Slot Antenna for UWB, Imaging, and Radar Applications," *IEEE Antennas and Wireless Propagation Letters*, vol. 15, pp. 195–198, February 2016.

[46] A. Ahmed, Y. Zhang, D. Burns, D. Huston, and T. Xia, "Design of UWB Antenna for Air-Coupled Impulse Ground-Penetrating Radar," *IEEE Geoscience and Remote Sensing Letters*, vol. 13, no. 1, pp. 92–96, January 2016.

[47] J. Zhang, P. Cao, Y. Huang, R. Alrawashdeh, and X. Zhu, "Compact planar ultra-wideband antenna with quintuple band-notched characteristics," *IET Microwaves, Antennas and Propagation*, vol. 9, no. 3, pp. 206–216, February 2015.

[48] W. Jeong and J. Choi, "A Low Profile IR-UWB Antenna with Conical Radiation Pattern for on-body Communications," in *Proc. International Symposium on Antennas and Propagation USNC/URSI National Radio Science Meeting*, July 2015, pp. 2023–2024.

[49] FCC, "Third memorandum opinion and order," Federal Communications Commission, USA, FCC 10-151, USA, Tech. Rep., August 2010.

[50] H. Mazar, "A comparison between European and North American wireless regulations," in *Technical Symposium at ITU*, October 2011, pp. 182 –186.

[51] N. Salman, I. Rasool, and A. Kemp, " IEEE Overview of the 802.15.4 standards family for Low Rate Wireless Personal Area Networks," in *Proc. International Symposium on Wireless Communication Systems (ISWCS* , September 2010, pp. 701 –705.

[52] M. Z. Win, D. Dardari, A. F. Molisch, W. Wiesbeck, and J. Zhang, "History and Applications of UWB," in *Proceedings of the IEEE*, vol. 97, no. 2, February 2009, pp. 198–204, ISSN: 0018-9219.

[53] G. R. Aiello and G. D. Rogerson, "Ultra-Wideband Wireless Systems," *IEEE Microwave Magazine*, June 2003.

[54] K. Witrisal, G. Leus, G. Janssen, M. Pausini, F. Troesch, T. Zasowski, and J. Romme, "Noncoherent Ultra-Wideband Systems," *IEEE Signal Processing Magazine*, vol. 26, pp. 1053 – 5888, July 2009.

[55] H. Arslan, Z. N. Chen, and M.-G. Di Benedetto, *Ultra Wideband Wireless Communication.* Hoboken, New Jersey : Wiley-Interscience, 2006, ISBN 0-471-71521-2(cloth).

[56] R. Aiello and A. Batra, *Ultra-Wideband Systems Technologies and Applications.* Newnes, Elsevier Inc. Oxford, 2006, ISBN 0-7506-7893-3.

[57] R. Kshetrimayum, "An introduction to UWB communication systems," *IEEE Potentials*, vol. 28, no. 2, pp. 9 –13, March-April 2009.

[58] M. Win and R. Scholtz, "On the energy capture of ultrawide bandwidth signals in dense multipath environments," *IEEE Communications Letters*, vol. 2, no. 9, pp. 245–247, September 1998.

[59] M. Win, F. Ramirez-Mireles, R. Scholtz, and M. Barnes, "Ultra-wide bandwidth (UWB) signal propagation for outdoor wireless communications," in *Proc. IEEE Vehicular Technology Conference (VTC)* , vol. 1, May 1997, pp. 251–255.

[60] A. Batra, J. Balakrishnan, and A. Dabak, "Multi-band OFDM: a new approach for UWB," *Proc. International Symposium on Circuits and Systems (ISCAS)*, vol. 5, pp. 365–368, May 2004.

[61] A. T. Kalghatgi, "Challenges in the Design of an Impulse Radio based Ultra Wide Band Tranceiver," in *Proc. International Conference of Signal Processing, Communications and Networking*, Madras Institute of Technology, Anna University, Chennai, India, February 2007, pp. 1–5.

[62] I. F. Akyildiz, B. F. Lo, and R. Balakrishnan, "Spectrum Sharing Radios," *Elsevier Journal of Physical Communication*, vol. 4, no. 1, pp. 40 – 62, March 2011.

[63] D. Cabric, I. D. O'Donnell, M. S.-W. Chen, and R. W. Brodersen, "Cooperative spectrum sensing in cognitive radio networks: A survey," *Elsevier Journal of Physical Communication*, vol. 4, pp. 30 – 45, Second Quarter 2006.

[64] J. Romme and L. Piazzo, "On the power spectral density of time-hopping impulse radio," in *Proc. IEEE Conference on Ultra Wideband Systems and Technologies*, 2002, pp. 241 – 244.

[65] A. Rabbachin, T. Quek, P. Pinto, I. Oppermann, and M. Win, "Non-Coherent UWB Communication in the Presence of Multiple Narrowband Interferers," *IEEE Transactions on Wireless Communications*, vol. 9, no. 11, pp. 3365 –3379, November 2010.

[66] A. F. Molisch, *Wireless Communications, 2nd Edition.* John Wiley & Sons Ltd., 2010, ISBN 978-0-470-74187-0.

[67] J. Ono, T. Tsunoda, K. Ohno, and M. Itami, "A study on RAKE reception using multicarrier template waveform for UWB-IR system," in *Proc. IEEE International Conference on Ultra-Wideband (ICUWB)*, September 2012, pp. 212–216.

[68] C. Din, W. Mansor, and R. Mohamad, "A review on modulation techniques in multiband-orthogonal frequency division multiplexing in ultra-wideband channel," in *Proc. IEEE Symposium on Computers and Informatics (ISCI)*, March 2011, pp. 576 – 582.

[69] J. F. M. Gerrits, J. R. Farserotu, and J. R. Long, "Low Complexity Ultra Wide Band Communications," *IEEE Transactions on Circuits and Systems ii: Express Briefs*, vol. 55, no. 4, pp. 329–333, April 2008.

[70] J. F. M. Gerrits and J. R. Farserotu, "Ultra Wideband FM: A Straightforward Frequency Domain Approach," in *Proc. European Microwave Conference*, October 2003, pp. 853–856.

[71] J. F. M. Gerrits, M. H. L. Kouwenhoven, P. R. van der Meer, J. R. Farserotu, and J. R. Long, "Principles and Limitations of Ultra-Wideband FM Communications Systems," *Proc. EUROSIP journal on Applied Signal Processing*, vol. 3, pp. 382–396, 2005.

[72] C. Carbonelli and U. Mengali, "M-PPM noncoherent receivers for UWB applications," *IEEE Transactions on Wireless Communications*, vol. 5, no. 8, pp. 2285–2294, August 2006.

[73] H. Sheng, P. Orlik, A. Haimovich, J. Cimini, L.J., and J. Zhang, "On the Spectral and Power Requirements for Ultra-Wideband Transmission," in *IEEE International Conference on Communications (ICC)*, May 2003.

[74] B. Hu and N. Beaulieu, "Pulse Shaping in UWB Communication Systems," in *IEEE Vehicular Technology Conference (VTC)*, September 2004.

[75] W. Tjhi, C. T. Lau, and A. Premkumar, "Performance of Different UWB Pulse Shapes Under High Data Rate Indoor Channel," in *Proc. IEEE Wireless Communications and Networking Conference (WCNC)*, March 2007, pp. 1751 – 1756.

[76] D. Wentzloff, R. Blazquez, F. Lee, B. Ginsburg, J. Powell, and A. Chandrakasan, "System design considerations for ultra-wideband communication," *IEEE Communications Magazine*, vol. 43, no. 8, pp. 114 – 121, August 2005.

[77] M. Mirshafiei, M. Abtahi, and L. Rusch, "Ultra-wideband pulse shaping: bypassing the inherent limitations of the Gaussian monocycle," *IET Communications*, vol. 6, no. 9, pp. 1068 –1074, 2012.

[78] B. Godara, G. Blamon, and A. Fabre, "UWB: A New Efficient Pulse Shape and its Corresponding Simple Tranceiver," in *International Symposium on Wireless Communication Systems*, September 2005.

[79] R. Thai-Singama, M. Piette, and F. Du-Burck, "A low-cost UWB Gaussian, monocycle and doublet generation based on the transient response of band-pass filters," in *Proc. General Assembly and Scientific Symposium, XXXth URSI*, August 2011, pp. 1–4.

[80] B. Parr, B. Cho, K. Wallace, and Z. Ding, "A Novel Ultra-Wideband Pulse Design Algorithm," *IEEE Communications Letters*, vol. 7, no. 5, pp. 219 – 221, May 2003.

[81] X. Luo, L. Yang, and G. Giannakis, "Designing Optimal Pulse-Shapers for Ultra-Wideband Radios," in *Proc. IEEE Conference on Ultra Wideband Systems and Technologies*, November 2003, pp. 349 – 353.

[82] D. Slepian and H. O. Pollak, "Prolate Spheroidal Wave Functions, Fourier Analysis, and Uncertainty -I," *Bell Syst. Tech. Journal*, vol. 40, no. 1, pp. 43–46, January 1961.

[83] L. Michael, M. Ghavami, and R. Kohno, "Multiple pulse generator for ultra-wideband communication using Hermite polynomial based orthogonal pulses," in *Proc. IEEE Conference on Ultra Wideband Systems and Technologies*, August 2002, pp. 47 – 51.

[84] M. Ghavami, L. Michael, and R. Kohno, "Hermite Function based Orthogonal Pulses for UWB Communications," *Proc. Wireless Personal Multimedia Conference*, pp. 437–440, September 2001.

[85] M. Biagi and V. Polli, "UltraWide Band Cognitive Pulse Shaping under Physical-Layer QoS Constraints ," *IEEE Transactions on Communications*, vol. 59, no. 11, pp. 3167 – 3176, November 2011.

[86] W. Gao, R. Venkatesan, and C. Li, "A Pulse Shape Design Method for Ultra-Wideband Communications," in *Proc. IEEE Wireless Communications and Networking Conference (WCNC)*, March 2007, pp. 2800 – 2805.

[87] H. Sheng, P. Orlik, A. Haimovich, J. Cimini, L.J., and J. Zhang, "On the Spectral and Power Requirements for Ultra-Wideband Transmission," in *IEEE International Conference on Communications (ICC)*, May 2003.

[88] L. Zhao and A. Haimovich, "Performance of ultra-wideband communications in the presence of interference," *IEEE Journal on Selected Areas in Communications*, vol. 20, no. 9, pp. 1684–1691, December 2002.

[89] H. Chen, Z. Jia, and X. Cai, "Waveform Design for UWB Communications Based on Combined Sinusoid Gaussian Pulse," in *Proc. International Conference on Computer, Mechatronics, Control and Electronic Engineering (CMCE)*, vol. 6, August 2010, pp. 267 – 271.

[90] Z. Jia, H. Chen, X. Cai, and X. Chen, "A Novel Pulse Design Based on Sinusoid Gaussian Function for UWB Communication," in *Proc. IEEE International Con-*

ference on Broadband Network and Multimedia Technology (IC-BNMT), October 2010, pp. 1240 – 1244.

[91] A. Iqbal, S. Islam, and K.-S. Kwak, "A study on the performance of UWB-MIMO detection techniques," in *Proc. Third International Conference on Ubiquitous and Future Networks (ICUFN)*, June 2011, pp. 220–223.

[92] J. M. Wozencraft and I. M. Jacobs, *Principles of Communication Engineering*. John Wiley & Sons, Inc., New York, 1965.

[93] J. G. Proakis and M. Salehi, *Communication Systems*. Prentice Hall, Inc., 1994, ISBN 0-13-300625-5.

[94] S. Haykin, *Communication Systems*. John Wiley & Sons, Inc., New York, USA, 2001, ISBN 0-471-17869-1.

[95] J. C. Hancock and P. A. Wintz, *Signal Detection Theory*. McGraw-Hill Book Company, 1966.

[96] A. Saleh and R. Valenzuela, "A Statistical Model for Indoor Multipath Propagation," *IEEE Journal on Selected Areas in Communications*, vol. 5, no. 2, pp. 128 –137, February 1987.

[97] G. Turin, F. Clapp, T. Johnston, S. Fine, and D. Lavry, "A statistical model of urban multipath propagation," *IEEE Transactions on Vehicular Technology*, vol. 21, pp. 1–9, 1972.

[98] G. L. Turin, "Communication Through Noise, Random-Multipath Channels," Ph.D. dissertation, Massachusetts Institute of Technology, June 1956.

[99] H. Suzuki, "A Statistical Model for Urban Radio Propogation," *IEEE Transactions on Communications*, vol. 25, no. 7, 1977.

[100] H. Hashemi, "Simulation of the urban radio propagation channel," *IEEE Transactions on Vehicular Technology*, vol. 28, no. 3, pp. 213–225, 1979.

[101] ——, "The indoor radio propagation channel," *Proc. of the IEEE*, vol. 81, no. 7, pp. 943–968, 1993.

[102] Q. Zhang and J. H. Cho, "On RAKE Receivers for Ultra-Wideband Binary Block-Coded PPM in Dense Multipath Channels," *IEEE Transactions on Vehicular Technology*, vol. 56, no. 4, pp. 1737–1748, July 2007.

[103] M. Win, G. Chrisikos, and N. Sollenberger, "Performance of RAKE reception in dense multipath channels: implications of spreading bandwidth and selection diversity order," *IEEE Journal on Selected Areas in Communications*, vol. 18, no. 8, pp. 1516–1525, August 2000.

[104] R. Price and P. Green, "A Communication Technique for Multipath Channels," *Proc. of the IRE*, vol. 46, no. 3, pp. 555–570, March 1958.

[105] M. K. Simon and M. S. Alouini, *Digital Communication over Fading Channels - A Unified Approach to Performance Analysis.* John Wiley & Sons, Inc., 2000, ISBN 9780471317791.

[106] G. Bottomley, T. Ottosson, and Y.-P. Wang, "A generalized RAKE receiver for interference suppression," *IEEE Journal on Selected Areas in Communications*, vol. 18, pp. 1536–1545, August 2000.

[107] A. Rajeswaran, V. Somayazulu, and J. Foerster, "RAKE performance for a pulse based UWB system in a realistic UWB indoor channel," in *Proc. ICC*, May 2003, pp. 2879–2883.

[108] B. S. Kim, J. Bae, I. Song, S. Y. Kim, and H. Kwon, "A Comparative Analysis of Optimum and Suboptimum Rake Receivers in Impulsive UWB Environment," *IEEE Transactions on Vehicular Technology*, vol. 55, no. 6, pp. 1797–1804, November 2006.

[109] A. Klein, I. Brown, D.R., D. Goeckel, and C. Johnson, "RAKE reception for UWB communication systems with intersymbol interference," in *IEEE Workshop on Signal Processing Advances in Wireless Communications (SPAWC)*, June 2003, pp. 244–248.

[110] N. Boubaker and K. Letaief, "A low complexity MMSE-RAKE receiver in a realistic UWB channel and in the presence of NBI," in *Proc. IEEE Wireless Communications and Networking (WCNC)*, vol. 1, March 2003, pp. 233–237.

[111] D. Cassioli, M. Win, F. Vatalaro, and A. Molisch, "Low Complexity Rake Receivers in Ultra-Wideband Channels," *IEEE Transactions on Wireless Communications*, vol. 6, no. 4, pp. 1265–1275, April 2007.

[112] V. Sipal, B. Allen, and D. Edwards, "Analysis and mitigation of antenna effects on wideband wireless channel," *IET Electronics Letters*, vol. 46, no. 16, pp. 1159–1160, August 2010.

[113] B. Xia, N. Xie, and J. Li, "Wavelet-based pulse design for UWB vehicular radar," in *IEEE International Symposium on Microwave, Antenna, Propagation and EMC Technologies for Wireless Communications*, October 2009.

[114] L. Fullerton, "UWB waveforms and coding for communications and radar," in *Proc. of National Telesystems Conference (NTC)*, vol. 1, March 1991, pp. 139 –141.

[115] K. Siwiak, "Ultra-wide band radio: introducing a new technology," in *Proc. Vehicular Technology Conference (VTC)*, vol. 2, 2001, pp. 1088–1093.

[116] G.-H. Im and J. Werner, "Bandwidth-efficient digital transmission up to 155 Mb/s over unshielded twisted pair wiring," in *IEEE International Conference on Communications, Geneva*, vol. 3, May 1993.

[117] I. Thng, X. Li, and C. C. Ko, "A new 3D CAP system," in *Proc. IEEE Region 10 Conference (TENCON)*, vol. 1, 1999, pp. 309 –312.

[118] G.-H. Im, D. Harman, G. Huang, A. Mandzik, M.-H. Nguyen, and J.-J. Werner, "51.84 Mb/s 16-CAP ATM LAN standard," *IEEE Journal on Selected Areas in Communications*, vol. 13, pp. 620 –632, May 1995.

[119] H. Bidgoli, *Handbook of Computer Networks volume 1.* John Wiley & Sons, Inc., 2008, ISBN 978-0-471-78458-6.

[120] J. Wei, J. Ingham, D. Cunningham, R. Penty, and I. White, "Performance and Power Dissipation Comparisons Between 28 Gb/s NRZ, PAM, CAP and Optical OFDM Systems for Data Communication Applications," *Journal of Lightwave Technology*, vol. 30, no. 20, pp. 3273 –3280, October 2012.

[121] G.-H. Im and J.-J. Werner, "Bandwidth-efficient digital transmission over unshielded twisted-pair wiring," *IEEE Journal on Selected Areas in Communications*, vol. 13, no. 9, pp. 1643 –1655, December 1995.

[122] A. Abdolhamid and D. Johns, "A comparison of CAP/QAM architectures," in *Proc. ISCAS*, vol. 4, May-June 1998.

[123] A. Shalash and K. Parhi, "Multidimensional carrierless AM/PM systems for digital subscriber loops," *IEEE Transactions on Communications*, vol. 47, no. 11, pp. 1655 –1667, November 1999.

[124] X. Liu, A. Premkumar, and A. Madhukumar, "Pulse Shaping Functions for UWB Systems," *IEEE Transactions on Wireless Communications*, vol. 7, no. 5, pp. 1512–1516, May 2008.

[125] G. Durisi and G. Romano, "Simulation analysis and performance evaluation of an UWB system in indoor multipath channel," in *Proc. IEEE Conference on Ultra Wideband Systems and Technologies*, May 2002, pp. 255–258.

[126] L. Wu, X. Wu, and Z. Tian, "Asymptotically optimal UWB receivers with noisy templates: design and comparison with RAKE," *IEEE Journal on Selected Areas in Communications*, vol. 24, no. 4, pp. 808–814, April 2006.

[127] X. Dong, A. Lee, and L. Xiao, "A new UWB dual pulse transmission and detection technique," in *Proc. IEEE International Conference on Communications (ICC)*, vol. 4, May 2005, pp. 2835–2839.

[128] P. Liu and Z. Xu, "POR-based channel estimation for UWB communications," *IEEE Transactions on Wireless Communications*, vol. 4, no. 6, pp. 2968–2982, November 2005.

[129] T. Ezaki and T. Ohtsuki, "Diversity gain in ultra wideband impulse radio (UWB-IR)," in *Proc. IEEE Conference on Ultra Wideband Systems and Technologies*, November 2003, pp. 56–60.

[130] X. Zuo, D. Wang, and R. Yao, "RAKE reception for IR-UWB systems in high mobile environments," in *Proc. International Conference on Systems and Informatics (ICSAI)*, May 2012, pp. 1459–1462.

[131] A. Molisch, D. Cassioli, C.-C. Chong, S. Emami, A. Fort, B. Kannan, J. Karedal, J. Kunisch, H. Schantz, K. Siwiak, and M. Win, "A Comprehensive Standardized Model for Ultrawideband Propagation Channels," *IEEE Transactions on Antennas and Propagation*, vol. 54, no. 11, pp. 3151–3166, 2006.

[132] S. Gezici, H. Kobayashi, H. Poor, and A. Molisch, "Performance evaluation of impulse radio UWB systems with pulse-based polarity randomization," *IEEE Transactions on Signal Processing*, vol. 53, no. 7, pp. 2537 – 2549, July 2005.

[133] D. Cassioli, M. Win, F. Vatalaro, and A. Molisch, "Low Complexity Rake Receivers in Ultra-Wideband Channels," *IEEE Transactions on Wireless Communications*, vol. 6, pp. 1265–1275, April 2007.

[134] R.-M. Cramer, R. Scholtz, and M. Win, "Evaluation of an Ultra-Wideband Propagation Channel," *IEEE Transactions on Antennas and Propagation*, vol. 50, pp. 561 –570, May 2002.

[135] S. Patarasen and C. Georghiades, "Maximum-likelihood symbol synchronization and detection of OPPM sequences," *IEEE Transactions on Communications*, vol. 42, no. 6, pp. 2282–2290, June 1994.

[136] G. Lui and H. Tan, "Frame Synchronization for Direct-Detection Optical Communication Systems," *IEEE Transactions on Communications*, vol. 34, no. 3, pp. 227–237, March 1986.

[137] K. Kiasaleh, "PN Code Acquisition for the Spread-Spectrum Optical On-Off-Keying Communication System," *IEEE Transactions on Communications*, vol. 38, no. 10, pp. 1879–1885, October 1990.

[138] C. N. Georghiades, "Maximum Likelihood Symbol Synchronization for the Direct-Detection Optical On-Off-Keying Channel," *IEEE Transactions on Communications*, vol. COM-35, no. 6, pp. 626–631, June 1987.

[139] ——, "Optimum Joint Slot and Symbol Synchronization for the Optical PPM Channel," *IEEE Transactions on Communications*, vol. COM-35, no. 6, pp. 632–636, June 1987.

[140] R. M. Gagliardi, "Synchronization Using Pulse Edge Tracking in Optical Pulse-Position Modulated Communication Systems," *IEEE Transactions on Communications*, vol. 22, no. 10, pp. 1693–1702, October 1974.

[141] T. Zhao, A. Nehorai, and B. Porat, "New data detection and symbol timing recovery approaches for burst optical signal transmission," in *Proc. ICASSP*, vol. 4, May 2004, pp. iv–917–920.

[142] ——, "K-means clustering-based data detection and symbol-timing recovery for burst-mode optical receiver," *IEEE Transactions on Communications*, vol. 54, no. 8, pp. 1492–1501, August 2006.

[143] U. Mengali, "Timing recovery in optical data transmission," *Optical and Quantum Electronics*, vol. 9, pp. 383–391, 1977.

[144] G. Lui, "PPM symbol synchronization in random data," in *Proc. IEEE Military Communications Conference (MILCOM)*, vol. 3, November 1991, pp. 1047–1053.

[145] M. Chiani, "Noncoherent Frame Synchronization," *IEEE Transactions on Communications*, vol. 58, no. 5, pp. 1536–1545, May 2010.

[146] J. Massey, "Optimum Frame Synchronization," *IEEE Transactions on Communications*, vol. 20, no. 2, pp. 115–119, April 1972.

[147] E. Bastaki, H. Tan, Y. Shi, and K. Letaief, "Frame synchronization based on multiple frame observations," *IEEE Transactions on Wireless Communications*, vol. 9, no. 3, pp. 1097–1107, March 2010.

[148] S. Aedudodla, S. Vijayakumaran, and T. Wong, "Timing acquisition in ultra-wideband communication systems," *IEEE Transactions on Vehicular Technology*, vol. 54, no. 5, pp. 1570–1583, September 2005.

[149] Z. Tian and V. Lottici, "Low-complexity ML timing acquisition for UWB communications in dense multipath channels," *IEEE Transactions on Wireless Communications*, vol. 4, no. 6, pp. 3031–3038, November 2005.

[150] C. Carbonelli, U. Mengali, and U. Mitra, "Synchronization and channel estimation for UWB signal," in *Proc. IEEE Global Telecommunications Conference (GLOBECOM)*, vol. 2, December 2003, pp. 764 – 768.

[151] R. Akbar and E. Radoi, "An overview of synchronization algorithms for IR-UWB systems," in *Proc. International Conference on Computing, Networking and Communications (ICNC)*, February 2012, pp. 573 –577.

[152] J. Ko and R. Gharpurey, "A pulsed uwb transceiver in 65 nm cmos with four-element beamforming for 1 gbps meter-range wpan applications," *IEEE Journal of Solid-State Circuits*, vol. 51, no. 5, pp. 1177–1187, May 2016.

[153] N. S. Kim and J. M. Rabaey, "A high data-rate energy-efficient triple-channel uwb-based cognitive radio," *IEEE Journal of Solid-State Circuits*, vol. 51, no. 4, pp. 809–820, April 2016.

[154] H. L. Xie, S. Q. Fan, X. Wang, and A. Wang, "An ultra-low power pulse-based uwb transceiver soc with on-chip adc," in *2006 49th IEEE International Midwest Symposium on Circuits and Systems*, vol. 1, Aug 2006, pp. 669–673.